

Impact of RF Imperfections on 60 GHz Wireless Communication Systems

Umar Hassan Rizvi

Impact of RF Imperfections on 60 GHz Wireless Communication Systems

PROEFSCHRIFT

ter verkrijging van de graad van doctor
aan de Technische Universiteit Delft,
op gezag van de Rector Magnificus Prof. ir. K.C.A.M. Luyben,
voorzitter van het College voor Promoties,
in het openbaar te verdedigen op maandag 21 november 2011 om 10.00 uur
door

Umar Hassan RIZVI

Master of Science in Electrical Engineering
Kungliga Tekniska Högskolan, Sweden
geboren te Lahore, Pakistan.

Dit proefschrift is goedgekeurd door de promotor:

Prof. dr. ir. I.G.M.M. Niemegeers

Copromotor: Dr. ir. G.J.M. Janssen

Samenstelling promotiecommissie:

Rector Magnificus	voorzitter
Prof. dr. ir. I.G.M.M. Niemegeers	Technische Universiteit Delft, promotor
Dr. ir. G.J.M. Janssen	Technische Universiteit Delft, copromotor
Prof. dr. M.-S. Alouini	King Abdullah University of Science and Technology
Prof. dr. J.R. Long	Technische Universiteit Delft
Prof. dr. ir. A.J. van der Veen	Technische Universiteit Delft
Prof. dr. A. Yarovoy.	Technische Universiteit Delft
Dr. ir. M.J. Bentum	Universiteit Twente
Prof. dr. A. Neto	Technische Universiteit Delft, reserve member

Copyright © 2011 by U.H. Rizvi

All rights reserved. No part of the material protected by this copyright notice may be reproduced or utilized in any form or by any means, electronic or mechanical, including photocopying, recording or by any information storage and retrieval system, without the prior permission of the author.

ISBN 978-94-6186-013-2

Author email: u.h.rizvi@gmail.com

To my father and mother

As far as the laws of mathematics refer to reality, they are not certain,
and as far as they are certain, they do not refer to reality. – Albert
Einstein (1879–1955)



Contents

Summary	v
List of Abbreviations	ix
List of Notations	xiii
1 Introduction	1
1.1 Background	2
1.2 Wireless Communication in the 60 GHz Band	5
1.2.1 Advantages, Disadvantages and Applications	5
1.2.2 60 GHz Standardization Activities	7
1.2.3 Challenges	9
1.2.4 SIGI Spot	10
1.3 Thesis Framework	11
1.4 Related Work	12
1.5 Summary of the Main Contributions	14
1.6 Thesis Organization	15
2 Channel and RF Impairment Models	19
2.1 Introduction	20
2.2 Channel Models	20
2.2.1 Path Loss Models	22
2.2.2 Frequency Selective Fading Models	22

2.2.3	Flat Fading Models	25
2.3	RF Circuit Impairment Models	28
2.3.1	DAC Model	30
2.3.2	ADC Model	32
2.3.3	Phase Noise Model	33
2.3.4	I/Q Imbalance Model	36
2.3.5	Amplifier Nonlinearity Model	37
2.4	Conclusions	39
3	Impact of RF Imperfections on Single-Carrier and Multi-Carrier Systems	41
3.1	Introduction	42
3.2	System Models	43
3.2.1	Multi-carrier based System	43
3.2.2	Single-carrier based System	45
3.2.3	Single-carrier and multi-carrier modulation with RF Im- perfections	50
3.3	System Complexity	50
3.4	Impact of DAC	52
3.5	Impact of ADC	53
3.6	Impact of Phase Noise	56
3.7	Impact of I/Q Imbalance	57
3.8	Impact of Amplifier Non-linearity	60
3.9	System Design Summary	63
3.10	Conclusions	63
4	Error Probability Analysis Under ADC Quantization Noise	65
4.1	Introduction	66
4.2	System Model	66
4.3	BER Analysis with AWGN	68
4.4	BER Analysis in Fading Conditions	71
4.5	Numerical Results	73
4.5.1	Error Probability	73
4.5.2	Impact of channel parameter m	76
4.5.3	Impact of the modulation level M	76
4.6	Conclusions	78

5	RF Level Diversity Combining	79
5.1	Introduction	80
5.1.1	Diversity combining	80
5.1.2	Conventional vs. RF Level Diversity Combining	82
5.2	System Model	83
5.3	RF Level Equal Gain Combining	86
5.3.1	Error Probability Analysis	89
5.3.2	PDF and CHF	90
5.3.3	Numerical Results	93
5.4	RF Level Selection Combining	97
5.4.1	Error Probability Analysis for Binary Signals	98
5.4.2	Error Probability Analysis for <i>MPSK</i>	101
5.4.3	Numerical Results	103
5.5	RF Level Switched Combining	107
5.5.1	Error Probability Analysis for Binary Signals	107
5.5.2	Error Probability Analysis for <i>MPSK</i>	111
5.5.3	Numerical Results	113
5.6	Comparison	122
5.7	Conclusions	124
6	Acoustic Demonstrator	125
6.1	Introduction	126
6.2	Setup	127
6.2.1	Sound card	127
6.2.2	Transmitter	127
6.2.3	Receiver Array	129
6.3	Channel Measurements	130
6.4	BER Comparison	137
6.5	Conclusions	137
7	Conclusions and Recommendations	141
7.1	Single-Carrier vs. Multi-Carrier Transmission	142
7.2	ADC Resolution	145
7.3	RF Level Diversity Combining	146
7.3.1	Equal Gain Combining	146
7.3.2	Selection and Switched Combining	147

7.4 Acoustic Demonstrator	148
A Integral Derivation	151
B An Alternative CHF for EGC	153
C Error Probability Derivations for Diversity Combining	157
C.1 BER of EGC at High SNR	157
C.2 Error Probability Derivation for MPSK Signals	158
C.3 Error Probability terms for Selection Combining	161
C.4 Error Probability terms for Switch and Stay Combining	163
C.5 Error Probability terms for Switch and Examine Combining	165
C.6 Error Probability terms for Switch and Examine Combining with Post Selection	168
List of Figures	171
List of Tables	175
Bibliography	177
Publications by the Author	189
Samenvatting	193
Acknowledgements	195
Curriculum Vitae	197



Summary

Impact of RF Imperfections on 60 GHz Wireless Communication Systems

Over the last couple of decades, wireless communication has proved to be a phenomenal success and has generated a booming industry with over 5 billion mobile handsets in use worldwide. This has on one end eased the life of its users while on the other end has introduced new challenges for wireless system designers. The varying nature of the wireless communication channel results in large differences in the instantaneous received signal strength. Since most mobile terminals are battery powered and operate in a network, simply increasing the transmission power is not an attractive solution, as it reduces the battery life and increases interference. Thus a major challenge in wireless communication is to increase the communication rate and link reliability by utilizing low power, low cost and spectrally efficient systems. Even with the advent of efficient signal processing techniques and miniaturized low power signal processing hardware, the physical bottleneck still remains the available system bandwidth. This has led to the introduction of the 60 GHz band as an attractive alternative. Among other benefits, the 60 GHz band is unlicensed and can provide system bandwidths up to 7 GHz, which is ideally suited for short range indoor wireless services such as wireless local area networks.

There are, however, certain challenges that need to be overcome before full potential of 60 GHz band can be harnessed. These challenges include the design of hardware components such as antennas, amplifier and mixers, identification

and utilization of suitable base band processing algorithms and efficient communication protocols for wireless networks operating in the 60 GHz domain. This dissertation deals with the design and development of baseband processing techniques for communication devices operating at a carrier frequency around 60 GHz.

Firstly, two practical candidates for baseband implementation are identified. The performance of these two alternatives namely single-carrier and multi-carrier is analyzed under various radio frequency circuit imperfections such as phase noise and amplifier non-linearity because low cost radio frequency circuits operating in the 60 GHz band are expected to have less than ideal performance. For both schemes, the performance degradation in terms of operating parameters such as the required number of bits in digital-to-analog converter/analog-to-digital converter and input back-off requirements for the power amplifier as a function of bit error probability, is determined. It is shown that the single-carrier schemes suffer a lower degradation in system performance for a given set of circuit parameters. The single-carrier scheme is therefore, identified as a suitable candidate for 60 GHz baseband implementation.

Secondly, we investigate the possibility of using low cost and complexity RF level diversity combining schemes to boost the system performance. Three low complexity diversity combining schemes namely equal gain combining, selection combining and switched combining are considered. An analytical framework for system performance evaluation of different diversity combining schemes by using low complexity RF level quantized phase combining is developed. Analytical expressions for the bit and symbol error rate of multi-level phase shift keying modulated symbols over Rayleigh fading channels are derived. The derived expressions are then utilized to compare the performance with non-coherent schemes under diversity reception. It is shown that the number of quantization levels required to achieve near ideal performance are dependent on the number of the receive antennas and the modulation level. The analysis is also utilized to investigate the impact of phase quantization on the switching threshold for switched combining schemes. It is shown that the switching threshold is not severely affected by phase quantization. The ability to perform various system level trade-offs is also demonstrated.

Lastly, a low cost audio demonstrator is proposed. The acoustic channels investigated in this thesis are seen to provide a multi-path rich environment typical of 60 GHz channels. This offers a practical way of verifying the performance of

various baseband processing algorithms in a cost effective manner.

Umar H. Rizvi



List of Abbreviations

ADC	Analog-to-digital converter
ADSL	Asymmetric digital subscriber line
AF	Amount of fading
AWGN	Additive white Gaussian noise
BER	Bit error rate
BFSK	Binary frequency shift keying
BPF	Bandpass filter
BPSK	Binary phase shift keying
CEP	Conditional error probability
CHF	Characteristic function
CIR	Channel impulse response
CMOS	Complementary metal oxide semiconductor

CMT	Common multiplicative term
CP	Cyclic prefix
CPR	Common phase rotation
CSI	Channel state information
DAC	Digital-to-analog converter
dB	Decibel
DPSK	Differential phase shift keying
DNL	Differential nonlinearity
EGC	Equal gain combining
FDE	Frequency domain equalization
FFT	Fast fourier transform
FMCW	Frequency modulated continuous wave
FT	Fourier transform
Gbps	Giga bits per second
GCQ	Gauss Chebyshev quadrature
GHz	Giga hertz
GSM	Groupe special mobile
HDTV	High definition television
HPA	High power amplifier
I/Q	In-phase quadrature-phase
IBI	Inter-block interference
IBO	Input back-off
ICI	Inter-carrier interference
IFFT	Inverse FFT
IFT	Inverse fourier transform

ISI	Inter-symbol-interference
LOS	Line-of-sight
LTV	Linear time variant
Mbps	Mega bits per second
MC	Multi-carrier
ML	Maximum likelihood
NLOS	Non line-of-sight
OFDM	Orthogonal frequency division multiplexing
PAM	Pulse amplitude modulation
PAPR	Peak to average power ratio
PC	Personal computer
PDF	Probability density function
PDP	Power delay profile
PLL	Phase locked loop
PN	Phase noise
PSD	Power spectral density
PSK	Phase shift keying
QN	Quantization noise
QoS	Quality of service
QPSK	Quadrature phase shift keying
RDS	RMS delay spread
RF	Radio frequency
RMS	Root mean square
RX	Receiver

SC	Selection combining
SC-FDE	Single-carrier with frequency domain equalization
SEC	Switch and examine combining
SEC _{ps}	Switch and examine combining with post selection
SNR	Signal-to-noise ratio
SSC	Switch and stay combining
SWC	Switched combining
TDL	Tapped delay line
TX	Transmitter
UAT	Ultrasonic air transducer
UF	Ultrasonic frequency (68 kHz)
WLAN	Wireless local area network



List of Notations

B	System bandwidth in Hertz
$E[.]$	Expectation operation
$\text{erf}(\cdot)$	Error function
$\text{erfc}(\cdot)$	Complimentary error function
${}_1F_1(\cdot; \cdot; \cdot)$	Confluent hypergeometric function of the first kind
$\mathcal{F}_k(\mathbf{x})$	k -th sample of the FFT of the vector \mathbf{x}
$\mathcal{F}_k^{-1}(\mathbf{x})$	k -th sample of the IFFT of the vector \mathbf{x}
f_o	PN spectrum bandwidth
F_s	Sampling frequency
h	Channel amplitude
$\Im[.]$	Imaginary part of any complex variable
K	Rician K factor
K_p	Total double sided integrated PSD
L	Phase quantization levels
\mathcal{L}	Noise floor
$\mathcal{L}_x(s)$	Laplace transform of a random variable x

N	OFDM and SC-FDE block length
N_{ADC}	ADC word length
N_{MA}	Number of multiply-and-accumulate operations
N_{DAC}	DAC word length
N_{max}	Maximum delay spread (in symbols)
N_R	Number of receive diversity branches
N_T	Total number of received multi-path components
$\langle P_{in} \rangle$	Average input power
P_{out}	Outage probability
P_0	Normalized received power
$p_x(x)$	PDF of a random variable x
$Q(\cdot)$	Gaussian Q function
$\Re[\cdot]$	Real part of any complex variable
T	Temperature in Kelvin
T_N	OFDM and SC-FDE block time
T_s	Sampling time
$var(x)$	Variance of a random variable x
V_{ref}	Reference voltage
γ	Instantaneous SNR
$\Gamma(\cdot)$	Gamma function
Δ_{SNR}	Degradation in SNR
ϵ	Amplitude imbalance
θ	Fading channel phase
τ	Channel delay
τ_{max}	Maximum delay spread (in seconds)
τ_{rms}	RMS delay spread
$\phi_x(\omega)$	Characteristic function of a random variable x
Ω	Second moment of channel amplitude

Chapter 1

Introduction

This chapter is a preamble and presents the outline and objectives of the research carried out in this dissertation. Various aspects of wireless communication in the 60 GHz band are outlined. A brief evolution of the 60 GHz band is given along with its advantages, disadvantages and possible applications. Popular standards for wireless communication in the 60 GHz band are discussed and challenges associated with this band are presented. The framework and scope of the research presented in this thesis are also outlined in this chapter.

1.1 Background

Wireless communication has come a long way since the first transatlantic radio transmission by Guglielmo Marconi in December 1901 [1]. Especially, in the last few decades there has been a vibrant growth in the wireless communication market and today a myriad of inexpensive wireless devices and services are available. This rapid growth is primarily attributed to the development of miniaturized low cost digital circuits and to the introduction of modern communication theory. Two significant milestones in this regard, which quite interestingly took place in the same year, were (1) the introduction of communication theory by Shannon in 1948 [2], (2) the development of solid state bipolar transistor by Shockley, Bardeen and Brattain in 1948 [3]. The introduction of the transistor paved the way for the development of inexpensive, light weight and portable radios, while the communication theory provided the frame work for establishing reliable links between the radio terminals. Since Shannon's discoveries, the communication theory has been extended and found applications in practical communication systems. Shannon's bound on reliable communication has eluded the communication engineers/theorists for a long time and it has only been within the past decade or so (with the advancement of digital hardware) that it was possible to reach within a few dB of Shannon's limit [4].

Communication through a wireless channel with its stochastic nature has proved to be quite challenging. The instantaneous signal strength received by an antenna in some instances can be quite large and at others can be so small that no message is likely to be received correctly. The brute force approach of increasing power is quite impractical as modern mobile communication terminals are required to be light weight and therefore power limited, and in a wireless network more power for one link means more interference for another [5]. Thus a major challenge in wireless communication is to increase the communication rate and link reliability by utilizing low power, low cost and spectrally efficient systems.

Today, a number of wireless systems and services operating in various frequency bands are available. These systems range from relatively simple radio broadcasting stations to complex satellite communication systems [6]. The most common and well known perhaps is the cellular telephony system which has gone through a series of evolutionary stages [7]. It started in the early 1980s with the analog first generation (1G) systems such as Nordic Mobile Telephone (NMT) in

Europe and Advanced Mobile Phone System (AMPS) in the U.S.A. The second generation (2G) systems which were based on digital technology were launched in the early 1990s. These 2G systems were based on the Groupe Spécial Mobile (GSM) standard and were considerably less bulky and more power efficient when compared to their 1G analog counterparts. The introduction of the GSM standard was a revolution in the cellular telephone industry as the cost and size of the handsets was drastically reduced. Currently, the third generation (3G) systems are available in the market which are primarily based on Enhance Data Rates for GSM Evolution (EDGE), Universal Mobile Telecommunication System (UMTS) and Code Division Multiple Access 2000 (CDMA 2000) standards. In addition to cellular telephony, wireless communications have found other applications as well. One other popular example is the wireless local area network (WLANs) which is primarily based on the IEEE 802.11 standard [8]. WLANs were mainly intended for short range high data rate communications as is generally required for internet connectivity. Unlike the cellular telephone systems, WLANs are small and localized (usually within and around buildings). This restricts mobility but provides much higher data rates. Although WLAN devices can access a larger frequency spectrum as compared to the cellular telephony devices, the data transfer rate in both systems is dictated by the available bandwidth. As the unit cost of IEEE 802.11 compliant chips is on a rapid decrease, more and more people at work and at home are utilizing WLANs. As can be seen from the two examples, i.e., cellular telephony (operating in the 900 MHz band) and WLAN (operating in the 2.54 GHz band), radio spectrum (bandwidth) is one of the most sought after resources in wireless communications. The rapid increase in the use of wireless services has lead to the problems of spectrum exhaustion and interference. System designers are therefore looking into other alternatives.

Many solutions have emerged to tackle the problems of interference and spectrum scarcity. One solution to increase the throughput is to boost the link quality by applying multiple transmit and receive antennas coupled with multi-level modulation techniques [9–12]. Multiple transmit antennas can be efficiently utilized to increase the system throughput by transmitting different information on each antenna element. Furthermore, multiple antenna elements can be utilized at the receiver to increase the average received signal strength by linear and non-linear diversity combining techniques [13, 14]. The most popular technique that effectively enhances the data rate and increases the link quality is known as the Bell

Labs layered space time (BLAST) architecture [11]. The problem of interference can be reduced by employing appropriate signal processing techniques for interference mitigation [15]. The problem of interference is more severe in localized IEEE 802.11 networks. This is due to the fact that an IEEE 802.11 wireless access point is easily affordable and operates in the unlicensed band. This implies that no permissions or licences are required for network deployment. As more and more people are putting these access points in small geographical locations (such as apartment complexes and offices) and the spectrum is rapidly being used up. The frequency reuse is thus taking place over short distances which can give rise to severe interference. Furthermore, the current technologies available today such as UWB and WLAN are unable to provide sufficient bandwidth for services such as high definition multimedia interfaces (HDMI), which require data rates in the range of Gbps.

The problems of interference and bandwidth lead researchers to explore alternative frequency bands, especially in localized wireless networks such as WLANs. The ultra wide band (UWB) and 60 GHz bands are two promising examples. The potential drawback of UWB in comparison with the 60 GHz band is the very low transmit power levels. A comparison of three popular short range communication standards is given in Table 1.1, in which the channel bandwidth and maximum transmitted power for UWB, WLAN and 60 GHz bands are shown. The UWB devices in principle are allocated in the bandwidth of 3.1 GHz - 10.6 GHz, which overlaps with many traditional narrowband and wideband communications systems such as WLANs. Thus in order to avoid interference, the maximum allocated power is kept extremely low (-43 dBm/MHz). The 60 GHz band on the other hand, offers the best possible alternative in terms of channel bandwidth allocation and allowed transmit power. This, however, comes at a price and certain obstacles should be overcome before this technology can be put to common use. A general introduction to the features, benefits, challenges and applications of the 60 GHz band is presented in Section 1.2. This thesis primarily deals with the baseband associated issues for wireless devices operating in the 60 GHz band. The main baseband related problems addressed in this dissertation are presented in Section 1.3. A brief literature survey regarding the baseband processing techniques for 60 GHz is presented in Section 1.4. In Section 1.5, the main contributions of this thesis are summarized. The thesis organization is outlined in Section 1.6.

Table 1.1: Channel bandwidths and power allocations for UWB, WLAN and 60 GHz bands.

Standard	Channel Bandwidth	Max. Transmit Power	Total Bandwidth
UWB	1355 MHz	0.4 mW	7.5 GHz
WLAN	40 MHz	1000 mW	100 MHz
60 GHz	2160 MHz	1000 mW	7 GHz

1.2 Wireless Communication in the 60 GHz Band

The origins of wireless communication with 60 GHz unmodulated carrier waves can be traced back to J. C. Bose [16]. In 1895, Bose remotely operated a bell and exploded gun powder over a distance of one mile using a 60 GHz carrier wave. Unfortunately, the semiconductor technology was not available at that time to further develop and explore wireless communications with 60 GHz carrier waves. It was only after the introduction of millimeter wave semiconductors that the interest in 60 GHz band was rekindled [17–26]. A further push was provided by the Federal Communications Commission (FCC) in 2001 when it allocated frequencies between 57 GHz and 66 GHz for unlicensed communication. Since then a number of standardization activities have been launched, many potential applications have been envisaged, new antenna and RF circuit designs have been proposed and novel baseband signal processing techniques have been introduced. Figure 1.1 gives a brief overview of various bands allocated in different parts of world for communication in the 60 GHz band. In this section we briefly outline some of these activities.

1.2.1 Advantages, Disadvantages and Applications

Wireless communications in the 60 GHz band entails certain advantages and disadvantages. The main advantages and disadvantages are:

- Small antenna sizes (*Advantage*). The antenna size is directly proportional to the wavelength of the transmission frequency. Thus as the frequency increases, the wavelength decreases. This means that 60 GHz, with a wavelength of 5 mm, offers the possibility of constructing miniaturized antenna elements. This carries significant benefits such as fabricating a large number of antenna elements within a small unit area and on chip antenna integration. Thus the 60 GHz band offers the potential to integrate a large number

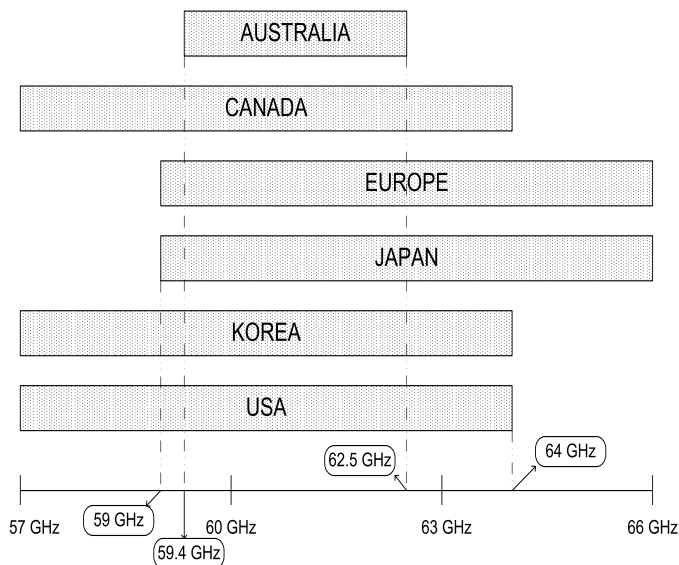


Figure 1.1: *Worldwide spectrum allocation for 60 GHz.*

of antenna modules in small portable wireless terminals. This also enables high antenna gain and beam with over a small circuit area.

- High wall and body attenuation (*Disadvantage/Advantage*). The 60 GHz carrier waves are severely attenuated when passed through walls or human body. This means that the signal level drops considerably from one room to the other and even within a single household or office complex multiple access points will be required to maintain connectivity and thereby increasing the cost of network deployment. Again, the positive aspect of this facet is the increased frequency reuse, security and resilience towards interference.

Some potential envisaged applications for the 60 GHz band are listed below:

- Fixed wireless access.
- Wireless local area networks.
- Personal area networks.
- Wireless multimedia streaming.
- Vehicular communication.

1.2.2 60 GHz Standardization Activities

Due to the numerous advantages and vast potential applications, a number of forums have been set up and standardization activities have been initiated to develop and promote wireless communications in the 60 GHz band [27–30]. Some major standardization activities are briefly reviewed in this section.

One of the main standardization activities undertaken by the IEEE for the 60 GHz communications band falls under the umbrella of IEEE 802.15.3c [27]. This activity has been ongoing for about half a decade. An initial proposal was released in October 2009. This standard outlines the physical (PHY) layer and medium access control (MAC) layer specifications for 60 GHz radios to establish reliable communications over short range. The IEEE 802.15.3c standard allocates four frequency channels each with a bandwidth of 2.14 GHz, and identifies three transmission schemes namely single carrier mode in mmWave PHY (SC PHY), high speed interface mode in mmWave PHY (HSI PHY) and audio/visual mode in mmWave PHY (AV PHY). The compliant devices should support at least one of these modes. The first mode, i.e., SC PHY is based on a single-carrier scheme while the other two require an orthogonal frequency division multiplexing (OFDM) based multi-carrier scheme. Each transmission scheme can employ a number of modulation and coding formats. The salient features of the various transmission schemes proposed in this standard are outlined in Table 1.2.

The second significant standardization effort after the IEEE 802.15.3c is the ECMA-387. The ECMA-387 standardization activity started about 4 years ago with the first edition of the standard released in December 2008. Like the IEEE 802.15.3c, it too describes the operating conditions for PHY and MAC layers. There are two main transmission modes supported in this standard, i.e., single-carrier block transmission (SCBT) and OFDM. A short summary of the modulation and coding schemes that can be used with each of these transmission methods is given in Table 1.3.

Two other notable standards for the 60 GHz communication band are the Wireless HD and Wireless Gigabit (WiGiG) standards [29, 30]. These are specifically tailored for high data rate audio/visual transmission such as that required by HDTV signals. These standardization activities are joint ventures of many companies including Broadcom, Intel, Dell, Nokia, LG and NEC. The standard details, however, are restricted and only available to the adaptors and partners.

Table 1.2: *IEEE 802.15.3c transmission modes.*

Transmission Mode	Data Rate	Modulations	Coding Schemes
SC PHY	25.8 - 5280 Mbps	$\pi/2$ BPSK ^a GMSK ^b $\pi/2$ QPSK ^c $\pi/2$ 8PSK $\pi/2$ 16QAM ^d	Reed Solomon LDPC ^e
HSI PHY	32.1 - 5005 Mbps	QPSK 16QAM 64QAM	LDPC
AV PHY	952 - 1904 Mbps	QPSK 16QAM	LDPC

^a Binary phase shift keying (BPSK).

^b Gaussian minimum shift keying (GMSK).

^c Quadrature phase shift keying (QPSK).

^d Quadrature amplitude modulation (QAM).

^e Low density parity check (LDPC).

Table 1.3: *ECMA-387 transmission modes.*

Transmission Mode	Data Rate	Modulations	Coding Schemes
SCBT	397 - 4234 Mbps	BPSK QPSK 8QAM 16QAM	Reed Solomon TCM ^a
OFDM	1008 - 2016 Mbps	QPSK 16QAM	Reed Solomon

^a Trellis coded modulation (TCM).

1.2.3 Challenges

The 60 GHz band has spurred new challenges for wireless system designers. Some of the issues are listed below:

- **High path loss and signal blocking.** The 60 GHz transmission band, unlike the currently available frequencies used in various standards, undergoes high additional oxygen absorption ($\approx 14\text{dB/km}$) and penetration losses. This high oxygen absorption and poor penetration implies that the link margins at 60 GHz are very tight and in order to maintain the wireless link with acceptable quality of service (QoS) very large distances or signal blocking should be avoided. This however, is not very relevant for short range indoor wireless communications. The received power P_r after passing through a wireless channel is given as $P_r \propto P_t d^{-n}$, where P_t denotes the transmitted power, d is the distance between the transmitter and the receiver and n is the path loss exponent. The 60 GHz channel has a high path loss exponent especially in non line-of-sight (NLOS) scenarios, which makes signal transmission prone to very deep fades if the line-of-sight (LOS) link is compromised. The high path loss, particularly in NLOS scenarios, is due to the high attenuation when passing through walls and body as explained in Section 1.2.1.
- **Inter-symbol interference.** Transmission through the 60 GHz channel, especially when high data rates are required, introduces severe inter-symbol interference (ISI), which needs to be mitigated by appropriate baseband processing techniques. Since applications of high data rates include wireless video broadcasting, which is extremely sensitive to delay, the baseband processing should accomplish equalization in short time (and with low complexity).
- **Limited circuit performance.** Traditionally, Gallium Arsenide (GaAs) and Indium Gallium Arsenide (InGaAs) based circuits were considered for the implementation of millimeter wave circuits including RF circuits for the 60 GHz communication band [23], due to their better power handling characteristics and low noise properties in comparison to complementary metal oxide semiconductor (CMOS). However, the GaAs and InGaAs based circuits are quite expensive and cannot be mass produced in a cost effective

manner. In order to reduce the system cost and to boost power efficiency, low cost CMOS based radio frequency (RF) circuits are more attractive. However, current CMOS RF circuits in the 60 GHz domain still have limited performance. Additionally, for low cost CMOS circuits, RF impairments such as phase noise, amplifier nonlinearities and analog-to-digital converter quantization effects should be countered by well chosen signal transmission schemes.

1.2.4 SIGI Spot

The 60 GHz communication project SIGI Spot: “60 GHz radio technology for high capacity wireless in-home communication networks”, was initiated in January 2006 to tackle the 60 GHz band communication challenges and to propose, design and investigate low cost system architectures. The SIGI spot project (IGC.0503) was jointly undertaken by Eindhoven University of Technology, Delft University of Technology and the Netherlands Organization for Applied Scientific Research (TNO), and financially supported by SenterNovem under and the IOP Generieke Communicatie (IOP GenCom) program. The main aim of the project was to develop “new low-cost radio technology using the license free 60 GHz frequency band”, with a focus on major bottle necks of the 60 GHz band from a layered perspective, i.e., to address problems related to antenna design, circuit design, baseband design and MAC design. This project involved four PhD researchers looking into these four aspects of 60 GHz band communication system design. The project was divided into a number of work packages (WPs), which are summarized below:

- WP1: This work package was aimed at management issues and overlooking the project progress.
- WP2: The main tasks for this WP were to investigate the possible propagation and application scenarios for the 60 GHz communication band.
- WP3: The design and fabrication of low cost antennas was the focus of this WP.
- WP4: Investigation of optimum choices for RF front end circuit elements such as mixers, low noise amplifiers and phase shifters.

- WP5: Investigation of appropriate transmission schemes for low cost 60 GHz transceiver implementation.
- WP6: Investigated energy efficient MAC protocols which can be used for neighbor discovery, source discovery and self configuration.
- WP7: Integration of various layers into a real working demonstrator that can be used as a proof of concept for a low cost 60 GHz transceiver.

The research presented in this thesis was carried out as a part of the WP5 activities.

1.3 Thesis Framework

Apart from numerous advantages and potential applications, several challenges for 60 GHz communication engineers exist that need to be overcome for this band to be put to common use as explained in Section 1.2.3. The specific problems addressed in this thesis can be listed as:

Single-carrier or Multi-carrier modulation schemes: High data rate transmission through 60 GHz channels suffers from ISI, which must be mitigated with appropriate modulation and base band processing schemes. Single-carrier block transmissions with frequency domain equalization (SC-FDE) and OFDM based multi-carrier (MC) schemes offer a good trade-off between performance and implementation complexity when used with frequency selective fading channels, such as those encountered at 60 GHz [31, 32]. In addition to ISI, low cost CMOS based RF circuits in the 60 GHz domain are still in their infancy and are therefore, expected to have limited performance [33]. Furthermore, in order to keep the implementation cost low, RF impairments such as digital-to-analog converter (DAC) and analog-to-digital converter (ADC) imperfections, phase noise (PN), amplifier nonlinearities and in-phase/quadrature phase (I/Q) imbalance should be countered by well chosen modulation and coding schemes. In this regards, it is vital to investigate the impact of various RF level circuit imperfections on SC-FDE and MC schemes.

ADC Resolution: It is well known that power consumption in an ADC is directly proportional to $F_s \cdot 2^{N_{ADC}}$, where F_s denotes the sampling frequency and N_{ADC} represents the ADC word length [34]. Thus with sampling rates

in the order of Giga samples per second, N_{ADC} must be kept as small as possible. An analytical, framework is, therefore, required to to choose ADC word length, depending on system parameters such as average received signal strength, the modulation technique and the fading conditions.

RF Level Diversity Combining: RF level diversity combining is a low cost and power efficient alternative in comparison to conventional diversity combining as it requires fewer ADCs and down converters (mixers). RF diversity combining, which employs RF level phase shifters and variable gain amplifiers, has certain issues that need to be addressed, for example, determining the performance as a function of average received signal-to-noise ratio (SNR), the number of phase shifting steps and the modulation scheme.

Low Cost Test bed: It is cumbersome to develop a cost effective demonstrator for 60 GHz due to high sampling rate requirements. In order to present a proof of concept for various baseband processing algorithms a low cost demonstrator was developed. This demonstrator models 60 GHz transmission scenarios at one hand and on the other hand is easier to program so that the focus was shifted from algorithm implementation to algorithm design.

1.4 Related Work

A number of research activities have been carried out on the design and evaluation of wireless communication systems operating in the 60 GHz band. These activities can be broadly categorized in five major aspects, i.e., propagation studies, antenna design, circuit design, baseband design and MAC layer protocols. Since this thesis primarily deals with the baseband aspects of 60 GHz communications a brief literature study of this area is presented in this section.

Traditionally, an OFDM based multi-carrier scheme was the only practically realizable alternative for mitigating the effect of severe ISI typical for indoor wireless mobile radio channels. Therefore, it was adapted for the IEEE 802.11 standard. However, high data rate signalling at 60 GHz carrier frequencies in addition to severe ISI conditions also suffers from a number of RF circuit imperfections. Therefore, in addition to countering ISI, the transmission scheme for 60 GHz must also have a low peak-to-average-power ratio (PAPR) and a high phase noise resilience. The SC-FDE is an alternative that has low PAPR and identical system complexity as that of OFDM. A number of general and 60 GHz specific

comparisons of these two schemes has been carried out in the literature. However, their sensitivity to RF circuit impairments in 60 GHz transmission scenarios is not yet fully investigated. A number of comparisons between multi-carrier and single-carrier schemes can be found in literature [35–38]. SC-FDE has a lower peak-to-average-power ratio (PAPR), and is more resistant to frequency offset errors as compared to the multi-carrier scheme [36]. The SC-FDE scheme with both phase shift keying and quadrature amplitude modulations was shown to require a lower input back-off (IBO) for the high power amplifier (HPA) and has a similar sensitivity to phase noise (PN) and in-phase/quadrature-phase (I/Q) imbalance for IEEE 802.11 transmission scenarios [38]. The SC-FDE scheme is known to achieve maximum diversity under frequency selective fading conditions [36], and therefore outperforms the MC scheme in un-coded scenarios. The operating parameters for 60 GHz RF circuits such as the available number of bits in the ADC, phase noise variance and I/Q imbalance values are expected to be different from IEEE 802.11. Therefore, a comparison of both SC-FDE and OFDM schemes under realistic 60 GHz RF front end and transmission scenarios is imperative for system design purposes.

Diversity combining employing multiple receive antennas is a well known concept that was first reported by Brennan in 1959 [13]. The diversity combining can be roughly divided into two categories, i.e., optimum diversity combining¹ and sub-optimum diversity combining. Maximum ratio combining (MRC) is the optimum diversity combining technique with the best possible performance. This however, is also the most complex in terms of channel estimation and combining implementation as both the channel phase and amplitude need to be estimated and used in the diversity combining process. A number of sub-optimum combining schemes with lower implementation complexity and slightly worse performance than MRC are preferred. Three main sub-optimum diversity combining techniques are equal gain combining (EGC), selection combining (SC) and switched combining (SWC). A lot of work has been done in investigating the performance of these diversity combining schemes when perfect and imperfect channel state information is available at the combiner. However, their applicability with RF level diversity combining, as envisaged for 60 GHz transceivers, is not yet fully investigated. The performance analysis for EGC, SC and three variants of SWC, namely; switch and stay combining (SSC), switch and examine combining (SEC)

¹The classification of optimum and sub-optimum is based on interference free scenario.

and switch and examine combining with post selection (SECps), with perfect and imperfect channel state information, has been extensively reported in the literature [39–55]. This performance analysis enables the system designer to quickly and efficiently investigate the gain in system performance and to choose certain design parameters such as the number of diversity branches required to achieve a certain specified error probability at a given SNR. For example, the performance of EGC with perfect CSI was reported in [39–41, 41–43]. For certain realistic scenarios CSI is not available and the impact of CSI errors on the performance of EGC was reported in [44]. The analysis of SC and SWC was treated in [45–48]. Some common conclusions that can be derived from these investigations are summarized as follows. In all the diversity combining schemes the maximum incremental gain in performance is achieved when the number of diversity branches are increased from one to two. Diminishing gains are obtained as the number of diversity branches are increased beyond two. Diversity combining, with correlated fading at the antennas, gives little or no improvement in the system performance [14]. Imperfect CSI beyond a certain specified threshold gives rise to irreducible error floors. In all the investigations for diversity combiners carried out so far one important peculiar facet, i.e., RF level diversity combining, has been neglected. Therefore, in this thesis we look closely into the performance and design considerations of various low complexity sub-optimal RF level diversity combining schemes.

1.5 Summary of the Main Contributions

A summary of the main contributions of this dissertation is given below:

- A comprehensive qualitative and quantitative comparison of single-carrier and multi-carrier based transmission schemes for 60 GHz scenarios in the presence of various RF circuit impairments is carried out. The RF impairments taken into account are DAC imperfections, ADC imperfections, phase noise effects, I/Q imbalance and amplifier nonlinearities.
- Novel closed-form analytic expressions for the bit error rate evaluation of single-carrier M -ary pulse amplitude modulated (MPAM) signal constellations as a function of the ADC word length, the SNR and the channel fading distribution, are derived. These results allow for a rapid and accurate evaluation of the system performance when the ADC resolution is limited, as is generally the case in high sample rate communication systems, and thus

provide a useful tool for system design, analysis and optimization.

- The possibility of utilizing the RF level diversity combining architectures with low complexity sub-optimal diversity combining schemes such as EGC, SC and SWC is investigated. Novel analytical expressions to evaluate the performance in terms of average error probability for single-carrier binary and multi-level phase shift keying (PSK) signal constellations in Rayleigh fading channels, are derived. These expressions are then used for:
 - investigating the impact of phase quantization on the system performance;
 - comparison with non-coherent and partially coherent schemes;
 - making system level trade-offs.
- A low cost acoustic test bed, for the design and verification of baseband algorithms for 60 GHz communication links, is proposed. The test bed is constructed from inexpensive audio components. The main idea behind the acoustic demonstrator is that the audio waves at 68 kHz have the same wavelength as that of 60 GHz radio waves. It is therefore expected that the propagating waves experience comparable multi-path effects at 60 GHz as at millimeter wavelength audio frequencies, which means that baseband processing algorithms will show a similar performance in both acoustic and radio wave channels. Since the baseband signal processing can be done at much lower sampling rates as compared to the radio channel, a low cost demonstrator can be used to demonstrate the proof of concept and to investigate various modulation and baseband processing schemes. The focus could therefore be shifted from algorithm implementation to algorithm design and verification aspects. Many aspects of the system design such as diversity combining, beam forming and channel estimation can therefore be practically verified on the acoustic demonstrator before being translated to the 60 GHz RF band.

1.6 Thesis Organization

This thesis can be broadly divided into three major parts. In the first part comprising the Chapters 2, 3 and 4, we first introduce the RF impairments and channel models and then look into the performance of single-carrier and multi-carrier

schemes under various RF circuit imperfections. The second part, consisting of Chapter 5, investigates the performance of various RF level diversity combining schemes. Three sub-optimal schemes namely EGC, SC and SWC, are considered. In the last part, which consists of Chapter 6, we introduce a low cost acoustic demonstrator which can be used for baseband algorithm design and implementation purposes. A chapter wise summary is given below:

- **Chapter 2:** In this chapter, channel models and RF imperfection models are introduced. Frequency flat and frequency selective channel models for various 60 GHz transmission scenarios are introduced. Transfer characteristics for the DAC, the ADC, the non-linear amplifier, PN and I/Q imbalance are given.
- **Chapter 3:** In this chapter, a performance comparison of SC-FDE and OFDM based transmission schemes in the presence of RF circuit imperfections and 60 GHz transmission scenarios is carried out. The overall complexity of the single-carrier and multi-carrier schemes is computed and compared.
- **Chapter 4:** In this chapter, closed-form expressions for the bit error rate of MPAM signal constellations as a function of the ADC word length, the SNR and the fading distribution, are derived. These expressions are then used to evaluate the impact of ADC word length on the performance of various MPAM schemes in different fading scenarios and to make system level tradeoffs.
- **Chapter 5:** In this chapter, the concept of RF level diversity combining is introduced. The possibility of utilizing the RF level diversity combining architecture with low complexity sub-optimal combining schemes such as EGC, SC and SWC, is explored. The impact of channel phase quantization on the performance of EGC, SC and SWC diversity combining schemes is investigated by deriving novel analytical expressions in terms of phase quantization levels L , the received signal-to-noise ratio (SNR) and the number of receive antennas N_R , for phase shift keying schemes. The mathematical analysis, is then used to perform system level trade-offs between N_R and L . Also, the performance with non-coherent frequency shift keying and differential phase shift keying schemes is compared. For SWC schemes the

analysis is also utilized to investigate the impact of phase quantization on switching threshold.

- **Chapter 6:** In this chapter, the design of a low cost acoustic demonstrator is described. Path loss and channel impulse response measurements are performed at 10 kHz and 68 kHz and compared with 60 GHz transmission scenarios. The bit error rate of single-carrier and multi-carrier techniques on both acoustic and radio channels is also compared.
- **Chapter 7:** In this chapter, the main highlights of the thesis are summarized. Major contributions are given and a number of unresolved issues as well as future research directions are presented.

Chapter 2

Channel and RF Impairment Models

Wireless signal transmission in the 60 GHz band undergoes fading and is degraded by various RF circuit imperfections in the front end. Therefore, in order to make a realistic evaluation of various transmission schemes, transfer characteristics of the wireless channel and RF imperfections are required. In this chapter, we introduce the system models for RF imperfections and wireless channels that will be used repeatedly throughout this thesis to model the front end and transmission scenarios for the 60 GHz band. Specific 60 GHz frequency selective and frequency flat channel models are introduced. Transfer characteristics for digital-to-analog converter, analog-to-digital converter, non-linear amplifier, phase noise and in-phase/quadrature-phase imbalance are also outlined.

2.1 Introduction

Signal transmission through a wireless communication channel is known to undergo large scale as well as small scale propagation effects. The main difference between these two types of fading conditions is outlined in this chapter and the large scale and the small scale characteristics for the 60 GHz communication channels are reviewed.

As indicated in the previous chapter, the signal transmission at 60 GHz is plagued with various RF component imperfections in addition to the channel fading. Secondly, at very high sampling rates that are typical for 60 GHz communication systems, several circuit elements such as ADCs are limited in the sense that larger word lengths are difficult to achieve. Also large word length ADCs consume a large chunk of the total transceiver power which is not desirable, especially for portable terminals. Lastly, as explained before, due to their low cost and high power efficiency, CMOS based circuits are preferred over GaAs. The design of low noise mixers and linear power amplifiers with CMOS is quite cumbersome, therefore the signal when passing through the front end is expected to undergo degradation from a number of circuit elements. In this chapter, we outline the transfer characteristics of various RF circuits used in the front end that may degrade the system performance at 60 GHz.

The chapter organization is as follows. In Section 2.2, path loss, frequency flat and frequency selective channel fading models that model various 60 GHz transmission scenarios, are presented. System level transfer characteristics of DAC, ADC, PN, I/Q imbalance and amplifier non-linearity, are outlined in Section 2.3. Conclusions are drawn in Section 2.4.

2.2 Channel Models

There are four basic mechanisms that impact signal propagation through wireless communication channels, namely spatial dispersion, reflection, refraction and scattering [56]. A characterization framework of wireless multi-path channels was initially presented by Bello [57]. It was shown that wireless channels can be modeled as linear time variant (LTV) systems which can be characterized in an interesting symmetrical manner by arranging system functions in time-frequency dual pairs [57]. The exact derivation of the channel correlation functions and their properties can be found in [57].

The generalized channel model for the wireless communication system shown in Figure 2.1, is given as

$$y(t) = h(t) * x(t) + n(t), \quad (2.1)$$

where $y(t)$ represents the received signal, $h(t)$ represents the channel impulse response (CIR) and $n(t)$ is random noise, which for most communication systems is known to follow the Gaussian distribution. The $*$ denotes the convolution operation and $x(t)$ represents the transmitted signal. The CIR is given as [56]

$$h(t) = \sum_{i=0}^{N_T-1} h_i e^{-j\theta_i} \delta(t - \tau_i), \quad (2.2)$$

where h_i represents the amplitude of the i -th multi-path component, θ_i denotes the phase, τ_i gives the delay and N_T is the total number of received rays or resolvable components. For the case of the well known additive white Gaussian noise (AWGN) channel model, there is no fading hence $h(t) = \delta(t)$, where $\delta(t)$ is the dirac delta function. Thus, (2.1) reduces to

$$y(t) = x(t) + n(t). \quad (2.3)$$

For the case when different multi-path components cannot be resolved, i.e. frequency flat fading, the convolution turns into a multiplication as there is only the fading component. This implies $N_T = 1$ and reduces (2.1) to

$$y(t) = h_0 e^{-j\theta_0} x(t) + n(t), \quad (2.4)$$

where the first component delay is taken as reference and assumed to be 0, i.e., $\tau_0 = 0$.

The wireless transmission at 60 GHz can also experience various types of fading depending on the chosen application and environment. For lower data rate (≤ 100 Mbps) frequency flat channel fading can be assumed. For high data rate signalling (≥ 1 Gbps), the channel is essentially frequency selective. A number of measurement campaigns at 60 GHz have been carried out and various path-loss and statistical models have been proposed in the literature [58–64]. In this section some commonly used path loss, frequency flat and frequency selective

channel models for the 60 GHz band are reviewed.

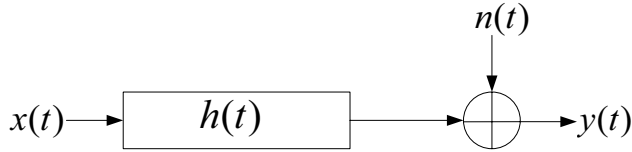


Figure 2.1: *A simplified wireless signal transmission model.*

2.2.1 Path Loss Models

Large scale fading is also commonly referred to as shadowing [6, 56, 65]. As its name suggests, the variation in received signal power due to large scale fading occurs over a distance of 1-10 meters. The 60 GHz communication band has some peculiar path loss characteristics that distinguish it from other frequency bands. It has poor wall and body penetration characteristics and the signal strength drops significantly over short distances (typically a few meters). Most propagation studies at 60 GHz model the path loss as

$$PL(d) = PL_0 + 10n \log_{10}(d) + X_\sigma \text{ (dB)} \quad (2.5)$$

where $PL(d)$ is the path loss at distance d , n is the path loss exponent and X_σ denotes a zero mean Gaussian distributed random variable with standard deviation σ (in dB). The term PL_0 represents the reference path loss typically at a distance of 1 m. The channel parameters σ and n are derived from channel measurements. The received power $P_r(d)$ at a distance d is then given by

$$P_r(d) = P_t + G_t + G_r - PL(d) \text{ (dB)}, \quad (2.6)$$

where P_t is the transmitted power, G_t and G_r represent the transmit and receiver antenna gains, respectively. Table 2.1 gives an overview of various propagation channel models. Figures 2.2 shows the path loss $PL(d)$ as a function of d for some selected channel models in NLOS and LOS environments (excluding X_σ).

2.2.2 Frequency Selective Fading Models

Variations due to multi-path propagation (small-scale fading) occur over very short distances comparable to the wavelength of the carrier frequency, which for

Ref.	Link	PL_0 [dB]	n	σ [dB]	Env.	Tx/Rx Ant.
Haibing [58]	NLOS	71	2.7	2.7	Room	Omni/Omni
	LOS	87.8	0.6	1.3	Room	Omni/Omni
		79.7	0.4	1.0	Room	Fan/Omni
		67.0	2.1	0.8	Room	Fan/Fan
		67.4	2.0	0.6	Room	Fan/Pen
Fryziel [66]	LOS	45.47	1.92	1.72	Office	Direc. (30) HP
		49.76	1.61	1.52	Office	Direc. (30) CP
IBM [67]	-	71.53	1.42	5.78	Library	-
		77	1.35	6.37	Home	-
France Tel. [68]	NLOS	16.2	2.44	6.2	Home	Sect. (60/72)
	LOS	23.5	1.53	1.5	Home	Sect. (60/72)
		4.3	1.73	1.6	Home	Direc. (60/10)
		49.6	0.56	1.2	Office	Sect. (72/60)

Table 2.1: Various path loss channel parameters at 60 GHz

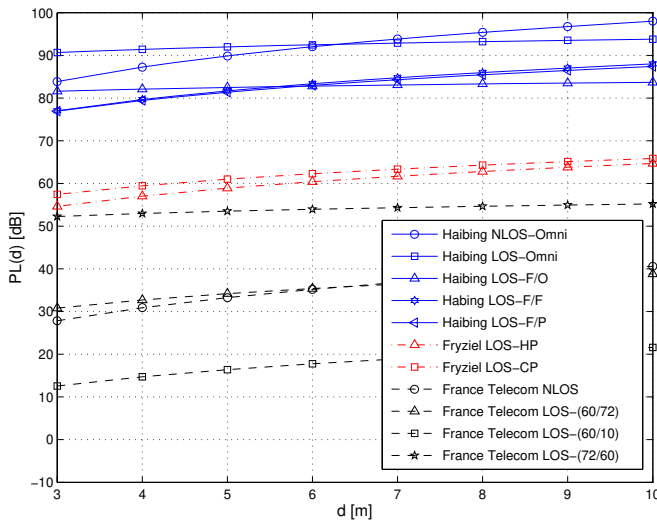


Figure 2.2: Path loss as a function of d for various 60 GHz channels

the case of 60 GHz band is 5 mm. Small scale characteristics are therefore more relevant for baseband design and performance evaluation purposes, whereas the large scale characteristics are more pertinent for link budget analysis. The channel parameters for a frequency selective channel model can be defined in terms of the statistical power delay profile (PDP). The PDP which specifies the ray powers

and their relative delays is given as [56]

$$p(\tau) = \sum_{i=0}^{N_T-1} h_i^2 \delta(\tau - \tau_i). \quad (2.7)$$

The normalized received power, denoted by P_0 is the sum of individual ray powers [56]

$$P_0 = P_t \sum_{i=0}^{N_T-1} h_i^2, \quad (2.8)$$

where P_t denotes the transmitted power. The Rician K -factor which is the ratio of the dominant path's power to the power in the scattered paths is defined as [69]

$$K = \frac{h_{\max}^2}{P_0 - h_{\max}^2}, \text{ where } h_{\max} = \max_i \{h_i\}. \quad (2.9)$$

If a LOS link exists between the transmitter and the receiver, then the first ray is the dominant one, implying that $h_{\max} = h_0$ at $\tau_0 = 0$. The root-mean-square (RMS) delay spread is defined as the second moment of the normalized PDP and is given as [56]

$$\tau_{rms} = \sqrt{\overline{\tau^2} - \bar{\tau}^2}, \text{ where } \bar{\tau}^m = \sum_i \tau_i^m h_i^2 / P_0, \quad m = \{1, 2\}. \quad (2.10)$$

The channel characteristics at a given time instant in a particular area are determined by these three parameters, i.e., P_0 , the normalized received power, K , the Rician K -factor and τ_{rms} , the RMS delay spread (RDS). Channel modeling is, therefore, aimed at estimating and characterizing these parameters. For a wide-band channel the multi-path is completely resolved and channel parameters vary little as the individual channel amplitudes do not change rapidly within a local area, however, for the flat fading case the multi-path cannot be resolved thus giving rise to multi-path interference which in turn results in a rapid fluctuation of the channel amplitude and phase. The RMS delay spread is considered to be the most important single parameter influencing the time-extent of the dispersive channel. It is also used to characterize the frequency-selectivity of the channel.

A number of frequency selective fading models for 60 GHz communication have been proposed in the literature [58–64, 70]. In this thesis, a simplified TDL model [63, 70] representing indoor LOS and NLOS 60 GHz transmission scena-

	LOS	NLOS
Delay [ns]	Power [dB]	Power [dB]
0	0	0
15	-30	-10
20	-15	5
35	-30	-10
40	-30	-10
45	-20	0
55	-35	-15
70	-28	-8

Table 2.2: Power delay profile for LOS and NLOS 60 GHz tapped delay line model.

rios will be used. Table 2.2 gives the PDP for LOS and NLOS 60 Hz TDL [70]. The NLOS scenario has a relatively high $E[\tau_{rms}] = 16.14$ ns as compared to $E[\tau_{rms}] = 6.58$ ns for the LOS case and thus results in severe ISI when used at high data rates. Such a model is useful for initial performance evaluation of a proposed 60 GHz communication system.

2.2.3 Flat Fading Models

A wireless system operating in a flat fading environment is affected by the phase and amplitude of the fading channel, as shown by equation (2.4). Dropping the subscript in (2.4), for notational convenience we represent the channel amplitude and phase as h and θ , respectively. The amplitude gain h and phase θ are both random variables and can, therefore, be characterized by their PDFs denoted by $p_h(h)$ and $p_\theta(\theta)$, respectively. The PDF is generally dependent on the underlying nature of radio wave propagation. The mean square value or second moment of h is denoted by $\Omega = E[h^2]$, where $E[\cdot]$ denotes the expectation operation. The transmitted signal is further perturbed by additive white Gaussian noise (AWGN) at the receiver. The AWGN is generally independent of the channel parameters. The amount of fading or fading figure is defined as

$$\text{Amount of Fading} = \frac{\text{var}(h^2)}{E[h^2]^2} = \frac{E[(h^2 - \Omega^2)^2]}{\Omega^2}, \quad (2.11)$$

where $\text{var}(\cdot)$ denotes the variance. The amount of fading is a measure of the severity of the fading. The statistical behavior of the fading envelop and phase is described by a number of distributions, depending on the operating scenario. For

example a narrow band NLOS link at 60 GHz can be modeled with a Rayleigh distribution, whereas the Nakagami- m and Nakagami- n distributions are required to reflect the LOS transmission scenarios. In the following subsections a brief overview of the Rayleigh, Nakagami- n and Nakagami- m distributions is given. The interested reader is referred to [14, ch. 2] for further details. Before moving on to the specific channel models we define the instantaneous and average SNR as $\gamma = h^2 E_s / N_0$ and $\bar{\gamma} = E[h^2] E_s / N_0$, respectively. The symbol N_0 denotes the AWGN noise power spectral density and E_s denotes the energy of the transmitted symbol.

Rayleigh Fading

As mentioned before Rayleigh fading is used to model the amplitude of the carrier wave when no LOS link exists between the transmitter and the receiver. The PDF of the channel amplitude gain for Rayleigh fading is given by the experimental distribution

$$p_h(h) = \frac{2h}{\Omega} e^{-\frac{h^2}{\Omega}}, \quad h \geq 0. \quad (2.12)$$

The phase is uniformly distributed, i.e.,

$$p_\theta(\theta) = \begin{cases} \frac{1}{2\pi}, & -\pi < \theta \leq \pi \\ 0, & \text{otherwise.} \end{cases} \quad (2.13)$$

The distribution of the instantaneous SNR γ for Rayleigh fading channels is given as

$$p_\gamma(\gamma) = \frac{1}{\bar{\gamma}} e^{-\frac{\gamma}{\bar{\gamma}}}. \quad (2.14)$$

Nakagami- n Fading

The Nakagami- n distribution is used to model transmission scenarios where a strong LOS exists in combination other weaker random components. This distribution is also known as the Rice distribution. The PDF of the received signal amplitude is given as

$$p_h(h) = \frac{2(1+n^2)e^{-n^2 h}}{\Omega} e^{-\frac{(1+n^2)h^2}{\Omega}} I_0\left(2nh\sqrt{\frac{1+n^2}{\Omega}}\right), \quad h \geq 0, \quad (2.15)$$

where n denotes the Nakagami- n fading parameter which ranges from 0 to ∞ and is related with the Rician K factor as $K = n^2$ and $I_0(\cdot)$ denotes the zero-order modified Bessel function of the first kind. As explained before, K denotes the ratio of the power of the LOS component to the scattered components. The PDF of the instantaneous SNR is given as

$$p_\gamma(\gamma) = \frac{(1+n^2)e^{-n^2}}{\gamma} e^{-\frac{(1+n^2)\gamma}{\bar{\gamma}}} I_0\left(2n\sqrt{\frac{(1+n^2)\gamma}{\bar{\gamma}}}\right). \quad (2.16)$$

The channel phase for Nakagami- n case is also uniformly distributed as in the case of Rayleigh fading.

Nakagami- m Fading

The PDF of the received signal amplitude for Nakagami- m fading is given as

$$p_h(h) = \frac{2m^m h^{2m-1}}{\Omega^m \Gamma(m)} e^{-\frac{mh^2}{\Omega}}, \quad h \geq 0, \quad (2.17)$$

where m denotes the Nakagami- m fading parameter which ranges from $1/2$ to ∞ . For Nakagami- m fading, the channel phase does not follow a uniform distribution. The channel phase distribution for the Nakagami- m fading environment is given as [71]

$$p_\theta(\theta) = \frac{\Gamma(m) |\sin(2\theta)|^{m-1}}{2^m \Gamma^2(m/2)}, \quad (2.18)$$

where $\Gamma(\cdot)$ denotes the gamma function. The PDF of the output SNR for Nakagami- m fading is given as

$$p_\gamma(\gamma) = \left(\frac{m}{\gamma}\right)^m \frac{\gamma^{m-1}}{\Gamma(m)} e^{-\frac{m\gamma}{\bar{\gamma}}}. \quad (2.19)$$

The Nakagami- m distribution, via its fading parameter m , spans the widest range of all fading distributions. It is good to note here that the Rayleigh distribution is a special case of the Nakagami- m distribution with $m = 1$ and Nakagami- n distribution with $n = 0$. The Nakagami- m can also approximate the Nakagami- n distribution and this mapping is given as

$$m \approx \frac{(1+n^2)^2}{1+2n^2}. \quad (2.20)$$

The PDFs of Rayleigh, Nakagami- n and Nakagami- m fading distributions are plotted in Figure 2.3 for various n and m values. It can be seen from Figure 2.3 that the Rayleigh fading has a higher probability of a signal experiencing a deep fade and therefore represents the worst fading condition (apart from $m = 1/2$). It is also observed that lower values of n and m typify more severe fading conditions. The phase distribution of Nakagami- m fading is shown in Figure 2.4.

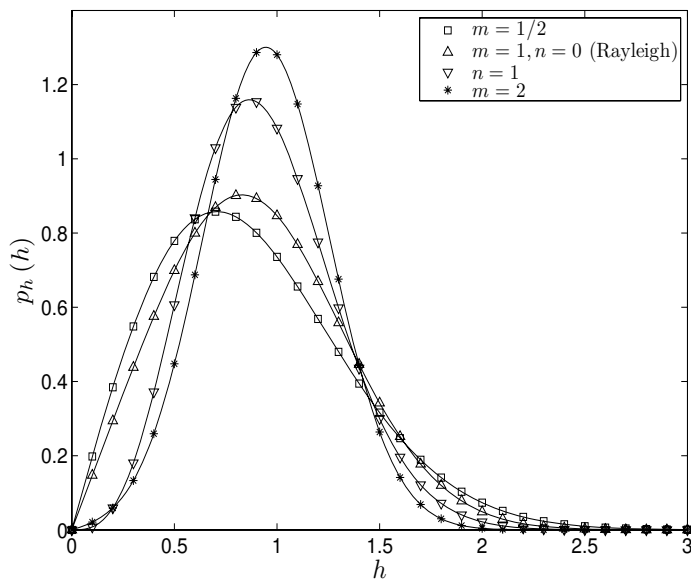


Figure 2.3: Nakagami- m and Nakagami- n amplitude PDFs for various value of m and n .

2.3 RF Circuit Impairment Models

The choice of a suitable receiver architecture is a trade-off between complexity, cost and performance. Ideally, wireless terminals should be cheap, small and light with a long battery life time. Therefore, the transceiver architecture should be suitable for a single silicon chip. This goal of a single chip integration can be realized with adaptive wireless devices. An effective way of adding reconfiguration into the system is to move the analog/digital interface closer to the antenna. From a flexibility and adaptability perspective, the traditional superheterodyne receiver is not the most viable alternative. Instead, receiver architectures which greatly simplify the analog front end are required. One such example is the direct

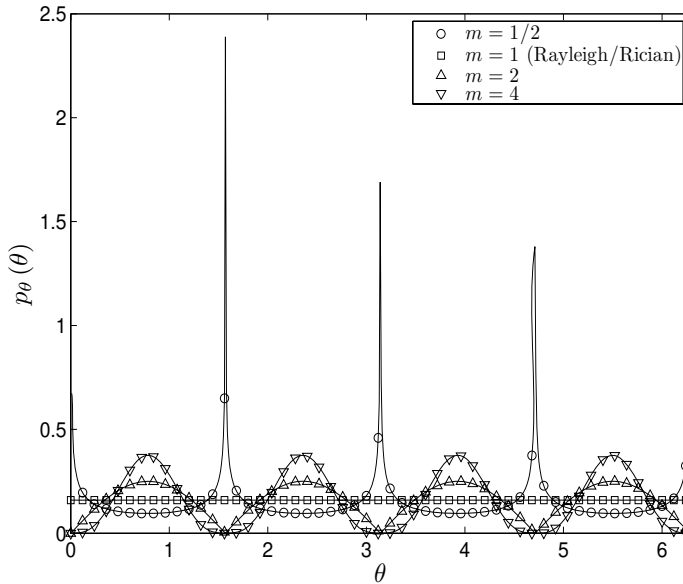


Figure 2.4: Nakagami- m phase PDF for various value of m .

conversion architecture as shown in Figure 2.5. This has numerous advantages over the traditional superheterodyne architecture shown in Figure 2.6. The biggest advantage is that it requires fewer components which makes it low cost and power efficient. However, this comes at the cost of increased requirements on the baseband signal processing. Throughout the rest of this thesis we will assume the direct conversion architecture for the RF front end, unless otherwise stated.

The DACs and the ADCs act as the interface between the digital baseband and the analog RF front end. Prior to transmission the digital baseband signal is first converted to the analog domain via the DAC. This signal is then up-converted using orthogonal quadrature mixers. The orthogonality of the carrier waves enables two separate in-phase and quadrature-phase (I/Q) signals to be added without interference and, therefore, helps to boost the spectrum efficiency of the system. The added I/Q signal is then passed through the high power amplifier (HPA) and fed to the transmit antenna. The received signal is amplified using a low noise amplifier (LNA) and down-converted to baseband frequencies using I/Q mixers. The signal phase for the down conversion mixers is estimated by a phase locked loop (PLL). The signal is then passed to the digital baseband through the

ADCs.

In an ideal scenario, all the elements mentioned thus far, i.e., DACs, ADCs, PLL, HPA and LNA should not deviate from their desired behavior. For example, amplifiers should act as linear gain devices. This, however, is not the case in practice and especially not the case for 60 GHz CMOS radios. Therefore, each of these elements attenuate the signal and add noise into the system. The impact of noise is dependent on channel conditions and transmission schemes, among other things. In this section, the 60 GHz specific transfer characteristics of each of these elements is explained.

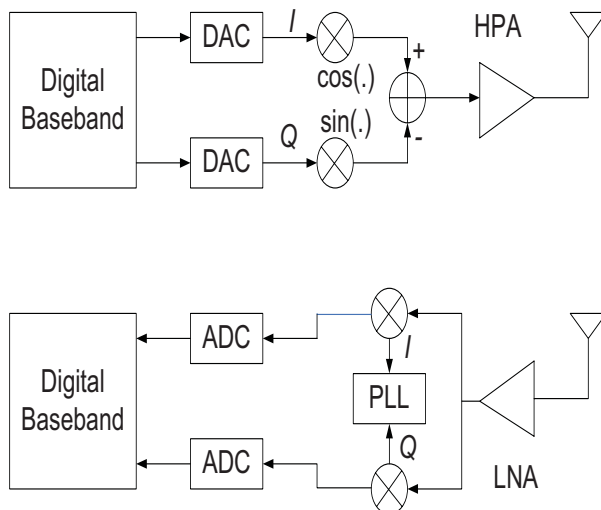


Figure 2.5: Simplified block diagram of a direct conversion transceiver.

2.3.1 DAC Model

A DAC converts digital data into analogue electrical signals. The number of bits of the DAC, N_{DAC} must be kept to a minimum in order to make a low cost and power efficient system. A simple way to model the DAC output is to consider the input signal added with quantization noise (which is assumed to be uniformly distributed). This however is too simplistic and (to the best of our knowledge) none of the commercially available DACs operating at sampling rates of Gsps demonstrates such a behavior. Therefore, we consider a realistic DAC based on

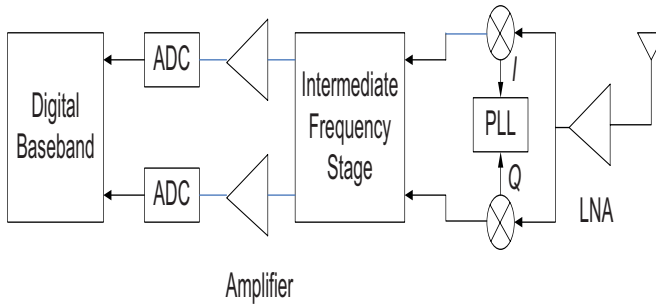


Figure 2.6: *Simplified block diagram of a superheterodyne receiver.*

behavioral modeling [72]. The behavioral modeling implies that the system model of a real DAC is implemented, which, means that the operations taking place in the real DAC are imitated in the simulation model. We consider a thermometric coded DAC in which each element consists of a resistance divider as shown in Figure 2.7. The resistance divider stages are labeled as RD. In this type of DAC the digital input word is fed into a decoder which connects to the appropriate voltage level. Since the voltage levels are provided by resistance divider stages, the noise due to resistance cannot be neglected especially at higher frequencies such as 60 GHz. Therefore, the noise due to resistance is also taken into account. The resistance noise is modeled as AWGN with zero mean and variance

$$\sigma_R^2 = 4 \cdot 1.38 \times 10^{-23} \cdot T \cdot R \cdot B, \quad (2.21)$$

where T is the temperature in Kelvin, R the resistance value in Ohm (Ω) and B represents the signal bandwidth in Hz. Assuming a room temperature of 290 Kelvin, a combined resistance of 50 Ω and a circuit operating at 1 GHz, we get $\sigma_R^2 = 8.004 \times 10^{-10}$ W. A real DAC, therefore, has an associated Gaussian noise in addition to additive quantization noise [72]. The normalized transfer characteristics of a 2 bit DAC are shown in Figure 2.8, in which the normalized output voltage is plotted against the normalized input (the input is in the form of discrete words) for a 2 bit DAC. It also draws a comparison between ideal DAC characteristics versus the real DAC. Due to the influence of resistive noise the output voltage levels fluctuate from the desired level. It is worthwhile to

notice here the last two extreme steps of the DAC have no Gaussian noise. This is because at those steps the DAC output is directly connected to a regulated voltage supply.

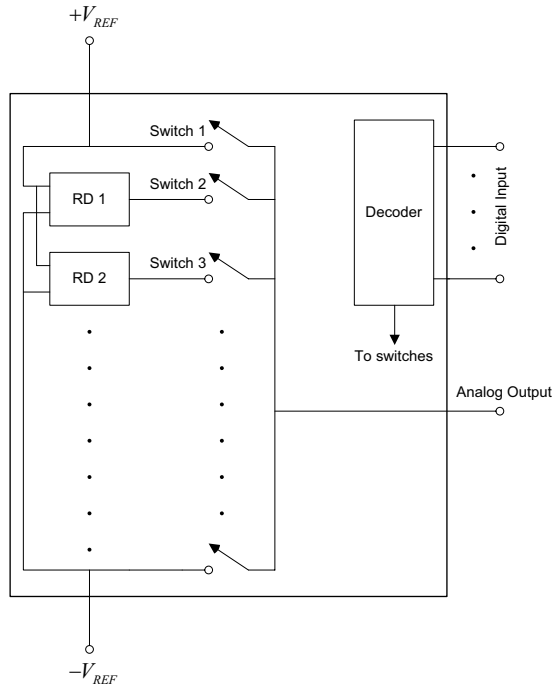


Figure 2.7: A simplified thermometric coded DAC schematic.

2.3.2 ADC Model

The ADC does the reverse operation of the DAC, i.e., it converts an analog voltage signal into a digital word that can be processed digitally. Here again, we consider a realistic ADC based on behavioral modeling [72]. The flash ADC is one of the popular high speed ADC architectures and is considered here. A simplified diagram of the flash ADC is shown in Figure 2.9. It consists of a number of voltage references which are assumed to be created by a number of resistance divider stages (RD) as in the case of the DAC. Each of the RD stages is connected to an operational amplifier which is configured as a comparator. Each comparator compares the input voltage with the reference voltage provided

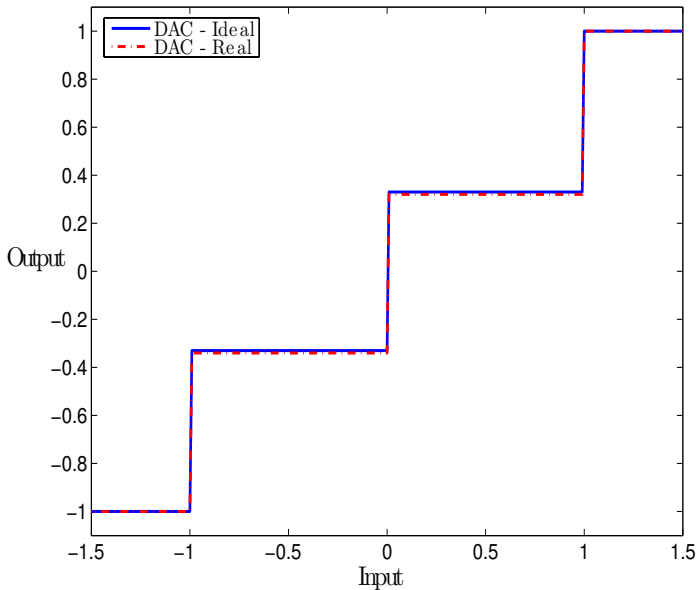


Figure 2.8: *Transfer characteristics of a thermometric coded DAC.*

by the RD network. Each comparator is connected to a decoding stage which outputs a digital word. Similar to the DAC, these voltage references give rise to noise at higher frequencies which in turn produces non-uniform quantization levels (commonly known as differential non-linearity (DNL)) and an offset as depicted in Figure 2.10. Figure 2.10 gives the normalized transfer characteristics of a 3 bit ADC, in which the normalized output voltage is plotted against the input (the output in this case is a discrete word). In our modeling it is assumed that there are no missing codes. It can be seen that the ideal ADC characteristics due to resistance noise deviates from the ideal ADC transfer characteristic. As in case of the DAC each resistance divider stage is assumed to have a combined resistance of 50Ω and the noise variance of each stage is given by equation (2.21). In the remaining part of the thesis, the ADC is assumed to have an offset of 0.05 V^2 , with a maximum operating voltage of 1 V .

2.3.3 Phase Noise Model

In an ideal scenario, the mixers are fed with a noise free local oscillator signal whose phase is perfectly in sync with the received carrier wave. This results in an ideal down conversion with the signal being attenuated only due to the

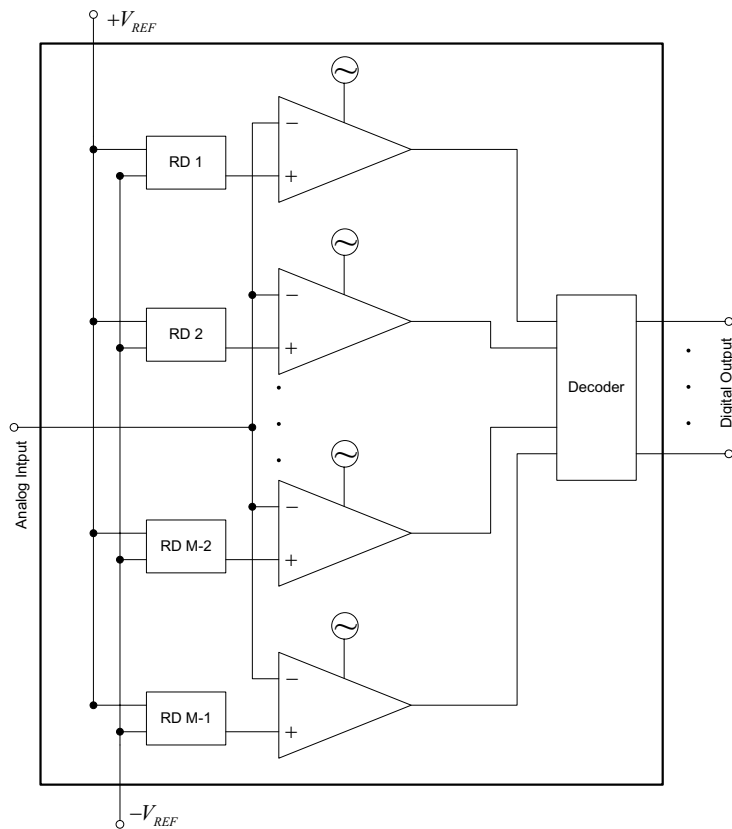


Figure 2.9: A simplified flash ADC schematic.

channel. However, in practice, especially at 60 GHz, this is not the case. The local oscillators are usually noisy and perfect phase recovery is not possible. This gives rise to additional attenuation and distortion due to the non-ideal down conversion process. Therefore, a model is required to investigate the impact of oscillator phase noise on the performance of digital transmission schemes. A number of local oscillator designs for operation in the 60 GHz band have been proposed [73] and mathematical models that emulate them have been outlined [74]. In our system we assume that the phase is tracked with a 60 GHz phase locked loop (PLL). The oscillator phase noise is often correlated and gives rise to a particular power spectral density (PSD) (instead of a Dirac pulse at the carrier frequency). In our analysis we consider the phase noise model proposed in [74]. This model is

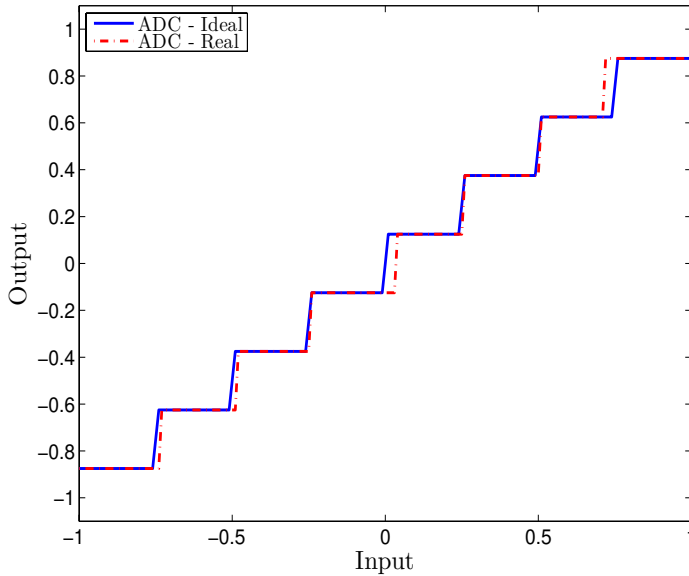


Figure 2.10: *Transfer characteristics of a flash ADC.*

well known to model 60 GHz phase noise characteristics [73]. As explained before the phase noise is correlated and hence completely specified by its PSD. The PN PSD is usually characterized with 3 parameters [74], i.e.,

- total double sided integrated PSD denoted by K_p dBc.
- PN spectrum bandwidth given by f_o Hz.
- the noise floor represented by \mathcal{L} dBc/Hz.

as shown in Figure 2.11. Three PN models each with $f_o = 1$ MHz, $\mathcal{L} = -120$ dBc/Hz (PN1), $\mathcal{L} = -125$ dBc/Hz (PN2) and $\mathcal{L} = -130$ dBc/Hz (PN3), and a K_p of -16 dBc, -20 dBc and -24 dBc, respectively, are considered. These models match quite well with the measured phase noise spectra of a 60 GHz phase locked loops (PLLs) [75]. The PSDs PN1, PN2 and PN3 are shown in Figure 2.11. All the three PN models outlined here assume a carrier transmission frequency of 60 GHz and a system operating bandwidth of 2 GHz.

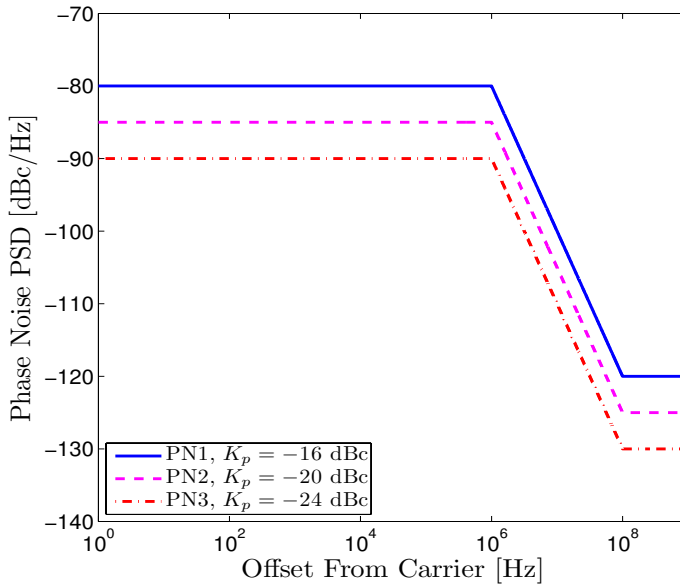


Figure 2.11: *Transfer characteristics of phase noise.*

2.3.4 I/Q Imbalance Model

Signal transmission on wireless communication channels is usually carried out using two orthogonal carriers on a single carrier frequency to boost the spectrum efficiency. These branches are commonly referred to as the in-phase (I) and the quadrature-phase (Q). Since both of the carriers are orthogonal if the carrier phase and amplitude are matched, at the receiver an ideal down conversion, i.e., separation of the in-phase and quadrature-phase component, is possible. This, however, is not the case in real systems where there is a slight amplitude and phase mismatch between the two carriers. In ideal conditions I/Q mixing produces a pure translation of the input frequency spectrum by the local oscillator frequency in either positive or negative direction. However, in practice, a leakage occurs from the in-phase branch to the quadrature-phase branch and vice versa. This has strong implications on the practical communications receiver architectures and their performances. The mixing of the I/Q branches has severe repercussions on the digital baseband signal. The generalized model of I/Q imbalance, when looked at from a baseband perspective, distorts the amplitude and the phase. Therefore, a complex baseband vector \mathbf{a} in the presence of I/Q imbalance characterized by

amplitude imbalance ϵ and phase imbalance ϕ is given by

$$\alpha \mathbf{a} + \beta \mathbf{a}^\dagger,$$

where

$$\alpha = \frac{1 + \epsilon e^{-j\phi}}{2} \quad (2.22)$$

and

$$\beta = \frac{1 - \epsilon e^{j\phi}}{2}. \quad (2.23)$$

This implies that $\epsilon = 1, \phi = 0$ is the ideal situation. The values of the parameters ϵ and ϕ are generally dependent on the carrier frequency being used and the receiver architecture. Two direct conversion receiver architectures operating over a carrier frequency of 60 GHz and a bandwidth of 2 GHz have been reported in [76] and [77]. These architectures have an amplitude imbalance of 1 dB and 1.6 dB and a phase error of 4° and 6.5° [76, 77], respectively. Based on these reported measurements we use 4 I/Q models (IQ1 - IQ4) to investigate the impact of I/Q imbalance as shown in Table 2.3.

Table 2.3: *I/Q imbalance parameters for 60 GHz transceivers.*

I/Q Model	ϵ	ϕ
IQ1	1.0 dB	4°
IQ2	1.0 dB	7°
IQ3	1.6 dB	4°
IQ4	1.6 dB	7°

2.3.5 Amplifier Nonlinearity Model

An amplifier in its ideal form should linearly scale the signal present at its input. Amplifiers generally tend to be linear as long as they are not operated at or close to their saturation region. However, as the operating point of the amplifier is moved closer to its saturation region, it starts exhibiting nonlinear gain. On the other hand the amplifier efficiency is considerably enhanced by moving the operating point close to the saturation region. For 60 GHz transceivers, that are fabricated in low cost CMOS technology, the amplifiers have a very narrow linear region and also for efficient power utilization it is more viable to operate the amplifier with

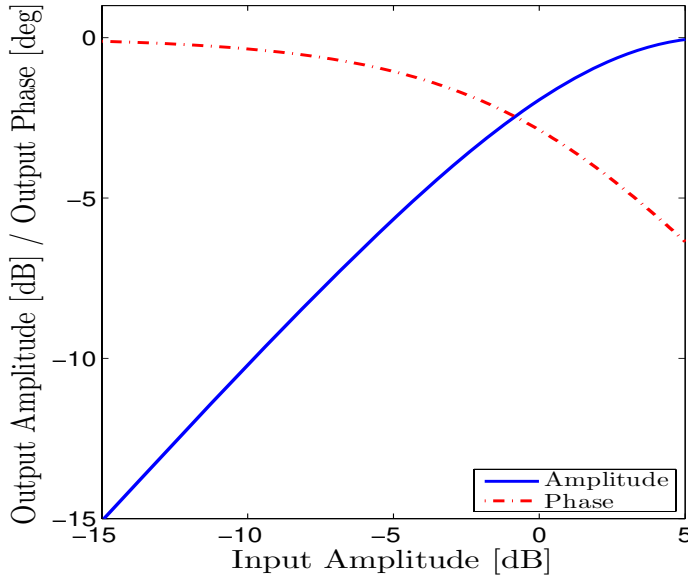


Figure 2.12: Phase and amplitude transfer characteristics of a nonlinear amplifier.

as small a back-off¹ as possible. The input back-off (IBO) of an amplifier is given as

$$\text{IBO} = \frac{a_{max}^2}{\langle P_{in} \rangle}, \quad (2.24)$$

where $\langle P_{in} \rangle$ denotes the average input power. The effect of this non-linearity can be modeled by the input amplitude to output amplitude (IA/OA) and input amplitude amplitude and output phase (IA/OP) transfer characteristics of the amplifier. A generalized IA/OA and IA/OP relation for a nonlinear amplifier, when supplied with a complex input signal $a = |a|e^{j\phi_a}$, is denoted by $f(a)$ and $g(a)$ respectively. The amplifier output is given by

$$a_{out}(a) = af(a)e^{jg(a)} \quad (2.25)$$

¹The back-off refers to the amount the amplifier is operated below its saturation region. For example, if an amplifier goes in saturation at an input of 0 dB, then it can be operated at an input of -5 dB, thus giving an input back-off of 5dB.

The input/output amplitude and phase relations for a typical power amplifier according to the Saleh's model [78] are given as

$$f(a) = \frac{\alpha_f}{1 + \beta_f |a|^2} \quad (2.26)$$

and

$$g(a) = \frac{\alpha_g |a|^2}{1 + \beta_g |a|^2}, \quad (2.27)$$

respectively. The parameters $\alpha_f, \beta_f, \alpha_g$ and β_g are device specific and are usually found by performing a minimum mean square curve fitting procedure [78]. Typical values for the amplifier model parameters are taken to be $\alpha_f = 1, \beta_f = 0.25, \alpha_g = \pi/50$ and $\beta_g = 0.25$ [79]. The normalized input/output relations for the given power amplifier parameters are shown in Figure 2.12, and are seen to be in good agreement with proposed 60 GHz HPA/LNA amplifier designs [80]. In [80], the system parameters were measured at a center frequency of 60 GHz.

2.4 Conclusions

In this chapter various frequency flat and frequency selective fading channel models, that can represent various 60 GHz transmission scenarios, were presented. Certain statistical channel properties such as amount of fading, RMS delay spread and the Rician K factor, were explained. Simplified tapped delay line based models, that will be used in subsequent chapters to investigate the system performance, were also presented. 60 GHz specific transfer characteristics for ADC, DAC, PN, I/Q imbalance and amplifier non linearity, were also outlined.

Chapter 3

Impact of RF Imperfections on Single-Carrier and Multi-Carrier Systems

This chapter compares the performance of single-carrier and multi-carrier based transmission schemes in the presence of RF impairments in 60 GHz transmission scenarios. The RF impairments and channel models introduced in Chapter 2 are utilized. The overall complexity of the single-carrier and multi-carrier schemes is computed and compared. It is shown that both the single-carrier and multi-carrier schemes while, having the same overall system complexity, react differently to multi-path fading and RF circuit imperfections.

3.1 Introduction

Multi-carrier (MC) and single-carrier schemes are two practical alternatives for high data rate communication in the 60 GHz band, and are currently under consideration by the IEEE 802.15.3c task group. Both schemes provide effective mitigation of ISI with reasonable implementation complexity. The multi-carrier scheme employs a number of orthogonal carriers for the transmission of the digital baseband symbols. The modulation of baseband symbols on multiple carriers can be accomplished by hardware mixers or in the digital domain. Since the implementation of mixers makes the front end design prohibitively complex and expensive, especially when a large number of carriers are required, digital mixing is preferred. Therefore, many current systems such as the IEEE 802.11 employ the inverse discrete fourier transform (IDFT) for mixing with the orthogonal sub-carriers. The received multi-carrier signal is then passed through the DFT block and equalized before being passed to the symbol detector. Traditionally the single-carrier schemes were overlooked, especially for severe ISI channels. The primary reason being the high implementation complexity. In most cases a finite impulse response filter whose coefficients were adjusted to equalize the effects of ISI was utilized. This required the convolution of the incoming signal with the equalization filter impulse response which was a computationally intense process. Therefore, this was abandoned in favor of the multi-carrier scheme. However, recently it was shown that by transforming the received signal to the frequency domain using the DFT one can in principle achieve the computational complexity comparable to the multi-carrier scheme. This scheme was thus referred to as the single-carrier with frequency domain equalization (SC-FDE). Subsequently, throughout the rest of this chapter single-carrier and SC-FDE will be used interchangeably. From an implementation perspective the main difference between the two schemes is the DFT block. In MC scheme the IDFT is done prior to transmission and DFT is performed at the receiver, whereas in the SC-FDE scheme both the DFT and IDFT operations are carried out at the receiver. A detailed description of both these schemes will be presented in the subsequent sections.

Although both the MC and SC-FDE schemes counter the ISI at a reasonable implementation complexity their sensitivity to RF circuit impairments in 60 GHz transmission scenarios has to be investigated. A number of comparisons between multi-carrier and single-carrier schemes can be found in literature [35–38].

Single-carrier has a lower peak-to-average-power ratio (PAPR), and is more resistant to frequency offset errors as compared to the multi-carrier scheme [36]. The block based processing for the single-carrier scheme is known to achieve maximum diversity, irrespective of the block length [36], and therefore outperforms the multi-carrier scheme in un-coded scenarios. For code rates $R_c \leq 1/2$, both schemes have the same performance in multi-path fading channels [36]. This is also confirmed, still assuming an ideal front-end, for 60 GHz transmission scenarios [37]. The single-carrier scheme was shown to require a lower IBO for the high power amplifier (HPA) and has a similar sensitivity to PN and I/Q imbalance for IEEE 802.11 transmission scenarios [38]. The operating parameters for 60 GHz RF circuits are expected to be different from IEEE 802.11 due to a large number of sub-carriers and more severe multi-path conditions.

In this chapter, the impact of RF circuit imperfections on multi-carrier and single-carrier schemes is investigated. The RF imperfections considered are: quantization due to DACs and ADCs, the nonlinearities due to HPA, phase noise and I/Q imbalance. The power penalty for single-carrier and multi-carrier schemes, i.e., the SNR degradation as a function of BER for various DAC/ADC word lengths, HPA IBO values, phase noise values and I/Q imbalance values is presented.

The chapter organization is as follows. The system models for the MC and SC-FDE transmission schemes are introduced in Section 3.2. The overall system complexity of the MC and the SC-FDE is computed and compared in Section 3.3. The degradation in system performance for MC and SC-FDE schemes due to DAC is given in Section 3.4, while the same comparison for ADC is presented in Section 3.5. Sections 3.6 and 3.7 outline the impact of phase noise and I/Q imbalance on their performance. In Section 3.8 the impact of amplifier non linearity on the performance of MC and SC-FDE is investigated. Based on the impact of RF imperfections, the chapter concludes with a 60 GHz system design summary which is presented in Section 3.9.

3.2 System Models

3.2.1 Multi-carrier based System

The basic idea behind multi-carrier transmission schemes is to split the incoming (high data rate) stream into a number of (low data rate) sub-streams. These

low data rate sub-streams are then simultaneously transmitted over orthogonal sub-channels. This effectively converts a wideband channel into a number of orthogonal narrow band sub-channels. The number of sub-channels are chosen such that the bandwidth of each sub-channel is less than the coherence bandwidth of the radio channel. This also ensures that each sub-channel experiences relatively flat fading and thus the ISI on each sub-channel is small.

Multi-carrier modulation can be efficiently implemented in the digital domain using the inverse and forward fast Fourier (IFFT/FFT) transforms. This FFT/IFFT based digital implementation, when used in conjunction with a cyclic prefix, is commonly referred to as OFDM [65]. In the OFDM based MC system of Figure 3.1, the mapped N -symbol data vector

$$\mathbf{x} = (x_0, x_1, \dots, x_{N-1}), \quad (3.1)$$

is passed through an inverse fast Fourier transform (IFFT) block to produce an OFDM block

$$\mathbf{X} = (\mathcal{F}_0^{-1}(\mathbf{x}), \dots, \mathcal{F}_{N-1}^{-1}(\mathbf{x})), \quad (3.2)$$

where

$$\mathcal{F}_k^{-1}(\mathbf{x}) = \frac{1}{N} \sum_{n=0}^{N-1} x_n e^{j2\pi \frac{kn}{N}}. \quad (3.3)$$

Mapping here refers to the selection of a complex point from a two dimensional M -ary signal constellation such as QPSK or 8PSK i.e. $x_i \in \{s_0, \dots, s_{M-1}\}$, where s_0, \dots, s_{M-1} denote complex signal constellation points. The OFDM block length N is chosen such that the OFDM block time

$$T_N = \frac{N}{B} = NT_s, \quad (3.4)$$

is much larger than the channel delay spread. The system bandwidth is denoted as B and T_s denotes the system sampling time. Prior to transmission, a cyclic prefix (CP) is added to the OFDM block which mitigates inter-block interference (IBI) between adjacent OFDM symbols and simplifies equalization requirements. The CP, which consists of the last Z samples of the OFDM block is chosen larger than the maximum channel delay spread i.e. $Z \geq N_{max}$, where $N_{max} = \lceil \tau_{max}/T_s \rceil$ gives the maximum channel delay spread in samples. The OFDM block after CP

insertion is given as

$$\mathbf{X}^C = (X_{N-Z}, X_{N-Z+1}, \dots, X_{N-1}, X_0, X_1, \dots, X_{N-1}). \quad (3.5)$$

Assuming an ideal front end, the received vector after passing through the channel is given as

$$\mathbf{Y}^C = \mathbf{X}^C * \mathbf{h} + \mathbf{n}^C, \quad (3.6)$$

where \mathbf{n}^C is a vector of Gaussian noise samples with zero mean and variance $N_0/2$. The CP removal converts linear convolution into circular convolution

$$\mathbf{Y} = \mathbf{X} \otimes \mathbf{h} + \mathbf{n}, \quad (3.7)$$

where \mathbf{Y} denotes the vector with the CP removed. The vector \mathbf{Y} is then passed through the FFT block whose output is denoted by \mathbf{y} . The samples of vector \mathbf{y} are given as

$$y_m = x_m \mathcal{F}_m(\mathbf{h}) + \mathcal{F}_m(\mathbf{n}), \quad (3.8)$$

where

$$\mathcal{F}_m(\mathbf{h}) = \sum_{n=0}^{N-1} h_n e^{-j2\pi \frac{mn}{N}}. \quad (3.9)$$

Assuming perfect channel state information (CSI) at the receiver, a simple (but sub-optimum) equalization strategy is to perform a point wise division of the FFT output by the estimated channel transfer function, i.e.,

$$\hat{x}_m = \frac{y_m}{\mathcal{F}_m(\mathbf{h})} = x_m + \frac{\mathcal{F}_m(\mathbf{n})}{\mathcal{F}_m(\mathbf{h})}. \quad (3.10)$$

The equalized symbol vector $\hat{\mathbf{x}}$ is then passed to a maximum likelihood (ML) detector that operates on a symbol by symbol basis. The parameters of a 60 GHz OFDM based transceiver are summarized in Table 3.1. The performance of an OFDM system with quadrature phase shift keying (QPSK) and 8PSK signal constellations for an ideal front end is shown in Figure 3.2.

3.2.2 Single-carrier based System

In traditional single-carrier based systems, ISI must be countered using equalization techniques. Channel equalization when carried out in the time domain is computationally very intensive and becomes too complex for channels with se-

	Multi-carrier	Single-carrier
Carrier frequency	60 GHz	60 GHz
Modulation scheme	QPSK / 8PSK	QPSK / 8PSK
Channel bandwidth	1 GHz	1 GHz
# of sub-carriers / block length	1024	1024
Cyclic prefix length (L)	100	100

Table 3.1: *Single-carrier and multi-carrier system parameters.*

vere ISI and high symbol rates. Recently, This limitation of single-carrier based systems was the primary reason for choosing OFDM as the preferred modulation scheme in ADSL and WLAN standards [81]. Recently, this limitation of the single-carrier scheme has been overcome with the introduction of frequency domain equalization (FDE) [31, 32]. The idea is quite similar to the one used for equalization in OFDM system with the only difference being the placement of the IFFT block at the receiver instead of at the transmitter. The system block diagram of a single-carrier based transceiver is shown in Figure 3.3. The mapped data symbol vector

$$\mathbf{x} = (x_0, x_1, \dots, x_{N-1}), \quad (3.11)$$

is added with a CP of length Z prior to transmission. The vector to be transmitted is thus given by

$$\mathbf{x}^C = (x_{N-Z}, x_{N-Z+1}, \dots, x_{N-1}, x_0, x_1, \dots, x_{N-1}). \quad (3.12)$$

Assuming an ideal front end, the received signal vector after passing through the channel is given by

$$\mathbf{r}^C = \mathbf{x}^C * \mathbf{h} + \mathbf{n}^C. \quad (3.13)$$

The received vector \mathbf{r} after CP removal is given by

$$\mathbf{r} = \mathbf{x} \otimes \mathbf{h} + \mathbf{n}. \quad (3.14)$$

The vector at the output of the FFT block is denoted by \mathbf{Y} . The samples of vector \mathbf{Y} are given as

$$Y_m = \mathcal{F}_m(\mathbf{h})\mathcal{F}_m(\mathbf{x}) + \mathcal{F}_m(\mathbf{n}). \quad (3.15)$$

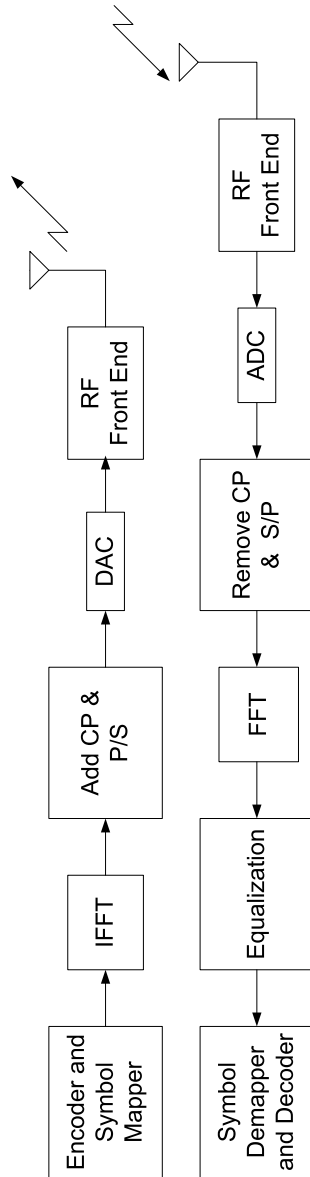


Figure 3.1: *A simplified system model for a multi-carrier based transceiver.*

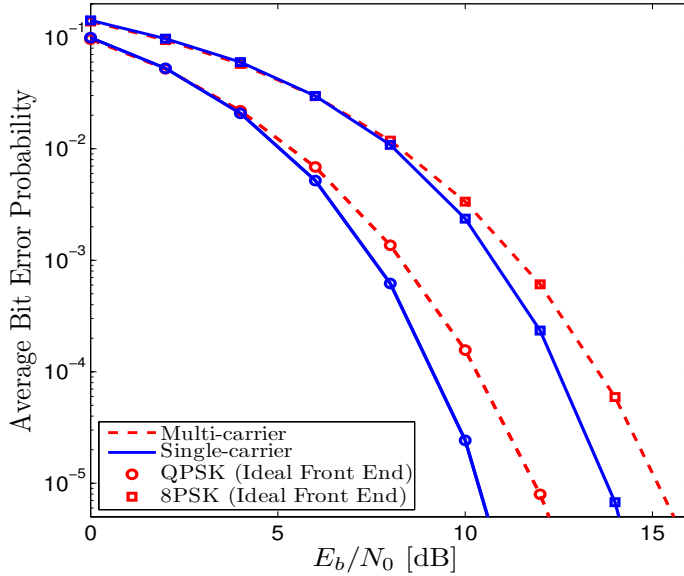


Figure 3.2: Performance of multi-carrier and single-carrier based transceivers at 60 GHz employing QPSK/8PSK constellations for an ideal front end.

Assuming perfect CSI at the receiver, then a simple (but sub-optimum) equalization strategy is to perform a point wise division of the FFT output by the estimated channel transfer function, i.e.,

$$\hat{Y}_m = Y_m / \mathcal{F}_m(\mathbf{h}) = \mathcal{F}_m(\mathbf{x}) + \frac{\mathcal{F}_m(\mathbf{n})}{\mathcal{F}_m(\mathbf{h})}. \quad (3.16)$$

The components of the vector $\hat{\mathbf{x}}$ after IFFT operation are given as

$$\hat{x}_m = x_m + \mathcal{F}_m^{-1}(\mathbf{N}), \quad (3.17)$$

where

$$\mathbf{N} = (\mathcal{F}_0(\mathbf{n})/\mathcal{F}_0(\mathbf{h}), \dots, \mathcal{F}_{N-1}(\mathbf{n})/\mathcal{F}_{N-1}(\mathbf{h})). \quad (3.18)$$

The estimated data symbol vector $\hat{\mathbf{x}}$ is then passed to an ML detector. The parameters for a 60 GHz SC-FDE are given in Table 3.1. It can be seen from Figure 3.2 that the single-carrier scheme exhibits a superior performance in terms of BER, as compared to the multi-carrier scheme. This is due to the difference in the signal processing being carried out the transmitter and the receiver. As

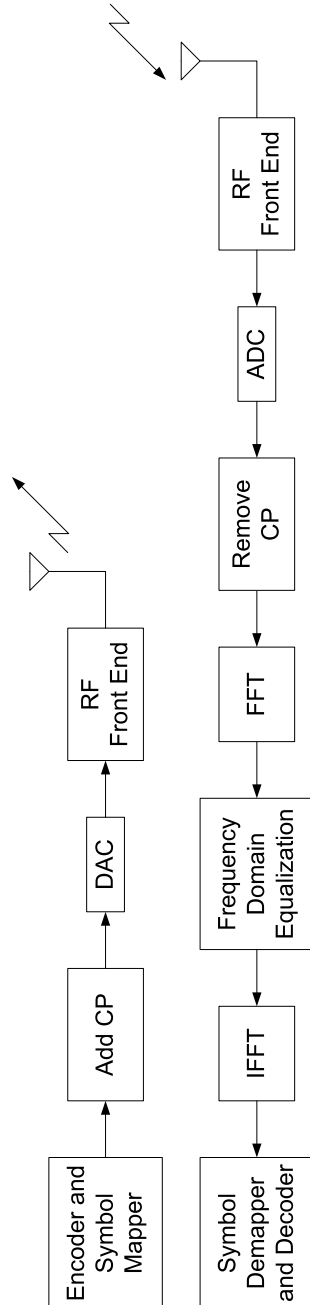


Figure 3.3: A simplified system model for a single-carrier based transceiver.

explained before, each baseband modulated symbol in the multi-carrier scheme is transmitted on its orthogonal sub-carrier. Therefore, each sub-carrier experiences flat fading, which can severely deteriorate the system performance, especially if the channel has deep fades. On the other hand in a single-carrier scheme one baseband modulated symbol is transmitted over the entire system bandwidth, the single-carrier scheme therefore, performs better as compared to the multi-carrier scheme.

3.2.3 Single-carrier and multi-carrier modulation with RF Imperfections

The received signal after equalization in both the single-carrier and multi-carrier schemes is the sum of the original transmitted signal x_m and a noise term. This however, is not the case in the presence of RF circuit imperfections. The samples of the received symbol $\hat{\mathbf{x}}$, after CP removal and equalization in the presence of RF imperfections, can be written as

$$\hat{x}_m = \kappa_m x_m + \zeta_m + \eta_m, \quad (3.19)$$

where κ_m and ζ_m are impairment and transmission scheme dependent multiplicative and additive terms, η_m is due to additive white Gaussian noise (AWGN) and x_m is a sample from the original transmitted vector \mathbf{x} . The factors κ_m and ζ_m depend on the type of impairment and the transmission scheme and will be explained in subsequent sections. For some impairments such as DAC noise κ_m and ζ_m are independent, while for others, e.g. phase noise, they are not. The vector $\hat{\mathbf{x}}$ is then passed to a maximum likelihood (ML) detector that works on a symbol by symbol basis. For MC transmissions, η_m is given as

$$\eta_m = \frac{\mathcal{F}_m(\mathbf{n})}{\mathcal{F}_m(\mathbf{h})}, \quad (3.20)$$

and for SC based systems

$$\eta_m = \mathcal{F}_m^{-1}(\mathbf{N}). \quad (3.21)$$

3.3 System Complexity

There exist a number of measures to assess the system complexity. For example, in computer science the complexity of a system is normally determined by the number of computational resources required to specify the object. The object in this

case can be a piece of text or a number. This complexity is commonly referred to as the Kolmogorov complexity. In digital signal processing multiply-accumulate is a commonly used operation which refers to the process of multiplying two numbers and then adding the result to an accumulator. Since most of the baseband processing schemes for multi-carrier and single-carrier modulation are implemented in the digitally it is worthwhile to measure the complexity of both schemes in terms of multiply-and-accumulate operations for comparison purposes.

Denoting N_{MA} as the number of multiply-and-accumulate (MA) operations required for the processing of one block of symbols of length N , as is shown in [35], that an FFT/IFFT operation can be implemented by $0.75N \log_2 N$ real N_{MA} operations. The channel is inverted by the equalizer with a complex multiplication for each sub-carrier that can be achieved using 3 real multiplications per sub-carrier. The complexity of the OFDM and single-carrier schemes are summarized in Table 3.2.

It is interesting to note here that OFDM system complexity is divided between the transmitter (TX) and the receiver (RX), whereas the single-carrier based system complexity is solely concentrated at the receiver side. This makes OFDM a good candidate (in terms of implementation complexity) for broadcast systems in which the main idea is to have one main hub or broadcaster such as in high definition television (HDTV) transmission and multiple receivers. In case of symmetric links in which every node in the system should be capable of transmission and reception it does not matter from a complexity point of view whether a multi-carrier or a single-carrier scheme is used. In the following sections we outline the impact

OFDM	SC-FDE	MA operation block	N_{MA}
TX	RX	IFFT	$0.75N \log_2 N$
RX	RX	FFT	$0.75N \log_2 N$
RX	RX	Equalization	$3N$
		Total	$1.5N \log_2 N + 3N$

Table 3.2: *Complexity of multi-carrier and single-carrier based systems.*

of DAC, ADC, PN, I/Q imbalance and amplifier imperfections on the performance of MC and SC schemes. The RF circuit imperfection models introduced in the last chapter are utilized. The simplified TDL channel models introduced in the last section are used for representing 60 GHz transmission scenarios. Two schemes, i.e., QPSK and 8PSK are used as candidate baseband modulation techniques.

3.4 Impact of DAC

The received signal for a multi-carrier scheme, employing a real DAC at the transmitter, after CP removal is given as

$$\mathbf{Y} = \tilde{\mathbf{X}} \otimes \mathbf{h} + \mathbf{n}, \quad (3.22)$$

where $\tilde{\mathbf{X}} = \mathbf{X} + \mathbf{p}^M$ and \mathbf{p}^M is an addition of two vectors i.e. $\mathbf{p}^M = \mathbf{q}^M + \mathbf{t}$ which consist of uniformly distributed quantization noise components q_n^M and a zero mean AWGN components t_n with variance σ_t^2 . The quantization noise q_n^M is uniformly distributed [82, p.35] between $(-b \cdot \Delta^{\mathcal{M}^D}, +b \cdot \Delta^{\mathcal{M}^D})$, where

$$\Delta^{\mathcal{M}^D} = \max \{ \max |\Re[\mathbf{X}]|, \max |\Im[\mathbf{X}]| \}, \quad (3.23)$$

$$b = 1/(2^{N_{DAC}} - 1), \quad (3.24)$$

N_{DAC} denotes the number of DAC bits, $\Re[\cdot]$ and $\Im[\cdot]$ represent the real and imaginary part of a signal and $\mathbf{X} = (\mathcal{F}_0^{-1}(\mathbf{x}), \dots, \mathcal{F}_{N-1}^{-1}(\mathbf{x}))$. It is assumed that no signal clipping occurs, i.e., it is assumed that the DAC's operating range is fully matched to the signal's dynamic range. The samples of the received vector after FFT and equalization are then given as

$$\hat{x}_m = x_m + \mathcal{F}_m(\mathbf{p}^M) + \frac{\mathcal{F}_m(\mathbf{n})}{\mathcal{F}_m(\mathbf{h})}. \quad (3.25)$$

The multiplicative and additive terms are thus given as

$$\kappa_m = 1$$

and

$$\zeta_m = \mathcal{F}_m(\mathbf{p}^M).$$

For a single-carrier based system, the received signal after CP removal and equalization in the presence of a real DAC is given as

$$\hat{x}_m = x_m + p_m^S + \mathcal{F}_m^{-1}(\mathbf{N}), \quad (3.26)$$

where $p_m^S = q_m^S + t_m$, t_m is the same as given in case of the multi-carrier scheme and q_m^S is the quantization noise uniformly distributed [82, p.35] between

$(-b \cdot \Delta^{SD}, +b \cdot \Delta^{SD})$ and

$$\Delta^{SD} = \max \{ \max |\Re[\mathbf{x}]|, \max |\Im[\mathbf{x}]| \}. \quad (3.27)$$

The multiplicative and additive terms are thus given as

$$\kappa_m = 1$$

and

$$\zeta_m = p_m^S.$$

In a multi-carrier system, \mathbf{X} has a higher dynamic range due to the IFFT operation, whereas in case of a single-carrier scheme \mathbf{x} has a relatively low dynamic range. Therefore, $\Delta^{MD} > \Delta^{SD}$ which means that a lower variance is found for q_m^S as compared to q_m^M and thus a higher number of bits are required in a multi-carrier system to reduce the impact of quantization.

Figure 3.4 shows SNR degradation (Δ_{SNR}) as a function of BER for single-carrier and multi-carrier schemes using QPSK and 8PSK constellations for different values of N_{DAC} . It can be seen that in order to achieve a Δ_{SNR} of less than 1 dB at a BER of 10^{-4} , a 1 bit DAC is required for single-carrier with QPSK whereas 5 bits are needed for multi-carrier with QPSK. It can also be seen that for a 4 bit DAC resolution multi-carrier 8PSK performs 5.5 dB worse than the single-carrier 8PSK scheme at a BER of 10^{-4} .

3.5 Impact of ADC

The received signal for a multi-carrier scheme, employing a real ADC, after CP removal is given as

$$\mathbf{Y} = \mathbf{X} \otimes \mathbf{h} + \mathbf{q}^{AM} + \mathbf{n}, \quad (3.28)$$

where \mathbf{q}^M denotes additive quantization noise. It is assumed that no signal clipping occurs, i.e., it is assumed that the ADC's operating range is fully matched to the signal's dynamic range. The samples of the received vector after FFT and equalization are given as

$$\hat{x}_m = x_m + \frac{\mathcal{F}_m(\mathbf{q}^{AM})}{\mathcal{F}_m(\mathbf{h})} + \frac{\mathcal{F}_m(\mathbf{n})}{\mathcal{F}_m(\mathbf{h})}. \quad (3.29)$$

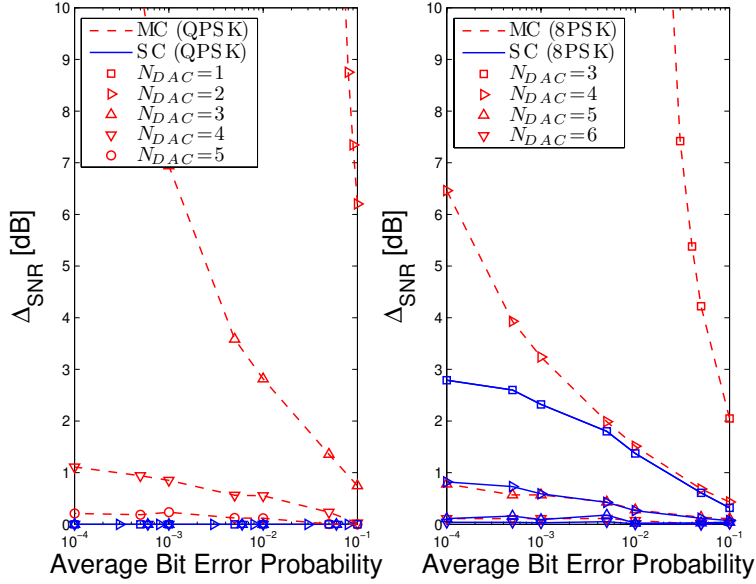


Figure 3.4: SNR degradation as a function of BER for various N_{DAC} values.

The multiplicative and additive terms are thus given as

$$\kappa_m = 1$$

and

$$\zeta_m = \frac{\mathcal{F}_m(\mathbf{q}^{\text{AM}})}{\mathcal{F}_m(\mathbf{h})}.$$

For a single-carrier based system, the received signal after CP removal and equalization in the presence of a real ADC is given as

$$\hat{x}_m = x_m + q_m^{\text{AS}} + \mathcal{F}_m^{-1}(\mathbf{N}), \quad (3.30)$$

where q_m^{AS} denotes additive quantization noise. The multiplicative and additive terms are thus given as

$$\kappa_m = 1$$

and

$$\zeta_m = q_m^{AS}.$$

Similar to the DAC, the received signal in case of a multi-carrier transmission has a higher dynamic range as compared to a single-carrier scheme. For a given number of bits the variance of \mathbf{q}^{AM} is greater than \mathbf{q}^{AS} which implies that the multi-carrier scheme will suffer more performance degradation as compared to the single-carrier scheme. Therefore, a higher number of quantization levels and ADC bits N_{ADC} are required for the multi-carrier scheme.

Figure 3.5 shows the Δ_{SNR} degradation against BER for various values of N_{ADC} using single-carrier and multi-carrier schemes employing QPSK and 8PSK constellations. Assuming that a BER of 10^{-4} with a maximum allowed Δ_{SNR} of 1 dB is required, single-carrier QPSK and single-carrier 8PSK schemes require 5 and 6 bits, respectively, whereas multi-carrier QPSK and multi-carrier 8PSK need 8 and 10 bits, respectively.

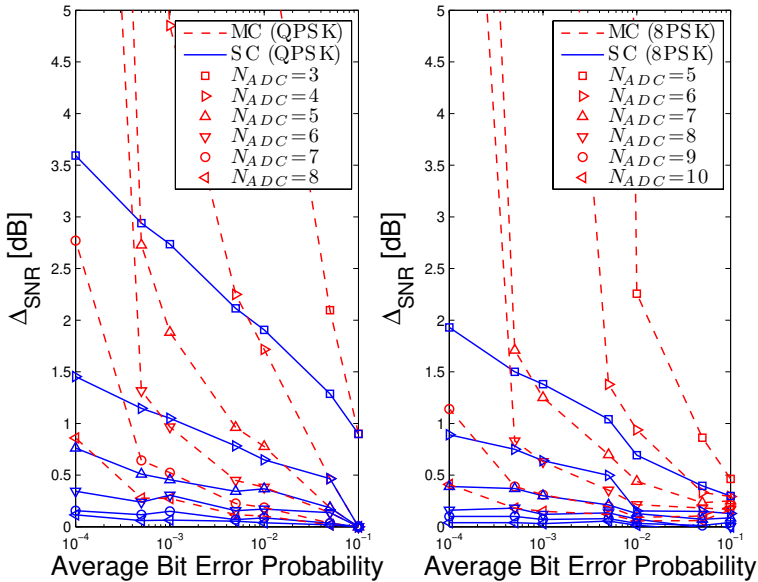


Figure 3.5: SNR degradation as a function of BER for various N_{ADC} values.

3.6 Impact of Phase Noise

The received signal for a multi-carrier system in the presence of transmitter phase noise, after CP removal is given as

$$\mathbf{Y} = \tilde{\mathbf{X}} \otimes \mathbf{h} + \mathbf{n}, \quad (3.31)$$

where $\tilde{\mathbf{X}}$ represents the phase noise perturbed OFDM block whose samples are given by

$$\tilde{X}_k = X_k e^{j\theta_k}, \quad (3.32)$$

and θ_k represents phase noise. After FFT and channel equalization the received signal is given by

$$\hat{x}_m = \mathcal{F}_m(\tilde{\mathbf{X}}) + \frac{\mathcal{F}_m(\mathbf{n})}{\mathcal{F}_m(\mathbf{h})}, \quad (3.33)$$

where $\mathcal{F}_m(\tilde{\mathbf{X}})$ can be written as

$$\mathcal{F}_m(\tilde{\mathbf{X}}) = \left(\frac{1}{N} \sum_{k=0}^{N-1} e^{j\theta_k} \right) x_m + \frac{1}{N} \sum_{n=0, n \neq m}^{N-1} \sum_{k=0}^{N-1} x_n e^{j2\pi(n-m)k/N} e^{j\theta_k}. \quad (3.34)$$

The multiplicative and additive terms are thus given by

$$\kappa_m = \frac{1}{N} \sum_{k=0}^{N-1} e^{j\theta_k} \quad (3.35)$$

and

$$\zeta_m = \frac{1}{N} \sum_{n=0, n \neq m}^{N-1} \sum_{k=0}^{N-1} x_n e^{j2\pi(n-m)k/N} e^{j\theta_k}, \quad (3.36)$$

respectively. From the above equations it can be seen that the multiplicative factor κ_m , is the same for all symbols and is referred to as the common phase rotation (CPR). The additive term ζ_m is a consequence of the orthogonality loss in the sub-carriers due to θ_k and is known as the inter-carrier interference (ICI). This additive term is seen to be dependent on the number of sub-carriers N , the mapped symbols \mathbf{x} and θ_k .

For a block based single-carrier scheme, the received signal after channel equalization is given by

$$\hat{x}_m = x_m e^{j\theta_m} + \mathcal{F}_m^{-1}(\mathbf{N}). \quad (3.37)$$

The interference terms are thus given as

$$\kappa_m = e^{j\theta_m}$$

and

$$\zeta_m = 0,$$

where θ_m denotes the phase noise. It can be seen from the above equations that for a single-carrier system the PN θ_m is directly multiplied with the baseband modulated symbol x_m . This results in rotation of the symbol constellation points. Since no orthogonal sub-carriers are involved in single-carrier transmission, there is no ICI and thus $\zeta_m = 0$.

The performance degradation in the multi-carrier scheme is due to the CPR κ_m and additive ICI ζ_m , whereas for the single-carrier scheme PN is directly multiplied with the transmitted symbol resulting in constellation rotation. For high phase noise variances and/or closely spaced constellation points the constellation clustering due to the ICI term in multi-carrier schemes can help to counter constellation rotation and thus give better performance as compared to the single-carrier scheme. For example consider an 8PSK constellation in the presence of a phase rotation of 23° but in the absence of AWGN. For multi-carrier schemes the additive interference will cluster the signal constellation resulting in correct detection of some mapped symbols, whereas in the single-carrier scheme no symbol will be correctly detected. This is depicted in Figure 3.6. Figure 3.7 gives the SNR degradation Δ_{SNR} as a function of BER for single-carrier and multi-carrier schemes using QPSK and 8PSK signal constellations. The multi-carrier QPSK scheme outperforms single-carrier QPSK by about 5.5 dB at a BER of 10^{-4} for a high phase noise variance i.e. PN1. For 8PSK, the multi-carrier scheme outperforms the single-carrier scheme even at low phase noise variances, for example at a low phase noise variance i.e. PN3, multi-carrier 8PSK performs 0.9 dB better than single-carrier 8PSK at a BER of 10^{-4} .

3.7 Impact of I/Q Imbalance

The received signal, for a multi-carrier scheme after CP removal, in the presence of I/Q imbalance at the transmitter is given by

$$\mathbf{Y} = \tilde{\mathbf{X}} \otimes \mathbf{h} + \mathbf{n}, \quad (3.38)$$

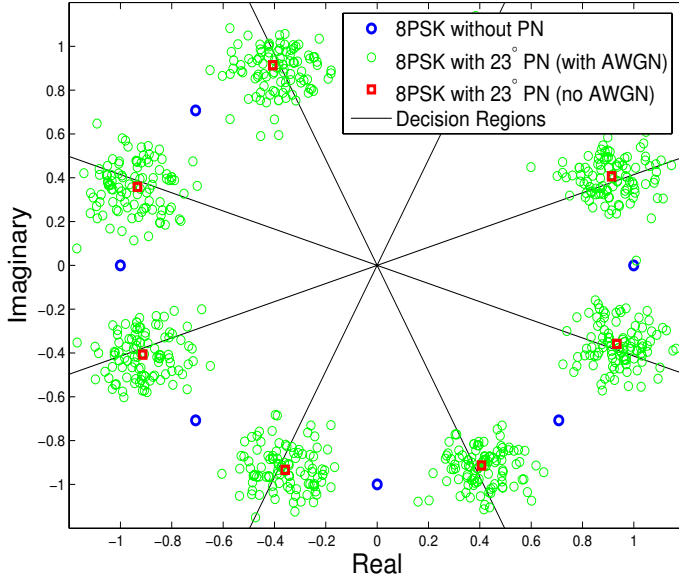


Figure 3.6: Impact of PN and AWGN on 8PSK signal constellation.

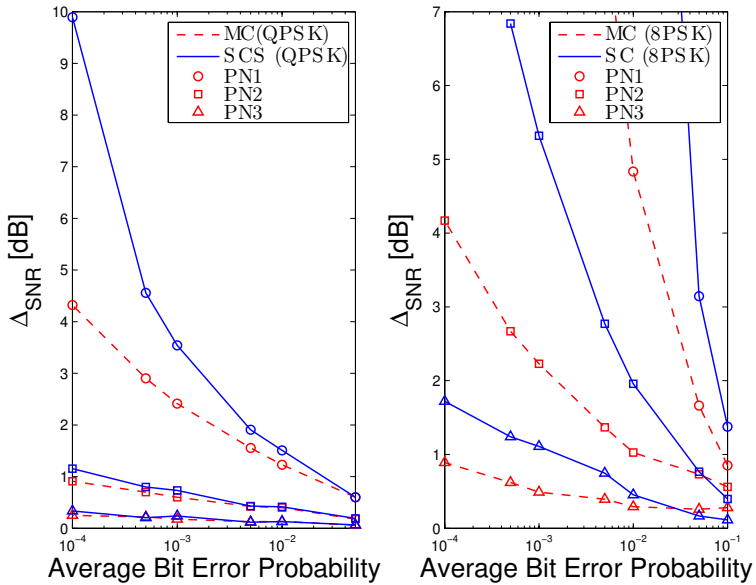


Figure 3.7: SNR degradation as a function of BER for various PN models.

where $\tilde{\mathbf{X}} = \alpha \mathbf{X} + \beta \mathbf{X}^\dagger$ and \dagger denotes the complex conjugate. The vector samples at the output of the FFT block after equalization are given by

$$\hat{x}_m = \alpha x_m + \beta \mathcal{F}_m(\mathbf{X}^\dagger) + \frac{\mathcal{F}_m(\mathbf{n})}{\mathcal{F}_m(\mathbf{h})}. \quad (3.39)$$

Therefore we get

$$\kappa_m = \alpha,$$

and

$$\zeta_m = \beta \mathcal{F}_m(\mathbf{X}^\dagger),$$

where $\mathbf{X} = (\mathcal{F}_0^{-1}(\mathbf{x}), \dots, \mathcal{F}_{N-1}^{-1}(\mathbf{x}))$. The baseband modulated symbol x_m in case of a multi-carrier scheme therefore experiences a common multiplication term (CMT) i.e. α which is the same for all symbols. This will have the effect of constellation rotation and contraction (since α is complex). An additional additive interference ζ_m will result in constellation clustering.

The received signal after CP removal and channel equalization for a single-carrier scheme is given by

$$\hat{x}_m = \alpha x_m + \beta x_m^\dagger + \mathcal{F}_m^{-1}(\mathbf{N}). \quad (3.40)$$

The multiplicative and additive terms are thus given as

$$\kappa_m = \alpha$$

and

$$\zeta_m = \beta x_m^\dagger.$$

Similar to the multi-carrier case the baseband modulated symbol in single-carrier will also undergo constellation rotation, contraction and clustering. It is interesting to note here that unlike the multi-carrier scheme the additive interference of any symbol is dependent only on that symbol and β , whereas for a multi-carrier scheme it depends on the β and the FFT of the modulated symbols, i.e., the interference is dependent on all the modulated symbols. In other words, the multi-carrier system is affected by ICI in the presence of I/Q imbalance.

The I/Q imbalance results in a CMT κ_m and an additive non zero term ζ_m for both the multi-carrier and the single-carrier case. While both schemes suffer from

the same CMT $\kappa_m = \alpha$, the additive term is different in both cases. Since \mathbf{X} has a higher dynamic range than \mathbf{x} , the ζ_m term is enhanced in case of multi-carrier and therefore results in a relatively worse performance for the multi-carrier scheme as compared to the single-carrier scheme.

The SNR degradation, as a function of the BER for single-carrier and multi-carrier schemes using QPSK and 8PSK constellations and for different I/Q parameters is shown in Figure 3.8. Single-carrier QPSK outperforms multi-carrier QPSK by about 0.7 dB at a BER of 10^{-4} , when $\epsilon = 1.0$ dB and $\phi = 4^\circ$. For 8PSK constellations both the single-carrier and the multi-carrier scheme exhibit very poor performance in the presence of I/Q imbalance and therefore must be used with some compensation algorithm to achieve satisfactory performance.

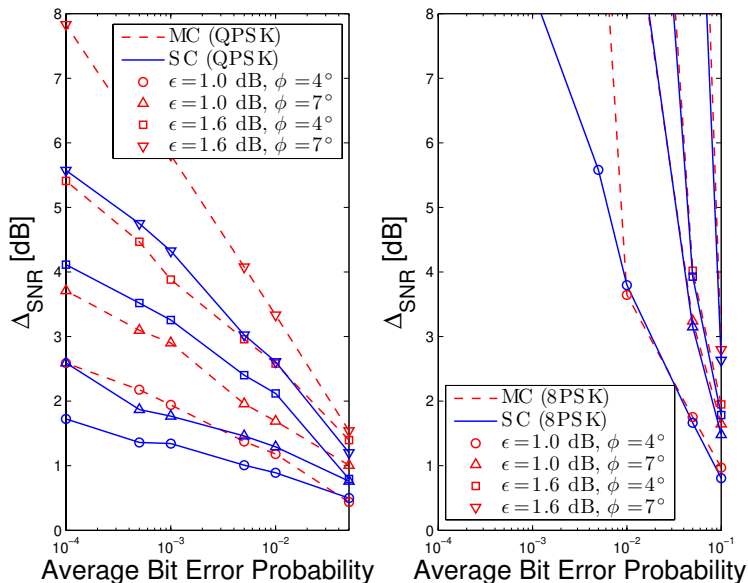


Figure 3.8: SNR degradation as a function of BER for various I/Q imbalance parameters.

3.8 Impact of Amplifier Non-linearity

The received multi-carrier signal, after CP removal and a nonlinear HPA is given by

$$\mathbf{Y} = \tilde{\mathbf{X}} \otimes \mathbf{h} + \mathbf{n}, \quad (3.41)$$

where the $\tilde{\mathbf{X}}$ is the OFDM symbol passed through a nonlinear amplifier, whose samples are given as

$$\tilde{X}_l = X_l f(X_l) e^{jg(X_l)}. \quad (3.42)$$

The vector samples at the output of the FFT block after equalization are given as

$$\hat{x}_m = \mathcal{F}_m(\tilde{\mathbf{X}}) + \frac{\mathcal{F}_m(\mathbf{n})}{\mathcal{F}_m(\mathbf{h})}, \quad (3.43)$$

where

$$\mathcal{F}_m(\tilde{\mathbf{X}}) = \left(\sum_{k=0}^{N-1} f(X_k) e^{jg(X_k)} \right) x_m + \sum_{n=0, n \neq m}^{N-1} x_n \sum_{k=0}^{N-1} f(X_k) e^{jg(X_k)} e^{j2\pi(n-m)k/N}. \quad (3.44)$$

This gives us

$$\kappa_m = \sum_{k=0}^{N-1} f(X_k) e^{jg(X_k)}$$

and

$$\zeta_m = \sum_{n=0, n \neq m}^{N-1} x_n \sum_{k=0}^{N-1} f(X_k) e^{jg(X_k)} e^{j2\pi(n-m)k/N}.$$

The baseband modulated symbol, therefore, experiences a common multiplicative term (CMT), i.e., κ_m and additive interference ζ_m . The additive interference is seen to be dependent on the number of sub-carriers N , the amplifier nonlinearity transfer characteristics and the symbol mapping. In a similar manner the behavior of a non-linear LNA, when used with single-carrier and multi-carrier transceivers, can be found.

The received signal after CP removal and channel equalization for SC scheme is given as

$$\hat{x}_m = x_m f(x_m) e^{jg(x_m)} + \mathcal{F}_m^{-1}(\mathbf{N}) \quad (3.45)$$

The multiplicative and additive terms in case of a single-carrier based system are given as

$$\kappa_m = f(x_m) e^{jg(x_m)}$$

and

$$\zeta_m = 0.$$

In single-carrier schemes there is no additive interference experienced by the baseband symbol but only multiplicative noise κ_m which is independent of the block length N . The multiplicative term is dependent only on the modulated symbol x_m and amplifier transfer characteristics.

The received multi-carrier signal is affected by a CMT and additive interference. This results in clustering of the signal constellation points in addition to constellation contraction and rotation, whereas in single-carrier, the only consequence is constellation rotation and contraction.

The simulation results for single-carrier and multi-carrier based systems using QPSK and 8PSK constellations and employing a nonlinear HPA are illustrated in Figure 3.9. Due to absence of ICI, the single-carrier scheme clearly outperforms the multi-carrier scheme in terms of SNR degradation. For instance the single-carrier QPSK scheme outperforms the multi-carrier QPSK by about 2 dB when the IBO is chosen to be 7 dB at a BER of 10^{-4} .

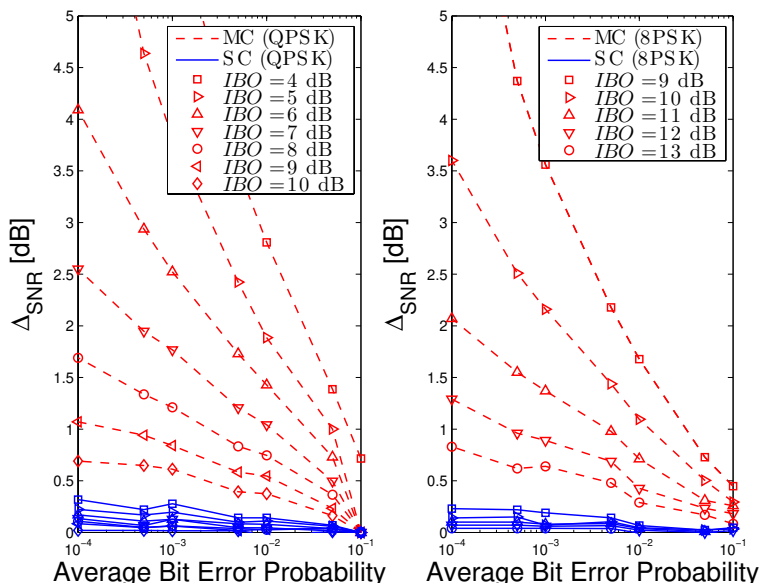


Figure 3.9: SNR degradation as a function of BER for various IBO values of the HPA.

3.9 System Design Summary

The SNR degradation (in dB), when all impairments are individually considered, for the single-carrier and multi-carrier schemes using QPSK and 8PSK constellations at a BER of 10^{-4} , for the system parameters outlined in Table 3.3, is given in Table 3.4. In Table 3.3, the ADC and DAC values are given in bits, the IBO values are specified in dB, phase noise is specified as the total integrated phase noise power K in dBc and I/Q imbalance as amplitude imbalance ϵ in dB and phase imbalance ϕ in degrees. It can be seen that an un-coded SC system, while having the same implementation complexity, undergoes a lower degradation in SNR for a given number of ADC and DAC bits and IBO for the HPA. It can tolerate a lower phase noise but higher amplitude and phase imbalance. The SC and MC schemes when used with 8PSK constellations, in the presence of I/Q imbalance exhibit an error floor much higher than 10^{-4} , and hence cannot be used without compensation.

Modulation	N_{DAC}	N_{ADC}	K_p	ϵ	ϕ	IBO_{HPA}
QPSK	4 bits	7 bits	-20 dBc	1 dB	4°	6 dB
8PSK	4 bits	9 bits	-24 dBc	1 dB	4°	10 dB

Table 3.3: Multi-carrier and single-carrier circuit parameters for quantitative comparison.

Mod.	Transc.	DAC	ADC	PN	I/Q	HPA
QPSK (BER= 1×10^{-4})	MC	1.2	2.8	0.9	2.6	4.1
	SC	0	0.2	1.1	1.8	0.3
8PSK (BER= 1×10^{-4})	MC	6.5	1.2	0.9	-	3.6
	SC	0.8	0.1	1.8	-	0.2

Table 3.4: Multi-carrier and single-carrier quantitative comparison.

3.10 Conclusions

In this chapter, a comparison of single-carrier and multi-carrier transmission schemes for 60 GHz wireless systems, in the presence of RF circuit imperfections, was presented. DAC, ADC, PN, I/Q and HPA models, that are in accordance with 60 GHz transceiver circuits, were used. For both modulation schemes, the

SNR degradation in terms of operating parameters such as the required number of bits in DAC/ADC and input back-off requirements for the HPA as a function of BER, was determined. The single-carrier schemes were shown to have a lower SNR degradation for a given set of ADC/DAC bits, HPA IBO values and I/Q imbalance parameters. Multi-carrier schemes on the other hand were shown to be more tolerant to phase noise. The single-carrier schemes on the whole offer a good trade-off in terms of circuit parameters and system performance, therefore, at the moment with immature 60 GHz circuit components, they are more suited for the implementation of low cost and power efficient wireless communication systems operating in the 60 GHz domain.

Chapter 4

Error Probability Analysis Under ADC Quantization Noise

In this chapter, closed-form expressions for the bit error probability of MPAM signal constellations as a function of the ADC word length, the SNR and the fading distribution, are derived. These results allow for a rapid and accurate evaluation of the system performance when the ADC resolution is limited, as is generally the case in high sampling rate communication systems, and thus provide a useful tool for system design, analysis and optimization.

4.1 Introduction

Direct conversion transceivers employing single-carrier (SC) schemes with directional antennas to counter ISI are a promising alternative to multi-carrier schemes, for high data rate communication systems operating in the 60 GHz and 100 GHz regime. I/Q imbalance as discussed in Chapter 3 is one of the major problems associated with direct conversion transceivers [83] which can be alleviated to an extent by employing one dimensional signal constellations [84]. It is well known that the power consumption in an ADC is directly proportional to $F_s \cdot 2^{N_{ADC}}$, where F_s denotes the sampling frequency and N_{ADC} represents the ADC word length. Thus with sampling rates in the range of Giga samples per second, N_{ADC} must be kept as small as possible. Monte Carlo simulations are often used to evaluate the system performance in terms of average bit error probability in the presence of limited ADC resolution. In [85] an analytical expression for the BER of OFDM based multi-carrier schemes is presented, which is based on the assumption that ADC quantization noise (QN) is Gaussian distributed. This assumption is valid only when the OFDM system employs a large number of sub-carriers and in general is not true for single-carrier schemes.

In this chapter, we derive closed-form expressions for the BER of Gray coded M -PAM signal constellations for single-carrier transmission in the presence of ADC QN over AWGN and fading channels. With the novel derived expressions, 2PAM (i.e, binary phase shift keying (BPSK)) and 4PAM are used as examples for the performance evaluation in various fading cases. For fading analysis the Nakagami- m distribution is assumed which covers line-of-sight as well as non-line-of-sight channels.

The rest of this chapter is organized as follows. In Section 4.2, the system model is introduced. The exact expression for the BER of MPAM schemes in AWGN channels is presented in Section 4.3. Section 4.4 provides an analysis of the bit error probability in fading scenarios. Conclusions are drawn in Section 4.6.

4.2 System Model

The real baseband equivalent received signal of an $MPAM$ communication system, after coherent detection, operating under the influence of fading h , AWGN n and

in the presence of ADC QN u is given as

$$y = hs + n + u = hs + z, \quad (4.1)$$

where s denotes the transmitted symbol chosen from the signal constellation set $\mathcal{S} = \{s_0, \dots, s_{M-1}\}$. The AWGN is assumed to be zero mean with variance σ_n^2 and power spectral density $N_0 = 2\sigma_n^2$. The additive QN u is uniformly distributed between $[-V/2^{N_{ADC}}, V/2^{N_{ADC}}]$ [34, p.186] and its variance is related with N_{ADC} as

$$\sigma_u^2 = \frac{V^2}{3 \cdot 2^{2N_{ADC}}}. \quad (4.2)$$

It is assumed that prior to ADC an automatic gain control circuit brings the signal within $[-V, V]$ and there is no clipping. In this chapter all signal constellations are taken to be Gray coded and equally distributed between $[-V, V]$ with an inter-symbol distance of

$$d = \frac{2V}{M-1}, \quad (4.3)$$

i.e., the l -th symbol in the signal constellation set is given as

$$s_l = \frac{V(2l - M + 1)}{M - 1}. \quad (4.4)$$

The average constellation energy is given as

$$E_s = \frac{1}{M} \sum_{l=0}^{M-1} s_l^2 = \frac{S_M V^2}{M(M-1)^2}, \quad (4.5)$$

where

$$S_M = \sum_{l=0}^{M-1} (2l - M + 1)^2. \quad (4.6)$$

Thus we get

$$V = \frac{\sqrt{M E_s}}{\sqrt{S_M}} (M - 1). \quad (4.7)$$

A system with frequency flat fading is assumed. The independent and identically distributed fading amplitudes h are drawn from a distribution with PDF $p_h(h)$. Assuming perfect channel state information at the receiver, symbol wise detection is performed, with the most likely transmitted symbol being chosen as the symbol

Distribution	PDF	Fourier
Uniform	$p_u(u) = \begin{cases} \frac{2^N}{2V}, & -\frac{V}{2^N} \leq u \leq \frac{V}{2^N}, \\ 0, & \text{otherwise} \end{cases}$	$\frac{e^{j\omega V 2^{-N}} - e^{-j\omega V 2^{-N}}}{2V j\omega 2^{-N}}$
Gaussian	$p_n(n) = \frac{e^{-\frac{n^2}{2\sigma_n^2}}}{\sqrt{2\pi\sigma_n^2}}$	$e^{-\frac{\sigma_n^2 \omega^2}{2}}$

Table 4.1: PDF and Fourier Transforms of Gaussian and Uniform distributions.

which minimizes the metric

$$\mathcal{C}(y, s_k) = |y - hs_k|^2 \text{ over all } s_k \in \mathcal{S}. \quad (4.8)$$

The Fourier transform (FT) of the PDF of a random variable a is defined as

$$\mathcal{F}_{p_a}(j\omega) = \int_{-\infty}^{\infty} p_a(a) e^{-j\omega a} da, \quad (4.9)$$

where $j^2 = -1$. Similarly, $p_a(a)$ can be obtained from $\mathcal{F}_{p_a}(j\omega)$ as

$$p_a(a) = \mathcal{F}^{-1}(\mathcal{F}_{p_a}(j\omega)) = \frac{1}{2\pi} \int_{-\infty}^{\infty} \mathcal{F}_{p_a}(j\omega) e^{j\omega a} d\omega, \quad (4.10)$$

where $\mathcal{F}^{-1}(\cdot)$ denotes the inverse FT. If a random variable u consists of the sum of two independent random variables a and b with PDFs $p_a(a)$ and $p_b(b)$, respectively, then the PDF of u is

$$p_u(u) = p_a(u) * p_b(u) = \mathcal{F}^{-1}(\mathcal{F}_{p_a}(j\omega) \mathcal{F}_{p_b}(j\omega)), \quad (4.11)$$

where $*$ denotes the convolution operation. The PDFs of Gaussian and uniform random variables used within this chapter along with their FTs are given in Table 4.1.

4.3 BER Analysis with AWGN

The average SNR per symbol for AWGN channels is defined as E_s/N_0 . The average energy per bit E_b is related with E_s as $E_s = \log_2(M) E_b$, and the average SNR per bit is given as E_b/N_0 . In the fading case, the instantaneous and average

SNRs are given as

$$\gamma = h^2 \frac{E_s}{N_0} \quad \text{and} \quad \bar{\gamma} = E [h^2] \frac{E_s}{N_0}, \quad (4.12)$$

respectively, where $E [.]$ denotes the expectation operation. Similarly, the average and instantaneous SNRs per bit for the fading case are denoted by

$$\gamma = h^2 \frac{E_b}{N_0} \quad \text{and} \quad \bar{\gamma}_b = E [h^2] \frac{E_b}{N_0}, \quad (4.13)$$

respectively. In this chapter $E [h^2] = 1$ is assumed. In [86], the BER for Gray coded MPAM signal constellations in the presence of AWGN is given, which can be generalized for any additive noise z as

$$P_b = 2K_M \sum_{k=1}^{\log_2(M)} \sum_{i=0}^{\mathcal{L}(k,M)} \mathcal{X}(k, i, M) \int_{\frac{\mathcal{Y}(i)d}{2}}^{\infty} p_z(z) dz, \quad (4.14)$$

where $p_z(z)$ represents the noise PDF and

$$K_M = \frac{1}{M \log_2(M)}. \quad (4.15)$$

The modulation and bit dependent functions $\mathcal{L}(k, M)$, $\mathcal{X}(k, i, M)$ and $\mathcal{Y}(i)$ are seen to follow a regular pattern for Gray coded MPAM signal constellations and are given as

$$\mathcal{L}(k, M) = (1 - 2^{-k}) M - 1, \quad (4.16)$$

$$\mathcal{X}(k, i, M) = (-1)^{\lfloor \frac{i \cdot 2^{k-1}}{M} \rfloor} \left(2^{k-1} - \left\lfloor \frac{i \cdot 2^{k-1}}{M} + \frac{1}{2} \right\rfloor \right) \quad (4.17)$$

and

$$\mathcal{Y}(i) = 2i + 1, \quad (4.18)$$

respectively [86].

In order to determine the BER, the PDF of $z = n + u$ must first be evaluated. Using the FTs given in Table 4.1 and (4.11) we can write the FT of the PDF of z as

$$\mathcal{F}_{p_z}(j\omega) = \left(\frac{e^{j\omega V 2^{-N_{ADC}}} - e^{-j\omega V 2^{-N_{ADC}}}}{j\omega V 2^{1-N_{ADC}}} \right) e^{-\frac{\sigma_n^2 \omega^2}{2}} \quad (4.19)$$

The PDF of z can be obtained by using (4.11) as

$$p_z(z) = \frac{1}{2\pi} \int_{-\infty}^{\infty} \frac{\left(e^{j\omega V 2^{-N_{ADC}}} - e^{-j\omega V 2^{-N_{ADC}}} \right) e^{-\frac{\sigma_n^2 \omega^2}{2}}}{j\omega V 2^{1-N_{ADC}}} e^{j\omega z} d\omega. \quad (4.20)$$

Solving the above integral yields the combined PDF [87, p.22], which can be stated as

$$p_z(z) = \frac{2^{N_{ADC}-2}}{V} \left[\operatorname{erf} \left(\frac{z + V 2^{-N_{ADC}}}{\sqrt{N_0}} \right) - \operatorname{erf} \left(\frac{z - V 2^{-N_{ADC}}}{\sqrt{N_0}} \right) \right], \quad (4.21)$$

where

$$\operatorname{erf}(x) = \frac{2}{\sqrt{\pi}} \int_0^x e^{-t^2} dt, \quad (4.22)$$

which is related to the Q function as

$$\operatorname{erf}(x) = 1 - 2Q(\sqrt{2}x). \quad (4.23)$$

Substituting (4.21) in (4.14) gives

$$P_b = K_M \sum_{k=1}^{\log_2(M)} \sum_{i=1}^{\mathcal{L}(k,M)} \mathcal{X}(k, i, M) \int_{d\mathcal{Y}(i)}^{\infty} \left[\operatorname{erf} \left(\frac{z + 2^{-N_{ADC}}}{\sqrt{N_0}} \right) - \operatorname{erf} \left(\frac{z - 2^{-N_{ADC}}}{\sqrt{N_0}} \right) \right] dz. \quad (4.24)$$

Solving the integral using [88] yields the expression of the BER for AWGN channels in the presence of ADC QN as

$$\begin{aligned} P_b = & K_M \sum_{k=1}^{\log_2(M)} \sum_{i=0}^{\mathcal{L}(k,M)} \mathcal{X}(k, i, M) Q \left(\sqrt{\frac{E_s}{N_0}} \varrho(\mathcal{Y}(i), 0) \right) \left(1 + \frac{\mathcal{Y}(i) 2^{N_{ADC}}}{M-1} \right) + \\ & K_M \sum_{k=1}^{\log_2(M)} \sum_{i=0}^{\mathcal{L}(k,M)} \mathcal{X}(k, i, M) Q \left(\sqrt{\frac{E_s}{N_0}} \varrho(\mathcal{Y}(i), 1) \right) \left(1 - \frac{\mathcal{Y}(i) 2^{N_{ADC}}}{M-1} \right) - \\ & \frac{B_M}{\sqrt{E_s/N_0}} \sum_{k=1}^{\log_2(M)} \sum_{i=0}^{\mathcal{L}(k,M)} \mathcal{X}(k, i, M) e^{-\frac{M E_s}{S_M N_0} (\mathcal{Y}(i) + (M-1) 2^{-N_{ADC}})^2} + \\ & \frac{B_M}{\sqrt{E_s/N_0}} \sum_{k=1}^{\log_2(M)} \sum_{i=0}^{\mathcal{L}(k,M)} \mathcal{X}(k, i, M) e^{-\frac{M E_s}{S_M N_0} (\mathcal{Y}(i) - (M-1) 2^{-N_{ADC}})^2}, \quad (4.25) \end{aligned}$$

where

$$\varrho(\mathcal{Y}(i), l) = \sqrt{M} \left(\frac{2\mathcal{Y}(i) + (-1)^l (M-1) 2^{-N_{ADC}+1}}{\sqrt{2S_M}} \right), \quad (4.26)$$

and

$$B_M = \frac{K_M \sqrt{S_M}}{(M-1) \sqrt{M} \pi 2^{-N_{ADC}+1}}. \quad (4.27)$$

As an illustrative example, the BER of 2PAM (BPSK) and substituting $M = 2$ in (4.25), can be written in closed form as

$$\begin{aligned} P_b = & \frac{1}{2} Q \left(\sqrt{\frac{2E_b}{N_0}} (1 + 2^{-N_{ADC}}) \right) + 2^{N-1} Q \left(\sqrt{\frac{2E_b}{N_0}} (1 + 2^{-N_{ADC}}) \right) + \\ & \frac{1}{2} Q \left(\sqrt{\frac{2E_b}{N_0}} (1 - 2^{-N_{ADC}}) \right) - 2^{N_{ADC}-1} Q \left(\sqrt{\frac{2E_b}{N_0}} (1 - 2^{-N_{ADC}}) \right) - \\ & \frac{2^{N_{ADC}-2}}{\sqrt{\pi E_b/N_0}} \left(e^{-\frac{E_b}{N_0} (1+2^{-N_{ADC}})^2} - e^{-\frac{E_b}{N_0} (1-2^{-N_{ADC}})^2} \right). \end{aligned} \quad (4.28)$$

For the case when there is no additive quantization noise, i.e., $N_{ADC} \rightarrow \infty$, (4.28) reduces to $\lim_{N_{ADC} \rightarrow \infty} P_b = Q \left(\sqrt{2E_b/N_0} \right)$, which is the exact expression for the error probability of BPSK in AWGN channels.

4.4 BER Analysis in Fading Conditions

For the case of fading channels and coherent detection the signal constellation is scaled by the channel gain h . This implies that for a given fading realization h , the Euclidean inter-symbol distance is given as hd . Therefore, the BER evaluation requires the computation of an average over the fading distribution as

$$P_b^F = \int_0^\infty P_b(h) p_h(h) dh, \quad (4.29)$$

where $P_b(h)$ denotes the instantaneous BER for a given fading realization h and is given as

$$P_b(h) = 2K_M \sum_{k=1}^{\log_2(M)} \sum_{i=0}^{\mathcal{L}(k,M)} \mathcal{X}(k, i, M) \int_{\frac{\mathcal{Y}(i)hd}{2}}^\infty q_z(z) dz. \quad (4.30)$$

Following the derivation in the last section it can be easily shown that $P_b(h)$ can be written as

$$\begin{aligned}
P_b = & K_M \sum_{k=1}^{\log_2(M)} \sum_{i=0}^{\mathcal{L}(k,M)} \mathcal{X}(k, i, M) Q\left(\sqrt{\bar{\gamma}}\vartheta(\mathcal{Y}(i), 0)\right) \left(1 + \frac{h\mathcal{Y}(i)2^{N_{ADC}}}{M-1}\right) + \\
& K_M \sum_{k=1}^{\log_2(M)} \sum_{i=0}^{\mathcal{L}(k,M)} \mathcal{X}(k, i, M) Q\left(\sqrt{\bar{\gamma}}\vartheta(\mathcal{Y}(i), 1)\right) \left(1 - \frac{h\mathcal{Y}(i)2^{N_{ADC}}}{M-1}\right) - \\
& \frac{B_M}{\sqrt{\bar{\gamma}}} \sum_{k=1}^{\log_2(M)} \sum_{i=0}^{\mathcal{L}(k,M)} \mathcal{X}(k, i, M) e^{-\frac{M}{S_M}\bar{\gamma}(h\mathcal{Y}(i)+(M-1)2^{-N_{ADC}})^2} + \\
& \frac{B_M}{\sqrt{\bar{\gamma}}} \sum_{k=1}^{\log_2(M)} \sum_{i=0}^{\mathcal{L}(k,M)} \mathcal{X}(k, i, M) e^{-\frac{M}{S_M}\bar{\gamma}(h\mathcal{Y}(i)-(M-1)2^{-N_{ADC}})^2}, \tag{4.31}
\end{aligned}$$

where

$$\vartheta(\mathcal{Y}(i), l) = \sqrt{M} \left(\frac{2h\mathcal{Y}(i) + (-1)^l(M-1)2^{-N_{ADC}+1}}{\sqrt{2S_M}} \right). \tag{4.32}$$

By substituting $h = (1 + \nu) / (1 - \nu)$ in (4.29), multiplying with $\sqrt{1 - \nu^2} / \sqrt{1 - \nu^2}$ and using the Gauss-Chebyshev quadrature (GCQ) [89, p.889, 25.4.38], the BER over fading channels in the presence of AWGN and ADC QN can be approximated as

$$P_b^F \approx \frac{2\pi}{N_g} \sum_{l=1}^{N_g} P_b \left(\frac{1 + \nu_l}{1 - \nu_l} \right) p \left(\frac{1 + \nu_l}{1 - \nu_l} \right) \frac{\sqrt{1 - \nu_l^2}}{(1 - \nu_l)^2}, \tag{4.33}$$

where

$$\nu_l = \cos \left(\frac{\pi}{2N_g} (2l - 1) \right) \tag{4.34}$$

and N_g denotes the degree of the Gauss-Chebyshev polynomial. The larger the value of N_g the closer is the approximation to the actual value. The expression given in (4.33) is in general true for any fading distribution but we restrict our discussion to the Nakagami- m distribution.

4.5 Numerical Results

In this section we verify the analysis with Monte Carlo simulations and then use the analytical results to investigate the impact of the fading parameter m and the modulation level M on the BER performance. The analytical curves for AWGN and fading channels are generated using (4.25) and (4.33), respectively. For the analysis of fading channels, the Gauss-Chebyshev polynomial degree $N_g = 16$ was seen sufficient for excellent accuracy. For $N_g < 16$, the approximate solution may not converge and the approximated value deviates from the actual value.

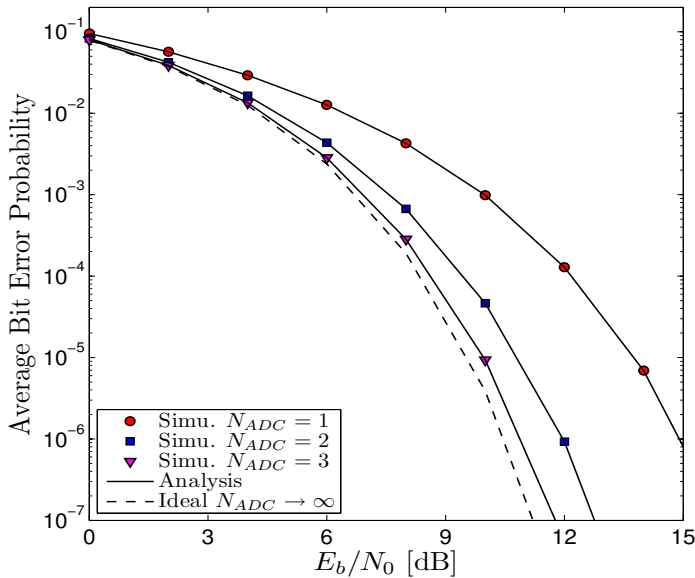


Figure 4.1: BER of 2PAM over an AWGN channel for various N_{ADC} values.

4.5.1 Error Probability

The BER for 2PAM and 4PAM signal constellations over AWGN channels is depicted in Figures 4.1 and 4.2, respectively. The simulations and analysis are seen to be in good agreement. It can be seen from the figure that a remarkable improvement in the system performance is achieved as the number of bits in the ADC are increased from 1 to 2. Increasing the number of ADC bits beyond 2 results in diminishing performance gains. For example, if 2PAM is employed the system performance improves by about 4 dB at a BER of 10^{-4} as N_{ADC} is

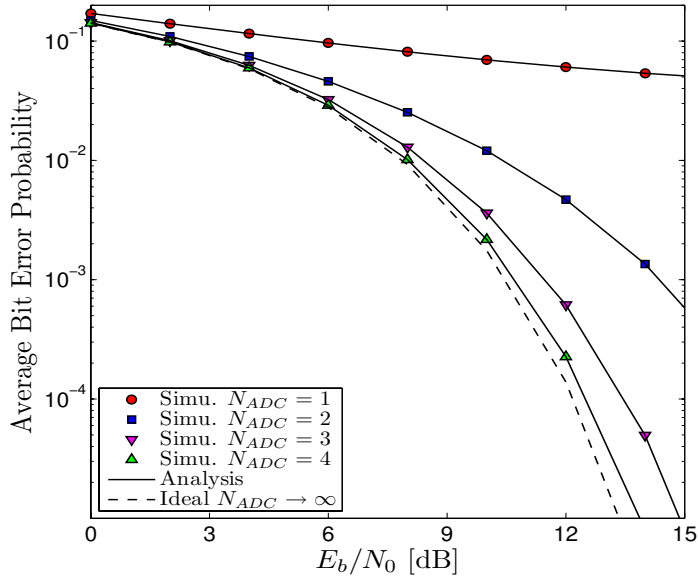


Figure 4.2: BER of 4PAM over an AWGN channel for various N_{ADC} values.

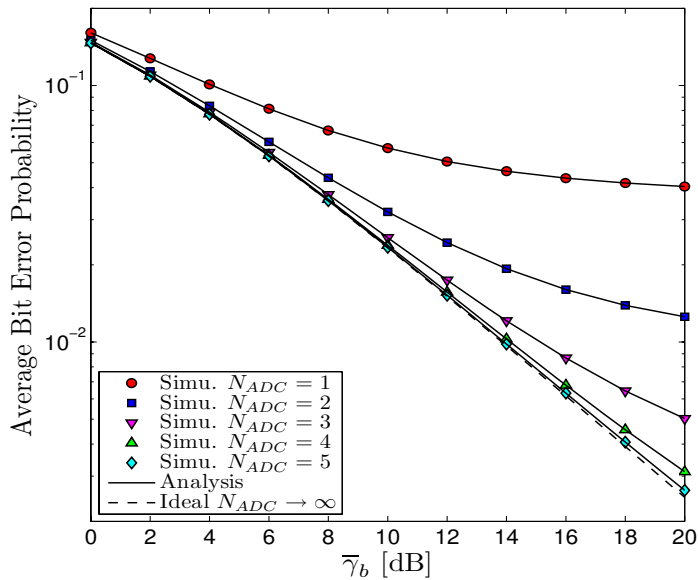


Figure 4.3: BER of 2PAM over a Rayleigh fading channel for various N_{ADC} values.

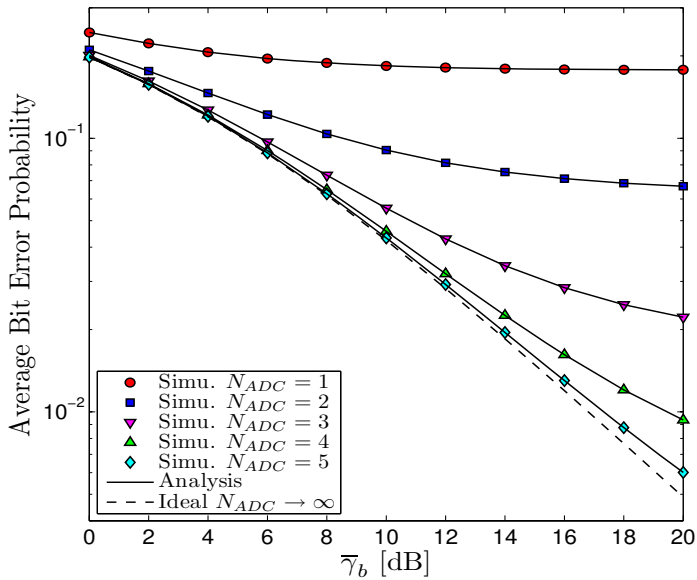


Figure 4.4: BER of 4PAM over a Rayleigh fading channel for various N_{ADC} values.

increased from 1 to 2, whereas, this gain is only about 1 dB when the N_{ADC} is increased from 2 to 3.

The BER over Rayleigh fading channels for 2PAM and 4PAM signal sets is shown in Figures 4.3 and 4.4, respectively. Here again the simulation and analysis is seen to be in good agreement. The increase in performance by increasing the number of ADC bits from 1 to 2 is again far greater than from 2 to 3. Furthermore, as compared to the AWGN case the fading scenarios exhibits more performance degradation, especially for lower values of N_{ADC} . For example, when 2PAM is used the performance is degraded by about 12 dB (at a BER of 4×10^{-2}) in fading scenario, which is much more in comparison to the AWGN channel (2 dB). This is primarily attributed to the fact that in fading scenarios the instantaneous received SNR can be quite low at times. Therefore, the received signal instead of being in the middle of the quantization region is pushed closer to the decision boundary between two signal constellation points and will require only a small amount of noise to cross the boundary and give detection errors.

4.5.2 Impact of channel parameter m

As another interesting application of the obtained results, the impact of changing the ADC resolution of 2PAM on the BER for different m parameters at $E_b/N_0 = 10$ dB is depicted in Figure 4.5. This can help the system designer to quickly establish the degradation in system performance due to limited ADC resolution for a given channel type (m parameter). For example, a maximum BER of 10^{-3} at $E_b/N_0 = 10$ dB can be achieved with a 2 bit ADC at $m = 7$, while for a channel with $m = 5$ a 3 bit ADC would be required.

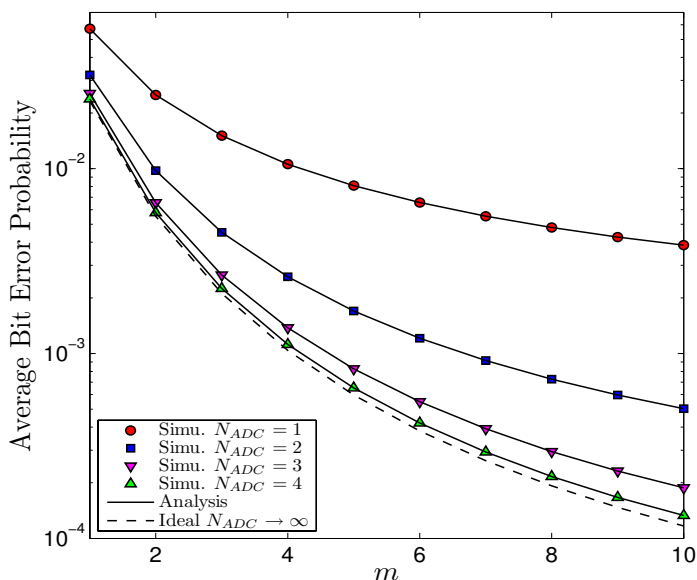


Figure 4.5: BER of 2PAM over various Nakagami- m fading channels with different N_{ADC} values at $\bar{\gamma}_b = 10$ dB.

4.5.3 Impact of the modulation level M

The impact of N_{ADC} on the modulation level M for AWGN and Rayleigh fading channels is shown in Figures 4.6 and 4.7, respectively. The figures give the error probability ratio Δ against the modulation index M . The error probability ratio is defined as the ratio of BER under ideal conditions, without QN to the BER with ADC QN, i.e.,

$$\Delta = \frac{\text{BER with ADC}}{\text{Ideal BER}}. \quad (4.35)$$

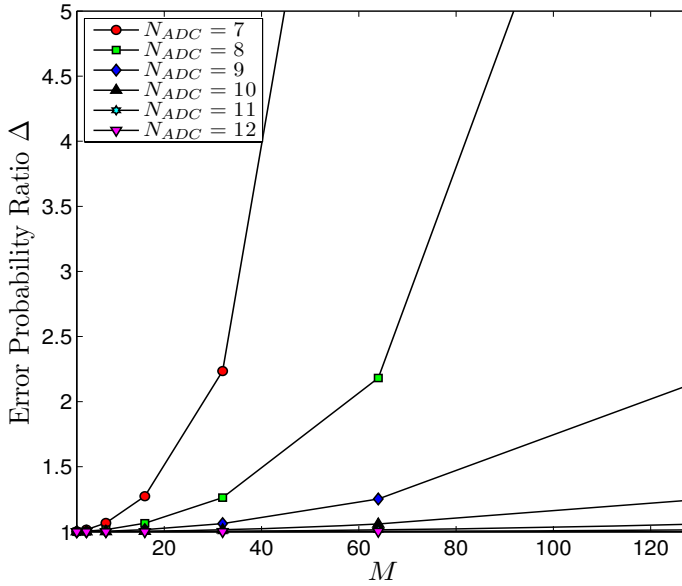


Figure 4.6: Degradation in BER as a function of M for various values of N_{ADC} over an AWGN channel at a BER of 10^{-5} .

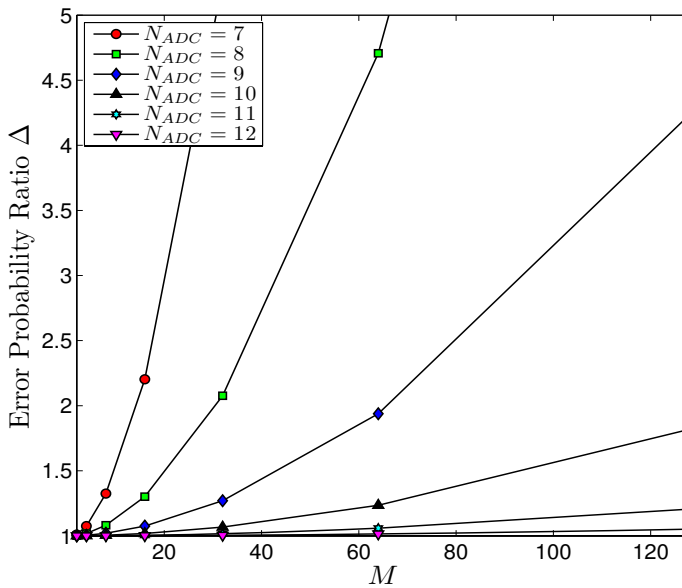


Figure 4.7: Degradation in BER as a function of M for various values of N_{ADC} over a Rayleigh fading channel at a BER of 10^{-3} .

It can be seen that the ADC word length required to achieve this ratio close to 1 (ideal case) depend on the modulation level. Lower modulation levels such as BPSK require less bits whereas higher levels such as 16 PAM require more bits. This means that using a lot of bits in the ADC is useless if the system does not employ higher level modulations.

4.6 Conclusions

In this chapter, the BER of MPAM modulation schemes in the presence of ADC QN was analyzed for fading and non-fading scenarios. Closed form expressions for the BER of Gray coded MPAM signals in the presence of AWGN, Nakagami fading and ADC QN, were presented. These expressions were then used to investigate the system performance. This analysis enables the system designer to rapidly determine for example the minimum number of bits required to achieve a desired performance for a given modulation level and under particular fading conditions.

Chapter 5

RF Level Diversity Combining

Radio frequency level diversity combining is a low cost and power efficient alternative to conventional diversity combining as it requires fewer analog-to-digital converters and down converters (mixers). In this chapter we investigate the possibility of utilizing the radio frequency level diversity combining architecture with low complexity sub-optimal diversity combining schemes such as equal gain combining, selection combining and switched combining. Novel analytical expressions to evaluate the performance of each of the mentioned schemes in Rayleigh fading scenarios for single-carrier binary and multi-level phase shift keying signals are derived. These expressions are then utilized to make system level trade-offs and to compare the performance with non-coherent and differentially coherent schemes under diversity reception.

5.1 Introduction

The deleterious effects of fading in wireless communications can be effectively mitigated with diversity combining (DC) [14]. The roots of diversity combining can be traced back to late 1950s when Brennan in his classic work first proposed the idea [13]. Since then, a lot of work has been carried out in this area and many different flavors of diversity combining have been introduced. This has resulted in the adoption of various diversity combining schemes for many current and emerging wireless communication systems. Diversity combining, in which, two or more replicas of the same signal are cleverly combined, offers great benefits for increasing the instantaneous received signal-to-noise ratio (SNR).

In traditional or conventional diversity combiners, in which digital baseband processing is utilized, channel phase compensation can be carried out with high finite precision. This is primarily due to the availability of large word lengths in modern digital signal processors. Large word length implies that any digital signal can closely match its analog counterpart and therefore carries very low (or negligible) quantization noise, as was explained in Chapter 4. This however, is not applicable for radio frequency (RF) level diversity combining, in which, it is cumbersome to accomplish channel phase compensation with infinite (or high finite) precision. Two major reasons for this are (1) continuous phase shifters are difficult to manufacture and (2) they significantly increase the system cost and complexity, especially at very high carrier frequencies such as 60 GHz [90]. One alternative is to carry out phase compensation in small discrete steps which reduces the system cost and complexity at the expense of adding more quantization noise in the system. Thus, from a hardware complexity and cost perspective, the number of steps in the phase shifters should be kept as small as possible. On the other hand, a larger step size implies a higher degradation in the system performance. In this chapter, using average error probability as a system performance indicator, we develop mathematical tools to investigate this performance. But first, a brief review of various diversity combining schemes is presented and the differences of conventional and RF level diversity combining are highlighted.

5.1.1 Diversity combining

As mentioned before, in diversity combining the same information bearing signal is received over differently fading branches. Since the probability that all the

branches are simultaneous in deep fade is quite low in all the diversity branches, the diversity combining, yields a superior performance as compared to single link channels. Diversity can be realized:

- in time by sending the same signal over various time slots
- in frequency by sending the same signal over multiple frequencies
- in space by employing multiple receive antennas.

There are four basic types of diversity combining techniques. Their main classification is based on (1) complexity and (2) the amount of channel state information (CSI) available at the receiver.

Maximum Ratio Combining

In interference free scenarios, maximum ratio combining (MRC) is the optimum diversity combining scheme [14]. It offers the best performance at the cost of high system complexity. In MRC the received signal on each diversity branch after co-phasing is multiplied with the fading amplitude of the diversity branch. The weighted and phase compensated signals from different diversity branches are then added together and passed on to the signal detector. Since the knowledge of both channel phase and amplitude is required for each diversity branch, MRC is best suited for unequal energy signal constellations such as quadrature amplitude modulation (QAM). This however, makes the system complex and not particularly suited for low complexity transceiver implementation, which is a basic requirement for 60 GHz systems. Therefore, MRC will not be pursued further in this chapter.

Equal Gain Combining

In equal gain combining (EGC) the received signal on each diversity branch is co-phased and added together, before being passed to the detector. This yields a sub-optimal but low complexity solution relative to MRC, since it does not require the estimation and compensation of channel amplitudes. This type of combining scheme is best suited for equal energy signal sets such as phase shift keying (PSK).

Selection Combining

Unlike MRC and EGC, which require all or some of the CSI from all the diversity branches, selection combining (SC) as its name suggests processes only a single diversity branch. This means that all diversity branches or chains need not be

active all the time. This improves system power consumption and further lowers the system complexity. In SC only the diversity branch with the highest received instantaneous signal power (or SNR) is selected.

Switched Combining

Switched combining (SWC) was proposed as an attempt to further lower the computational complexity of the system. As mentioned before, SC picks the diversity branch with the highest received signal strength, which requires the continual monitoring for all diversity branches. In order to prevent this, the SWC scheme rather than continuously picking the best diversity branch, stays connected to a particular branch as long as the signal strength on that branch does not drop below some predefined threshold. And when the signal drops below the specified threshold the receiver switches to the another diversity branch. Three popular variants of SWC namely switch and stay combining (SSC), switch and examine combining (SEC) and switch and examine combining with post selection (SECps) will be explored further in this chapter.

Due to their low complexity EGC, SC and SWC schemes are good candidates for 60 GHz system design. They will be investigate and explained further in this chapter.

5.1.2 Conventional vs. RF Level Diversity Combining

DC when implemented with multiple receive antennas has the disadvantage of requiring two mixers (down-converters) and two ADCs per antenna element. This makes the system design inefficient in terms of cost and power consumption and is difficult to realize, especially in portable terminals or at high carrier frequencies such as 60 GHz. Recently, RF level diversity combining [90, 91] has been proposed as an attractive alternative to overcome the drawbacks associated with conventional systems. In RF level DC proposed in [91], the channel phase and amplitude tracking is moved from the baseband part to the RF level. The channel phase compensation is also performed at RF level by making use of circuit elements such as phase shifters. This significantly reduces the system hardware and baseband processing requirements, thus paving the way for low cost and low complexity devices. The reduction in system cost and complexity, however, entails a deterioration in system performance. In this chapter, we develop mathematical tools to investigate the tradeoff between performance and the number of steps in the phase shifter L . By mathematical tools analytical expressions for average

bit and symbol error rate are implied which can quickly and accurately evaluate the system performance as a function of L , average received SNR and number of diversity branches N_R . An additional advantage for such analysis is that one can in principal also investigate the trade-off between L and N_R for a given error probability and SNR. This implies, that while maintaining the same system performance we can choose to either put more phase steps L or diversity branches N_R (antennas) whichever is more suitable from a cost/complexity perspective.

In non-coherent and differently coherent schemes diversity combining can be carried out without channel phase information. Thus a natural argument would be: why use RF level diversity combining when we can also perform non-coherent combining? The error probability expressions that we develop in this chapter can also be used to answer this question and to compare the performance with non-coherent and differentially coherent schemes. In particular, it is useful to determine in which scenarios the RF level diversity combining outperforms the non-coherent schemes (if at all). Thus a system with limited phase shifter resolution and/or diversity branches (antennas) may not be a viable alternative for implementing 60 GHz transceivers.

The chapter organization is as follows. Section 5.2 presents the system model and notations. The performance analysis for EGC and SC is presented in Sections 5.3 and 5.4, respectively. The performance of SWC is outlined in Section 5.5. A comparison of the three combining schemes is given in Section 5.6. Conclusions are drawn in Section 5.7.

5.2 System Model

The model for a communication system employing RF level diversity combining is depicted in Figure 5.1, which has obvious advantages in terms of cost and power consumption compared to the conventional antenna diversity combiner as shown in Figure 5.2. It is assumed that channel estimation and compensation along with signal combining is carried out at the RF level. Since channel co-phasing is implemented by hardware phase shifters it is difficult to accomplish this with infinite precision. Instead, it is carried out in discrete steps, which is equivalent to phase quantization.

The complex baseband signal after RF level diversity combining at time instant

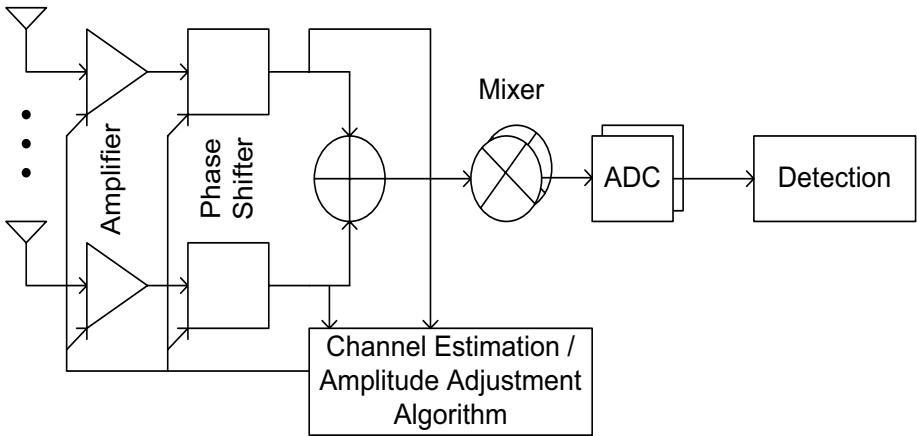


Figure 5.1: System architecture for an RF level diversity combiner.

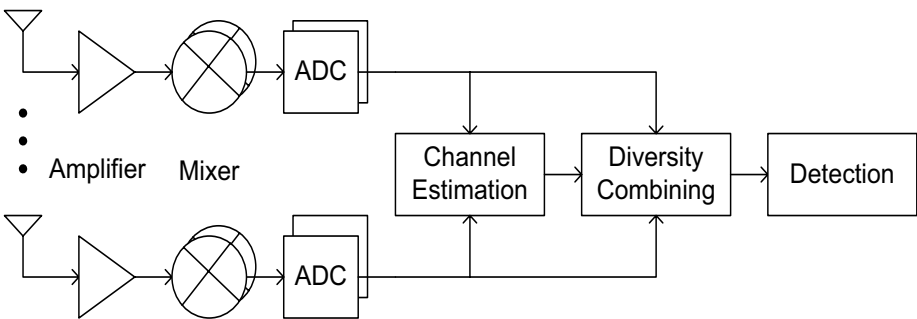


Figure 5.2: System architecture for a conventional diversity combiner.

t is given as

$$\begin{aligned} r(t) &= \sum_{i=0}^{N_R-1} \left(h_i(t) e^{j\theta_i(t)} s(t) + n_i(t) \right) g_i(t) e^{-j\theta_i^{\mathcal{Q}}(t)} \\ &= \sum_{i=0}^{N_R-1} h_i(t) g_i(t) e^{j(\theta_i(t) - \theta_i^{\mathcal{Q}}(t))} s(t) + g_i(t) \hat{n}_i(t), \end{aligned} \quad (5.1)$$

where $n_i(t)$ and $\hat{n}_i(t)$ represent zero mean complex additive white Gaussian noise (AWGN) with variance $N_0/2$ per dimension, N_R is the number of antennas at the receiver and $g_i(t)$ denotes the amplifier gain. The channel gains $h_i(t)$ are assumed to be Rayleigh distributed with uniformly distributed channel phase $\theta_i(t)$ between $[-\pi, \pi)$. It is assumed that the antenna elements are sufficiently separated for each branch to undergo independent but identically distributed (i.i.d) fading. The quantized channel phase is denoted by $\theta_i^{\mathcal{Q}}(t)$ and $s(t)$ represents the complex baseband modulated symbol chosen from the M -dimensional PSK signal constellation set ¹

$$\mathcal{S} \in \left\{ s_l = \sqrt{E_s} e^{j2\pi l/M} \right\}_{l=0}^{M-1}, \quad (5.2)$$

where E_s denotes the symbol energy. For an L -level uniform phase quantizer the phase can be modeled as

$$\theta_i^{\mathcal{Q}}(t) = \theta_i(t) + \theta_i^{\mathcal{E}}(t), \quad (5.3)$$

where $\theta_i^{\mathcal{E}}(t)$ is uniformly distributed between $(-\pi/L, \pi/L)$. The amplifier gains for different diversity combining schemes are given as:

- *EGC*: All amplifier gains are set to unity, since only channel co-phasing is performed.
- *SC*: The amplifier gain of the branch with the maximum instantaneous received signal strength is set to unity while all others are set to 0.
- *SWC*: The main idea behind switched combining is to stay connected with a diversity branch until the received signal strength drops below a certain specified threshold. This switching action can be accomplished in a variety

¹This signal constellation set is different from \mathcal{S} introduced in Chapter 4.

of ways. For SSC, the first branch with the received signal strength greater than the threshold value is selected and the amplifier gain of that branch is set to unity while the gains for all other branches is set to 0. In the next time slot if the signal strength drops below the threshold then the amplifier gain for the next available branch will be set to 1, i.e., the next available branch will be selected while the amplifier gains for all other branches will be 0. This switching takes place irrespective of the signal level on the next (selected) diversity branch. Similar to the SSC case, in SEC the first branch with higher signal strength than the threshold is selected, however, unlike the SSC case in the next time slot if the signal strength drops below the threshold value then instead of switching to the next branch irrespective of its signal strength, a comparison is made with the threshold value for the next branch. This process is repeated until a diversity branch with received signal strength higher than the threshold is found or all diversity branches have been examined. In case the signal strength in all diversity branches is lower than the threshold value then the last examined branch is selected, i.e., the amplifier gain for the last examined branch is set to unity while amplifier gains for all other branches are set to 0. The SECps works in the same manner as the SEC combining except, if the received signal strength in all the diversity branches is lower than the threshold then the diversity branch with the maximum received signal strength is selected.

The amplifier gains $g_i(t)$ for EGC, SC, SSC, SEC and SECps, using [53,54], are summarized in Table 5.1, in which, r_T denotes the switching threshold and

$$h^M(t) = \max \{h_0(t), \dots, h_{N_R-1}(t)\}, \quad (5.4)$$

where $((i-1)_{N_R})$ denotes the $i-1$ modulo N_R . It has been shown in [53] that increasing the number of branches for SSC beyond two does not improve the system performance. Therefore, in this thesis only dual branch SSC is considered.

5.3 RF Level Equal Gain Combining

For conventional EGC, as mentioned before, the channel phases are estimated and compensated for in the digital baseband. The combining in the digital domain entails very low quantization noise and therefore it is generally not included

Table 5.1: Amplifier gains for EGC, SC, SSC, SEC and SECps.

Scheme	$g_i(t)$
EGC	$g_i(t) = 1, \forall i$
SC	$g_i(t) = \begin{cases} 1, & \text{iff } h_i(t) = h^M(t), \\ 0, & \text{otherwise} \end{cases}$
SSC	$g_i(t) = \begin{cases} 1, & \text{iff } \begin{cases} g_i(t-1) = 1 \text{ and } h_i(t) \geq r_T, \text{ or} \\ g_{((i-1))_{N_R}}(t-1) = 1 \text{ and} \\ h_{((i-1))_{N_R}}(t) < r_T \end{cases} \\ 0, & \text{otherwise} \end{cases}$
SEC	$g_i(t) = \begin{cases} 1, & \text{iff } \begin{cases} g_i(t-1) = 1 \text{ and } h_i(t) \geq r_T, \text{ or} \\ g_i(t-1) = 1 \text{ and } h_k(t) < r_T, \\ k = 0, \dots, N_R - 1, \text{ or} \\ g_{((i-1))_{N_R}}(t-1) = 1 \text{ and} \\ h_{((i-1))_{N_R}}(t) < r_T \text{ and} \\ h_i(t) \leq r_T, \text{ or} \\ g_{((i-j))_{N_R}}(t-1) = 1 \text{ and} \\ h_{((i-j+k))_{N_R}}(t) < r_T \text{ and} \\ h_i(t) \geq r_T, k = 0, \dots, j-1, \text{ or} \\ g_{((i-1))_{N_R}}(t-1) = 1 \text{ and} \\ h_{((i-1+k))_{N_R}}(t) < r_T \text{ and} \\ h_i(t) \geq r_T, k = 0, \dots, N_R - 2 \end{cases} \\ 0, & \text{otherwise} \end{cases}$
SECps	$g_i(t) = \begin{cases} 1, & \text{iff } \begin{cases} g_i(t-1) = 1 \text{ and } h_i(t) \geq r_T, \text{ or} \\ h_k(t) < r_T \text{ and } h_i(t) = h^M(t), \\ k = 0, \dots, N_R - 1 \end{cases} \\ 0, & \text{otherwise} \end{cases}$

in the performance analysis of traditional (or conventional) EGC. A number of investigations regarding the performance of EGC in various fading scenarios has been carried out in the literature. In [39], the PDF for the sum of Rayleigh random variables is represented in the form of a series and used for error rate evaluation of EGC. A decision variable based approach is taken in [40] to evaluate the performance of the EGC and simplify the analysis presented in [39]. In [41] the characteristic function (CHF) based approach is applied to alleviate the need for computing the PDF of the combined signal amplitude with EGC. A similar but slightly different approach is adopted in [42], the difference being in the calculation of the conditional error probability (CEP). Closed form error probability expressions for the case of dual branch EGC over Rayleigh fading

channels were presented in [43]. In [44], the impact of Gaussian weighting errors on the performance of EGC with BPSK modulation over Rayleigh fading channels is analyzed. All these performance investigations for EGC carried out thus far assume that the channel phase can be perfectly compensated for in the digital baseband. The main conclusions that can be inferred from this work is that it possible to represent the bit (or symbol) error probability in closed form or as a single finite integral of elementary functions. The error probability expressions give the bit (or symbol) error probability as a function of SNR and the number of diversity branches. These can then be used to estimate the performance under various fading conditions. In this section we will investigate the impact of imperfect channel co-phasing on EGC combiners.

The complex baseband signal after RF level EGC with discrete phase compensation using (5.1) and (5.3) after ignoring the time index for notational convenience, is given as

$$r = \sum_{i=0}^{N_R-1} (h_i e^{j\theta_i} s + n_i) e^{-j\theta_i^Q} = \sum_{i=0}^{N_R-1} h_i e^{j(\theta_i - \theta_i^Q)} s + \tilde{n}_i = \sum_{i=0}^{N_R-1} h_i e^{-j\theta_i^E} s + \tilde{n}_i, \quad (5.5)$$

where n_i and \tilde{n}_i represent zero mean complex AWGN with variance $N_0/2$ per dimension. Over here we only limit ourselves to BPSK signalling, therefore, the baseband modulated symbol is chosen from the signal constellation set $\{-1, +1\}$. Since in case of EGC only BPSK signalling is considered, only the real part of the signal has an impact on the detection performance. The real or in-phase part of (5.5) can be written as

$$r_I = \sum_{i=0}^{N_R-1} h_i \cos(\theta_i^E) s + \Re[\tilde{n}_i] = \sum_{i=0}^{N_R-1} h_i z_i s + \Re[\tilde{n}_i], \quad (5.6)$$

where $z_i = \cos(\theta_i^E)$. The instantaneous SNR for EGC is defined as $\gamma = x^2$ where

$$x = \sqrt{\frac{E_s}{N_R N_0}} \sum_{i=0}^{N_R-1} h_i z_i = \sqrt{\frac{E_s}{N_R N_0}} \sum_{i=0}^{N_R-1} y_i = \sqrt{\frac{1}{N_R}} \sum_{i=0}^{N_R-1} v_i = \frac{w}{\sqrt{N_R}}, \quad (5.7)$$

where ²

$$v_i = y_i \sqrt{\frac{E_s}{N_0}}, \quad (5.8)$$

$$y_i = h_i z_i \quad (5.9)$$

and

$$w = \sum_{i=0}^{N_R-1} v_i. \quad (5.10)$$

5.3.1 Error Probability Analysis

The error probability for EGC is given as

$$P_s = \int_0^\infty P(\varepsilon | x) p_x(x) dx, \quad (5.11)$$

where $P(\varepsilon | x)$ and $p_x(x)$ represent the CEP and the PDF of x , respectively. To alleviate the need for $p_x(x)$ computation, which is generally cumbersome, we can write the BER using the CHF based approach as [41]

$$P_s = \frac{1}{2\pi} \int_{-\infty}^\infty \mathcal{G}(\omega) \phi_x^*(\omega) d\omega, \quad (5.12)$$

where $\phi_x^*(\omega)$ denotes the complex conjugate of the CHF of x and

$$\mathcal{G}(\omega) = \int_{-\infty}^\infty P(\varepsilon | x) e^{j\omega x} dx \quad (5.13)$$

denotes the Fourier transform (FT) of the CEP. The FT of the CEP for BPSK signalling is given as [41]

$$\mathcal{G}(\omega) = \frac{1}{2\omega} \left(\frac{\omega}{\sqrt{\pi}} {}_1F_1 \left(1; \frac{3}{2}; -\frac{\omega^2}{4} \right) + j - j e^{-\frac{\omega^2}{4}} \right), \quad (5.14)$$

where ${}_1F_1(\cdot; \cdot; \cdot)$ represents the confluent hypergeometric function of the first kind [92, p. 260, Eq. (9.9.1)]. After some manipulation (5.12) can be written as [41]

$$P_s = \frac{2}{\pi} \int_0^{\pi/2} \frac{\Re[\tan(\eta) \mathcal{G}(\tan(\eta)) \phi_x^*(\tan(\eta))]}{\sin(2\eta)} d\eta. \quad (5.15)$$

²The variables x and y are redefined in the scope of this chapter and have no relation with those defined in Chapter 3.

The CHF of x is given by

$$\phi_x(\omega) = \prod_{i=0}^{N_R-1} \phi_{y_i} \left(\omega \sqrt{\frac{E_s}{N_R N_0}} \right) = \prod_{i=0}^{N_R-1} \phi_{v_i} \left(\frac{\omega}{\sqrt{N_R}} \right). \quad (5.16)$$

The average SNR per branch is denoted by

$$\bar{\gamma}_i = E[v_i^2] = \frac{E_s}{N_0} E[y_i^2] = \bar{\gamma}, \quad (5.17)$$

where $E[\cdot]$ denotes the expectation operation. The last equality follows from the fact that the branches have identical average SNR because of the i.i.d fading. Thus, to evaluate the error probability we need to determine the CHF of y_i , which is a product of two random variables, i.e., h_i and z_i . Since $\theta_i^{\mathcal{E}}$ is uniformly distributed between $(-\pi/L, \pi/L)$, the PDF of $z_i = \cos(\theta_i^{\mathcal{E}})$ is given as

$$p_{z_i}(z) = \frac{L}{\pi\sqrt{1-z^2}}, \quad \cos(\pi/L) \leq z \leq 1. \quad (5.18)$$

5.3.2 PDF and CHF

Using [93, Eq. (4)], the PDF of $y_i = h_i z_i$ can be written as

$$p_{y_i}(y) = \int_0^\infty \frac{d}{dy} \left[F_{h_i} \left(\frac{y}{z} \right) \right] p_{z_i}(z) dz, \quad (5.19)$$

where $F_{h_i}(h)$ denotes the cumulative distribution function (CDF) of h_i . The CDF for the Rayleigh fading case is given as

$$F_{h_i}(h) = 1 - e^{-\frac{h^2}{\Omega_i}}, \quad (5.20)$$

where $\Omega_i = E[h_i^2]$. Substituting (5.20) and (5.18) in (5.19), we obtain

$$p_{y_i}(y) = \frac{2L}{\pi\Omega_i} \int_{L_c}^1 \frac{y e^{-\frac{y^2}{\Omega_i z^2}}}{z^2 \sqrt{1-z^2}} dz, \quad (5.21)$$

where $L_c = \cos(\pi/L)$. The solution to (5.21) can be obtained by using the result given in the Appendix A. Substituting $z = \sin(\theta)$ in (5.21) and using (A.4) yields

$$p_{y_i}(y) = \frac{L}{\sqrt{\pi\Omega_i}} e^{-\frac{y^2}{\Omega_i}} \operatorname{erf}\left(\frac{y}{\sqrt{\Omega_i}} \tan\left(\frac{\pi}{L}\right)\right), \quad (5.22)$$

where $\operatorname{erf}(\cdot)$ denotes the error function. For the case when $L \rightarrow \infty$, $p_{y_i}(y)$ can be written as

$$\begin{aligned} \lim_{L \rightarrow \infty} p_{y_i}(y) &= \frac{1}{\sqrt{\pi\Omega_i}} e^{-\frac{y^2}{\Omega_i}} \lim_{L \rightarrow \infty} \left[L \operatorname{erf}\left(\frac{y}{\sqrt{\Omega_i}} \tan\left(\frac{\pi}{L}\right)\right) \right] \\ &= \frac{2y}{\Omega_i} e^{-\frac{y^2}{\Omega_i}}, \end{aligned} \quad (5.23)$$

which is the PDF of Rayleigh fading and the system behaves as conventional EGC. It can be easily shown that

$$p_{v_i}(v) = \frac{L}{\sqrt{\pi\gamma}} e^{-\frac{v^2}{\gamma}} \operatorname{erf}\left(\frac{v}{\sqrt{\gamma}} \tan\left(\frac{\pi}{L}\right)\right), \quad (5.24)$$

and the CHF of v_i can be written as

$$\phi_{v_i}(\omega) = \int_0^\infty p_{v_i}(v) e^{j\omega v} dv. \quad (5.25)$$

Substituting (5.24) in (5.25) and using the alternative representation of the error function

$$\operatorname{erf}(x) = 1 - \frac{2}{\pi} \int_0^{\pi/2} e^{-\frac{x^2}{\sin^2(\phi)}} d\phi, \quad (5.26)$$

we obtain the CHF as

$$\begin{aligned} \phi_{v_i}(\omega) &= \frac{L}{2} e^{-\frac{\omega^2\gamma}{4}} - \frac{L}{2} e^{-\frac{\omega^2\gamma}{4}} \operatorname{erf}\left(\frac{\omega\sqrt{\gamma}}{2j}\right) - \frac{L}{\pi} \int_0^{\pi/2} \frac{e^{-\frac{\omega^2\gamma}{4+4\csc^2(\phi)\tan^2(\frac{\pi}{L})}}}{\sqrt{1+\csc^2(\phi)\tan^2(\frac{\pi}{L})}} d\phi + \\ &\quad \frac{L}{\pi} \int_0^{\pi/2} \frac{e^{-\frac{\omega^2\gamma}{4+4\csc^2(\phi)\tan^2(\frac{\pi}{L})}}}{\sqrt{1+\csc^2(\phi)\tan^2(\frac{\pi}{L})}} \operatorname{erf}\left(\frac{\omega\sqrt{\gamma}}{2j\sqrt{1+\csc^2(\phi)\tan^2(\frac{\pi}{L})}}\right) d\phi. \end{aligned} \quad (5.27)$$

The CHF given in (5.27) can be efficiently estimated using the Gauss-Chebyshev quadrature (GCQ) [89, p. 889, Eq. (25.4.38)] as

$$\begin{aligned} \phi_{v_i}(\omega) \approx & \frac{L}{2} e^{-\frac{\omega^2 \pi}{4}} - \frac{L}{2} e^{-\frac{\omega^2 \pi}{4}} \operatorname{erf}\left(\frac{\omega \sqrt{\gamma}}{2j}\right) - \frac{L\pi}{4N_g} \sum_{l=1}^{N_g} \frac{\sqrt{1-\nu_l^2} e^{-\frac{\omega^2 \pi}{4\mathcal{U}(l)}}}{\sqrt{\mathcal{U}(l)}} + \\ & \frac{L\pi}{4N_g} \sum_{l=1}^{N_g} \frac{\sqrt{1-\nu_l^2} e^{-\frac{\omega^2 \pi}{4\mathcal{U}(l)}}}{\sqrt{1 + \csc^2\left(\frac{\pi}{4}(\nu_l + 1)\right) \tan^2\left(\frac{\pi}{L}\right)}} \operatorname{erf}\left(\frac{\omega \sqrt{\gamma}}{2j \sqrt{\mathcal{U}(l)}}\right), \end{aligned} \quad (5.28)$$

where the ν_l 's represent the roots of the the Gauss-Chebyshev polynomial of degree N_g and are the same as given in (4.34), and the function $\mathcal{U}(l)$ is given as

$$\mathcal{U}(l) = 1 + \csc^2\left(\frac{\pi}{4}(\nu_l + 1)\right) \tan^2\left(\frac{\pi}{L}\right). \quad (5.29)$$

The series converges very fast and typically $N_g = 64$ is seen to be sufficient for excellent accuracy. Thus (5.27) or (5.28) together with (5.15) can be used to evaluate the BER for arbitrary L and N_R . An alternative but numerically equivalent CHF for EGC using the Mellin transform based approach is derived in Appendix B.

High SNR Analysis

The BER for high SNR values is dependent on the behavior of the PDF around the origin, i.e., the first non-zero term in the Maclaurin series expansion is sufficient to quantify the performance [94]. The first term in the Maclaurin series expansion of (5.24) is given as

$$p_{v_i}(v) = \frac{2Lv}{\pi\gamma} \tan\left(\frac{\pi}{L}\right). \quad (5.30)$$

Using (5.30), we can formulate the BER at high SNR as

$$P_s = \frac{1}{2\Gamma(1 + N_R)} \left(\frac{N_R L}{2\pi\gamma} \tan\left(\frac{\pi}{L}\right) \right)^{N_R}. \quad (5.31)$$

A detailed derivation of (5.31) is outlined in Appendix C. This can now be compared with [94, Eq. (1)], i.e.,

$$P_s = (G_c \bar{\gamma})^{-G_d}, \quad (5.32)$$

where G_c denotes the coding gain and G_d represents the diversity order. We get

$$G_c = \frac{2\pi (2\Gamma(1 + N_R))^{1/N_R}}{N_R L \tan(\frac{\pi}{L})} \quad \text{and} \quad G_d = N_R. \quad (5.33)$$

Due to the presence of $\tan(\pi/L)$, (5.31) holds for $L > 2$. For the conventional case, i.e., when $L \rightarrow \infty$ we get

$$P_s^C = \lim_{L \rightarrow \infty} P_s = \frac{1}{2^{N_R+1} \Gamma(1 + N_R)} \left(\frac{N_R}{\bar{\gamma}} \right)^{N_R}, \quad (5.34)$$

which gives us

$$G_c^C = \frac{2(2\Gamma(1 + N_R))^{1/N_R}}{N_R} \quad \text{and} \quad G_d^C = N_R. \quad (5.35)$$

For $N_R = 1$, (5.34) reduces to $1/(4\bar{\gamma})$, which is a well known result for BPSK over single branch Rayleigh fading [95, p. 819]. It is interesting to note here that the diversity order is not affected by channel phase quantization. The coding gain on the other hand is scaled by a factor of $\pi/(L \tan(\pi/L))$. Therefore we can write the degradation in system performance Δ as the difference in coding gains (in dB), which gives $\Delta = 10 \log_{10}(G_c/G_c^C)$ at high SNR ($\bar{\gamma} \gg 1$) as

$$\Delta = 10 \log_{10} \left(\frac{\pi}{L \tan(\frac{\pi}{L})} \right). \quad (5.36)$$

5.3.3 Numerical Results

Any of the CHF's (5.27) or (5.28) can be used in conjunction with (5.15) to numerically evaluate the performance of BPSK signalling with RF level EGC over Rayleigh fading channels. In this section we use (5.28) with $N_g = 64$.

PDF and CHF

Figure 5.3 gives a comparison of the analytic and Monte Carlo simulated PDF of EGC for $N_R = 1$ and different phase quantization levels L . The simulation results are seen to be in good agreement with the analysis. As the value of L increases the PDF is seen to approach the conventional Rayleigh fading case. It is good to note here that this behavior is quite similar to the Nakagami- m as m is varied between $1/2$ and 1 .

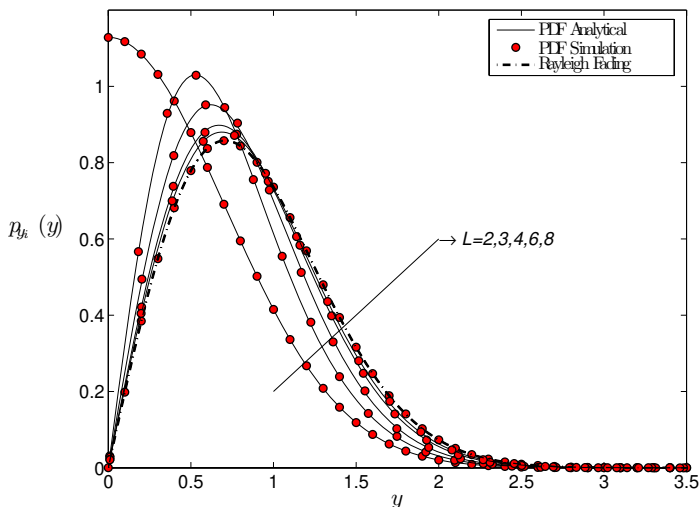


Figure 5.3: Comparison of simulated and analytic PDF of EGC for $N_R = 1$.

The comparison between analysis and simulation for the absolute $|\phi_x(\omega)|$ and phase values $\angle\phi_x(\omega)$ of the CHF using fixed L and different N_R is shown in Figures 5.4 and 5.5, respectively. Here again, the simulation and analysis is seen to be in good agreement.

Error Probability

A comparison of the analytic and Monte Carlo simulated BER for $N_R = 2$ and using various phase quantization levels L , is shown in Figure 5.6. The simulation and analysis is seen to be in perfect agreement. At a BER of 10^{-2} for $N_R = 2$ there is a performance improvement of more than 6 dB, when L is increased from 2 to 3. This is significant in comparison to the case when L is increased from 3 to 4, in which case the gain is only about 1 dB. It can also be seen that for only $L = 4$, the performance is within 1.1 dB of the conventional EGC. This can also be observed with (5.36), which for $L = 4$ gives $\Delta = 1.05$ dB. A comparison between the exact and approximate BER expressions is shown in Figure 5.7. The approximation is very tight in the high SNR regime especially for $\bar{\gamma} > 15$ dB.

Comparison

A comparison with non-coherent BFSK and DBPSK for various values of N_R and L is shown in Figure 5.8. The results for BFSK and DBPSK are obtained as

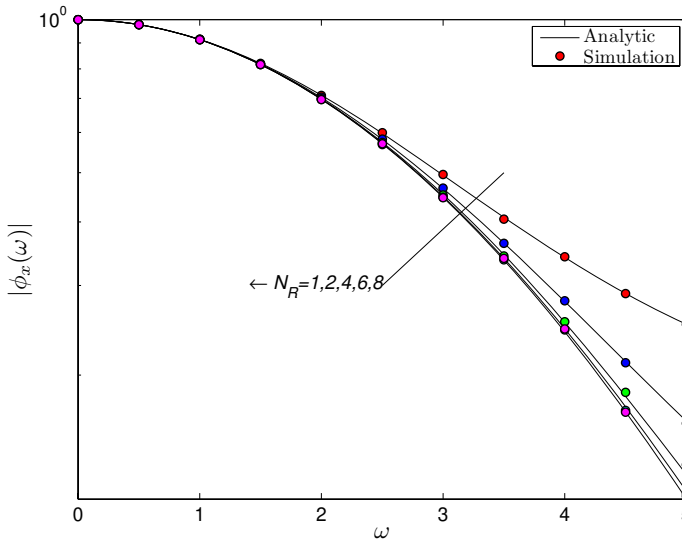


Figure 5.4: Comparison of simulated and analytic $|\phi_x(\omega)|$ for $L = 2$.

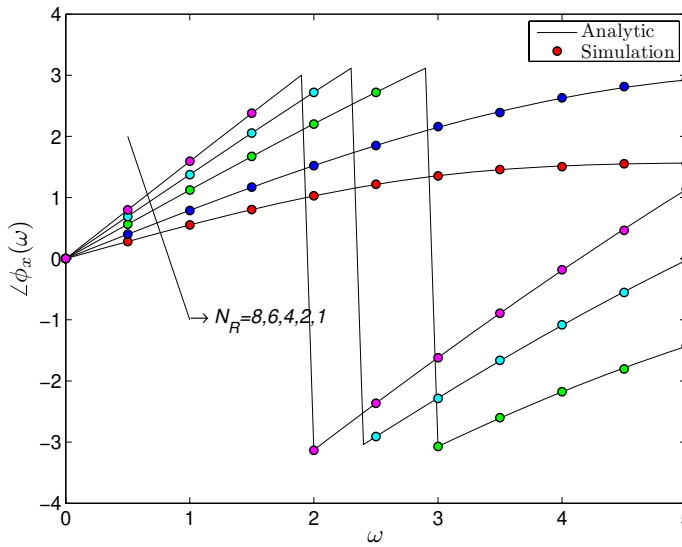


Figure 5.5: Comparison of simulated and analytic $\angle\phi_x(\omega)$ for $L = 2$.

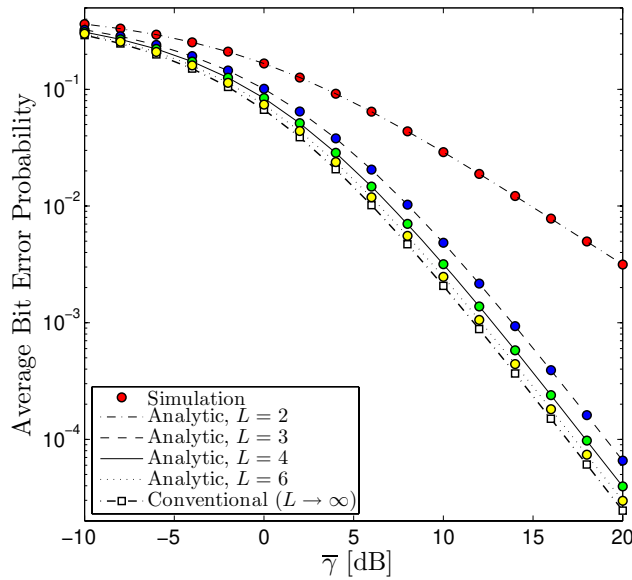


Figure 5.6: A comparison of simulated and analytic BER for $N_R = 2$.

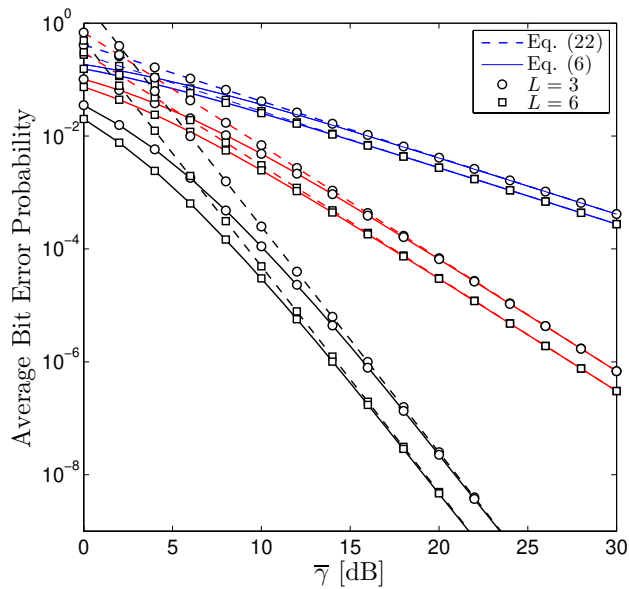


Figure 5.7: A comparison of tight (5.15) and high SNR (5.31) BER for various values of N_R and L .

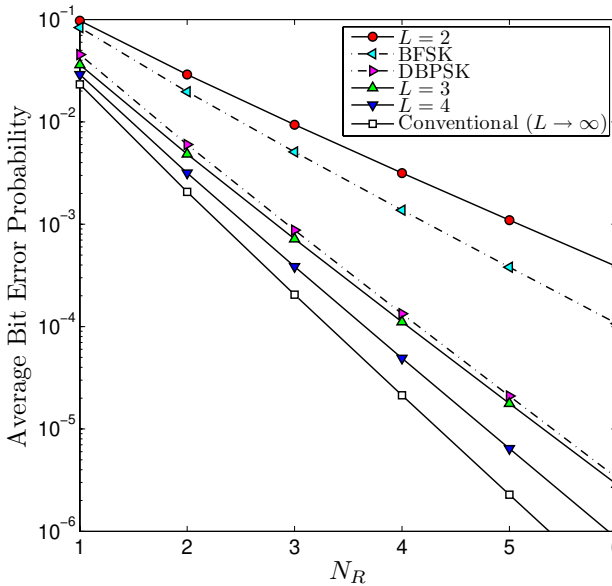


Figure 5.8: BER comparison of BPSK with BFSK and DBPSK at $\bar{\gamma} = 10$ dB.

outlined in [95, p. 825, Eqs. (14.4-15), (14.4-27), (14.4-30)]. It can be seen that both BFSK and DBPSK exhibit a superior performance to BPSK when $L = 2$, i.e., for two level phase compensation. The performance on the other hand is much worse as compared to DBPSK for $L = 2$. In order to achieve superior performance to a conventional DBPSK diversity receiver at least $L = 3$ is required.

System Tradeoffs

The trade-off between N_R and L is highlighted in Figure 5.8, in which the BER is presented as a function of L and N_R for $\bar{\gamma} = 10$ dB. As an example, a target BER of 10^{-3} at an SNR of 10 dB can be achieved by either using $L = 2$ with $N_R = 5$ or using $L = 3$ with $N_R = 3$. The system designer can thus choose for the most cost effective solution.

5.4 RF Level Selection Combining

The performance of SC in various fading scenarios has been extensively reported in the literature. In [45] the performance of non-coherent BFSK over uncorrelated Nakagami- m fading channels with SC is investigated. The performance of SC for differential modulations over correlated Rayleigh fading channels is analyzed

in [46]. The performance of SC for coherent and differential modulations over correlated Nakagami- m fading channels was investigated in [47]. In [48] a unified approach is presented for the error rate evaluation of various coherent and non-coherent modulation schemes over correlated and uncorrelated fading channels with SC. In [44] the performance of SC in the presence of Gaussian distributed weighting errors is analyzed. In this section the impact of imperfect channel co-phasing on the performance of SC is investigated.

The complex baseband signal after RF level SC using (5.1) and Table 5.1 is given as

$$r = \tilde{h}e^{-j\theta^\mathcal{E}} s + \tilde{n}, \quad (5.37)$$

where \tilde{h} denotes the amplitude of the diversity combined signal and \tilde{n} is AWGN with variance $N_0/2$.

5.4.1 Error Probability Analysis for Binary Signals

For the case of BPSK signalling, i.e. $\mathcal{S} \in \{-1, +1\}$, detection is based on the real part of the signal. We can write the real part of (5.37) as

$$r_I = \tilde{h} \cos(\tilde{\theta}^\mathcal{E}) s + \Re[\tilde{n}] = \tilde{h}z s + \Re[\tilde{n}]. \quad (5.38)$$

The instantaneous SNR for SC is defined as $\gamma = x^2$ where

$$x = \sqrt{\frac{E_s}{N_0}} \tilde{h}z = \sqrt{\frac{E_s}{N_0}} y. \quad (5.39)$$

The error probability using (5.38) and (5.39) can be given as

$$P_s = \int_0^\infty P(\epsilon|x) p_x(x) dx. \quad (5.40)$$

The CEP for BPSK signalling is given as

$$P(\epsilon|x) = Q(\sqrt{2}x) = \frac{1}{\pi} \int_0^{\frac{\pi}{2}} e^{-\frac{x^2}{\sin^2(\theta)}} d\theta, \quad (5.41)$$

where $Q(\cdot)$ denotes the Gaussian Q -function and the last equality follows from the alternate representation of the Q -function. Thus in order to determine the error probability we must first determine the PDF of y and x .

For SC we can write the cumulative distribution function (CDF) of \tilde{h} as

$$F_{\tilde{h}}(h) = \prod_{i=1}^{N_R} F_{h_i}(h) = \left(1 - e^{-\frac{h^2}{\Omega}}\right)^{N_R}, \quad h \geq 0, \quad (5.42)$$

where the last equality follows from the fact that each branch is Rayleigh distributed with CDF

$$F_{h_i}(h) = 1 - e^{-\frac{h^2}{\Omega_i}}, \quad h \geq 0. \quad (5.43)$$

We can write the PDF of y as

$$p_y(y) = \int_0^\infty \frac{d}{dy} \left[F_{\tilde{h}}\left(\frac{y}{z}\right) \right] p_z(z) dz, \quad y \geq 0. \quad (5.44)$$

Substituting (5.42) and (5.18) in (5.44), we get

$$p_y(y) = \frac{2yLN_R}{\pi\Omega} \int_{L_c}^1 \frac{e^{-\frac{y^2}{z^2\Omega}} \left(1 - e^{-\frac{y^2}{z^2\Omega}}\right)^{N_R-1}}{z^2\sqrt{1-z^2}} dz, \quad (5.45)$$

where $L_c = \cos(\pi/L)$. By using the Binomial expansion [89, p. 10, Eq. (3.1.1)] and the substitution $z = \sin(\theta)$, we can write (5.45) as

$$p_y(y) = \frac{2yLN_R}{\pi\Omega} \sum_{k=0}^{N_R-1} \binom{N_R-1}{k} (-1)^k \int_{\frac{\pi}{2}-\frac{\pi}{L}}^{\frac{\pi}{2}} \frac{e^{-\frac{y^2(k+1)}{\Omega \sin^2(\theta)}}}{\sin^2(\theta)} d\theta. \quad (5.46)$$

Solving the integral using (A.4) and transforming the result into x using (5.39), we can write the PDF of x as

$$p_x(x) = \frac{LN_R}{\sqrt{\pi\bar{\gamma}}} \sum_{k=0}^{N_R-1} \binom{N_R-1}{k} \frac{(-1)^k}{\sqrt{1+k}} e^{-\frac{(1+k)x^2}{\bar{\gamma}}} \operatorname{erf}\left(\frac{\sqrt{1+k}x \tan(\pi/L)}{\sqrt{\bar{\gamma}}}\right), \quad (5.47)$$

where

$$\bar{\gamma} = \frac{E_s}{N_0} E[y^2], \quad (5.48)$$

is the average SNR per branch. Substituting (5.41) and (5.47) in (5.40) and using the transformation $v = x^2$ we get

$$P_s = \frac{2LN_R}{\pi\sqrt{\pi\bar{\gamma}}} \sum_{k=0}^{N_R-1} \binom{N_R-1}{k} \frac{(-1)^k}{\sqrt{1+k}} \int_0^{\frac{\pi}{2}} \int_0^\infty \frac{1}{\sqrt{v}} \operatorname{erf}\left(\frac{\sqrt{1+k}\sqrt{v}\tan(\pi/L)}{\sqrt{\bar{\gamma}}}\right) e^{-\left(\frac{1}{\sin(\theta)^2} + \frac{(1+k)}{\bar{\gamma}}\right)v} v dv d\theta. \quad (5.49)$$

It can be seen that the inner integral in (5.49) is just the Laplace transform of

$$\mathcal{V}(v) = \frac{1}{\sqrt{v}} \operatorname{erf}\left(\frac{\sqrt{1+k}\sqrt{v}\tan(\pi/L)}{\sqrt{\bar{\gamma}}}\right), \quad (5.50)$$

evaluated at

$$\frac{1}{\sin(\theta)^2} + \frac{(1+k)}{\bar{\gamma}}. \quad (5.51)$$

Thus we can use the moment generating function (MGF) based approach [48] to write the error probability as

$$P_s = \frac{LN_R}{2\pi\sqrt{\pi\bar{\gamma}}} \sum_{k=0}^{N_R-1} \binom{N_R-1}{k} \frac{(-1)^k}{\sqrt{1+k}} \int_0^{\pi/2} L_{\mathcal{V}}\left(\frac{1}{\sin^2(\theta)} + \frac{1+k}{\bar{\gamma}}\right) d\theta, \quad (5.52)$$

where

$$L_{\mathcal{V}}(\omega) = \frac{2}{\sqrt{\omega\pi}} \tan^{-1}\left(\sqrt{\frac{(1+k)\tan^2(\pi/L)}{\omega\bar{\gamma}}}\right), \quad (5.53)$$

denotes the Laplace transform of $\mathcal{V}(v)$. Using GCQ, we can approximate the error probability in closed form as

$$P_s \approx \frac{LN_R\pi}{8N_g\sqrt{\pi\bar{\gamma}}} \sum_{k=0}^{N_R-1} \binom{N_R-1}{k} \frac{(-1)^k}{\sqrt{1+k}} \sum_{l=1}^{N_g} L_{\mathcal{V}}\left(\frac{1}{\sin^2\left(\frac{\pi}{4}(\nu_l+1)\right)} + \frac{1+k}{\bar{\gamma}}\right) \sqrt{1-\nu_l^2}, \quad (5.54)$$

where ν_l denotes the roots of the N_g -th order GC polynomial and are the same as given in (4.34). In our numerical results $N_g = 64$ was seen to be sufficient for excellent accuracy. For all the numerical results presented subsequently, (5.54)

will be used.

5.4.2 Error Probability Analysis for MPSK

Unfortunately the approach introduced in the previous section is not readily applicable for the error probability computation of MPSK signals. In this section we use another approach for the error probability analysis of MPSK signals. The conditional symbol error probability or symbol error rate (SER) for an MPSK signal constellation in the presence of phase error ϕ and amplitude error α over an AWGN channel is given as

$$P(\epsilon|\alpha, \phi) = \begin{cases} \frac{1}{2\pi} \int_0^{\frac{\pi}{M}(M-1)} e^{-\frac{\alpha^2 E_s \sin^2(\frac{\pi}{M} + \phi)}{N_0 \sin^2(\Phi)}} d\Phi + \\ \frac{1}{2\pi} \int_0^{\frac{\pi}{M}(M-1) + \phi} e^{-\frac{\alpha^2 E_s \sin^2(\frac{\pi}{M} - \phi)}{N_0 \sin^2(\Phi)^2}} d\Phi, & \phi \leq \frac{\pi}{M} \\ 1 - \frac{1}{2\pi} \int_{\phi - \frac{\pi}{M}}^{\pi - \frac{2\pi}{M}} e^{-\frac{\alpha^2 E_s \sin^2(\phi - \frac{\pi}{M})}{N_0 \sin^2(\Phi)}} d\Phi + \\ \frac{1}{2\pi} \int_{\phi + \frac{\pi}{M}}^{\pi} e^{-\frac{\alpha^2 E_s \sin^2(\phi + \frac{\pi}{M})}{N_0 \sin^2(\Phi)}} d\Phi - \\ \frac{1}{2\pi} \int_{\pi - \frac{2\pi}{M}}^{\pi} e^{-\frac{\alpha^2 E_s \sin^2(\phi - \frac{\pi}{M})}{N_0 \sin^2(\Phi)}} d\Phi + \\ \frac{1}{2\pi} \int_0^{\frac{\pi}{M}(M-1)} e^{-\frac{\alpha^2 E_s \sin^2(\frac{\pi}{M} + \phi)}{N_0 \sin^2(\Phi)}} d\Phi + \\ \frac{1}{2\pi} \int_0^{\frac{\pi}{M}(M-1) + \phi} e^{-\frac{\alpha^2 E_s \sin^2(\frac{\pi}{M} - \phi)}{N_0 \sin^2(\Phi)^2}} d\Phi, & \phi > \frac{\pi}{M} \end{cases} \quad (5.55)$$

The SER for the first part, i.e., $\phi \leq \pi/M$ follows directly from [96], whereas the second part is derived in Appendix C. The error probability for SC with MPSK can thus be computed as

$$P_s = \int_0^\infty \int_0^\infty P(\epsilon|\tilde{h}, \theta^\mathcal{E}) p_{\theta^\mathcal{E}}(\theta^\mathcal{E}) p_{\tilde{h}}(\tilde{h}) d\theta^\mathcal{E} d\tilde{h}. \quad (5.56)$$

Substituting (5.55) in (5.56) and rearranging we get

$$P_s = \begin{cases} \int_{\frac{\pi}{M}}^{\frac{\pi}{L}} \int_0^\infty p_\gamma(\gamma) p_{\theta^\mathcal{E}}(\theta^\mathcal{E}) d\gamma d\theta^\mathcal{E} + \\ \frac{1}{2\pi} \int_0^{\frac{\pi}{M}} \int_0^{\frac{\pi}{M}(M-1)} \int_0^\infty e^{-\frac{\gamma \sin^2(\frac{\pi}{M} + \theta^\mathcal{E})}{\sin^2(\Phi)}} p_\gamma(\gamma) p_{\theta^\mathcal{E}}(\theta^\mathcal{E}) d\gamma d\Phi d\theta^\mathcal{E} + \\ \frac{1}{2\pi} \int_0^{\frac{\pi}{M}} \int_0^{U_1} \int_0^\infty e^{-\frac{\gamma \sin^2(\frac{\pi}{M} - \theta^\mathcal{E})}{\sin^2(\Phi)^2}} p_\gamma(\gamma) p_{\theta^\mathcal{E}}(\theta^\mathcal{E}) d\gamma d\Phi d\theta^\mathcal{E} - \\ \frac{1}{2\pi} \int_{\frac{\pi}{M}}^{\frac{\pi}{L}} \int_{\theta^\mathcal{E} - \frac{\pi}{M}}^{\pi - \frac{2\pi}{M}} e^{-\frac{\gamma \sin^2(\theta^\mathcal{E} - \frac{\pi}{M})}{\sin^2(\Phi)}} p_\gamma(\gamma) p_{\theta^\mathcal{E}}(\theta^\mathcal{E}) d\gamma d\Phi d\theta^\mathcal{E} + \\ \frac{1}{2\pi} \int_{\frac{\pi}{M}}^{\frac{\pi}{L}} \int_{\theta^\mathcal{E} + \frac{\pi}{M}}^\pi e^{-\frac{\gamma \sin^2(\theta^\mathcal{E} + \frac{\pi}{M})}{\sin^2(\Phi)}} p_\gamma(\gamma) p_{\theta^\mathcal{E}}(\theta^\mathcal{E}) d\gamma d\Phi d\theta^\mathcal{E} - \\ \frac{1}{2\pi} \int_{\frac{\pi}{M}}^{\frac{\pi}{L}} \int_{\pi - \frac{2\pi}{M}}^\pi e^{-\frac{\gamma \sin^2(\theta^\mathcal{E} - \frac{\pi}{M})}{\sin^2(\Phi)}} p_\gamma(\gamma) p_{\theta^\mathcal{E}}(\theta^\mathcal{E}) d\gamma d\Phi d\theta^\mathcal{E}, & L < M \\ \frac{1}{2\pi} \int_0^{\frac{\pi}{L}} \int_0^{\frac{\pi}{M}(M-1)} \int_0^\infty e^{-\frac{\gamma \sin^2(\frac{\pi}{M} + \theta^\mathcal{E})}{\sin^2(\Phi)}} p_\gamma(\gamma) p_{\theta^\mathcal{E}}(\theta^\mathcal{E}) d\gamma d\Phi d\theta^\mathcal{E} + \\ \frac{1}{2\pi} \int_0^{\frac{\pi}{L}} \int_0^{U_1} \int_0^\infty e^{-\frac{\gamma \sin^2(\frac{\pi}{M} - \theta^\mathcal{E})}{\sin^2(\Phi)^2}} p_\gamma(\gamma) p_{\theta^\mathcal{E}}(\theta^\mathcal{E}) d\gamma d\Phi d\theta^\mathcal{E}, & L \geq M \end{cases} \quad (5.57)$$

where

$$\gamma = \tilde{h}^2 \frac{E_s}{N_0}, \quad (5.58)$$

denotes the instantaneous SNR and

$$U_1 = \frac{\pi}{M} (M - 1) + \theta^\mathcal{E}. \quad (5.59)$$

Using [97, p. 278, Eq. (6.7)] and binomial expansion we can write the PDF of the output SNR for SC as

$$p_\gamma(\gamma) = \frac{N_R}{\bar{\gamma}} \sum_{k=0}^{N_R-1} \binom{N_R-1}{k} (-1)^k e^{-\frac{\gamma(k+1)}{\bar{\gamma}}}, \quad (5.60)$$

where

$$\bar{\gamma} = E \left[\tilde{h}^2 \right] \frac{E_s}{N_0}, \quad (5.61)$$

denotes the average SNR. Substituting (5.60) in (5.57) and solving yields

$$P_s = \begin{cases} 1 - \frac{L}{M} + \frac{LN_R}{2\pi^2}(I_1 + I_2) - \frac{LN_R}{2\pi^2\bar{\gamma}}(I_3 - I_4 + I_5) & , L < M \\ \frac{LN_R}{2\pi^2}(I_6 + I_7) & , L \geq M \end{cases} \quad (5.62)$$

where the terms I_1 to I_7 are given in Appendix C.3. It can be seen from (5.62) and the terms given in Appendix C, that the expression of SER for SC is a single finite integral of elementary functions, and therefore, can be efficiently evaluated numerically.

5.4.3 Numerical Results

In this section we validate the analysis with Monte Carlo simulations. We also use the analysis to outline various system level trade-offs and compare the performance with DBPSK and BFSK under diversity reception.

PDF

Figure 5.9 gives a comparison of the analytic and Monte Carlo simulated PDF of SC for $N_R = 1$ and different phase quantization levels L . The simulation results are seen to be in good agreement with the analysis. As the value of L increases the PDF is seen to approach the conventional Rayleigh fading case.

Error Probability

Figures 5.10 and 5.11 give the BER and SER of BPSK and QPSK modulated symbols for SC as a function of the average SNR $\bar{\gamma}$ over Rayleigh fading channels, respectively. The simulation and analysis is seen to be in good agreement. It can be seen that, the system performance improves more for lower values of L as compared to the higher values. This point can be illustrated using figure, in which, there is a drastic improvement in the system performance as L is increased from 2 to 5 for QPSK. For example for SC and a SER of 2.5×10^{-2} the system performance improves by about 7.5 dB when L is increased from 4 to 5, whereas this gain is about 4 dB when the L is increased from 5 to 8. In general the required number of quantization steps will be dependant on the constellation size M and number of diversity branches N_R as can be seen from Figure 5.13.

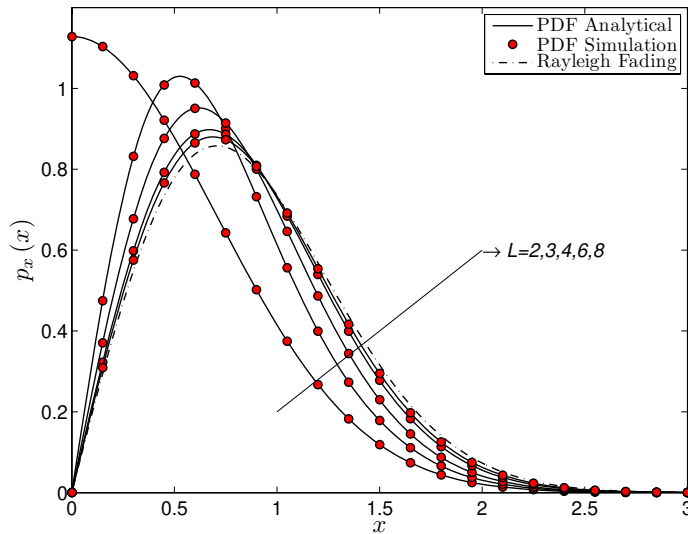


Figure 5.9: Comparison of simulated and analytic PDF of SC for $N_R = 1$.

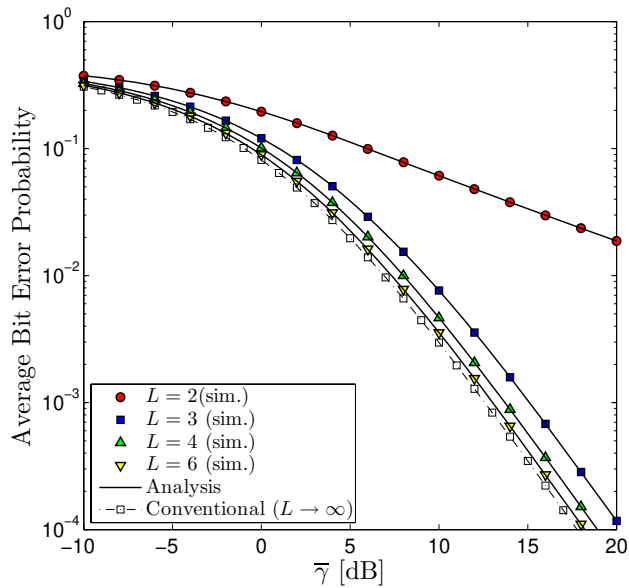


Figure 5.10: A comparison of simulation and analysis for BPSK signal constellation with SC and $N_R = 2$.

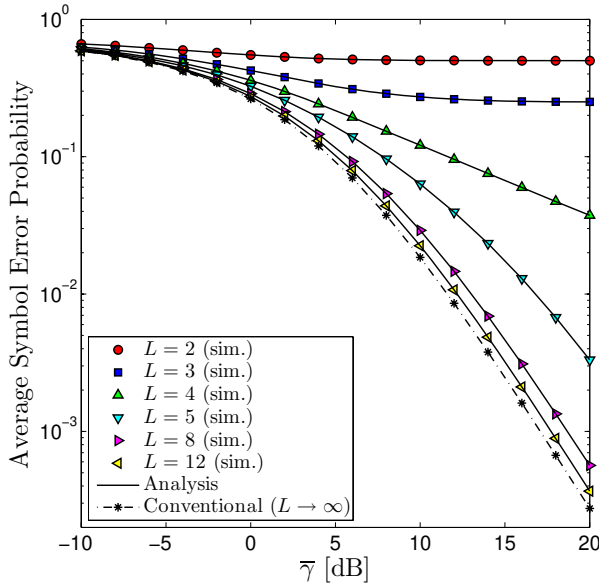


Figure 5.11: A comparison of simulation and analysis for QPSK signal constellation with SC and $N_R = 2$.

Comparison

A comparison with BFSK and DBPSK can also be evaluated using the presented analysis. It can be seen that the number of quantization levels L required to outperform DBPSK and BFSK is dependent on the number of receive diversity branches N_R . For example for a single branch $L = 3$ is sufficient to outperform both BFSK and DBPSK, whereas $L = 4$ is required to do the same when $N_R = 4$.

System Tradeoffs

The presented analysis also allows us to make trade-offs in terms of M , L and N_R . Two such tradeoffs are outlined in Figures 5.12 and 5.13, when SC is employed. Figure 5.13 shows the SER against the number of receive diversity branches N_R for various phase quantization levels L and signal sets M . It can be seen that the number of quantization levels required to achieve performance close to the conventional case is depends on the number the modulation levels M . For example, for 2PSK (BPSK) $L = 4$ is sufficient to attain a SER within 2 times to that of the conventional case, whereas for 4PSK (QPSK) $L = 8$ is required to achieve

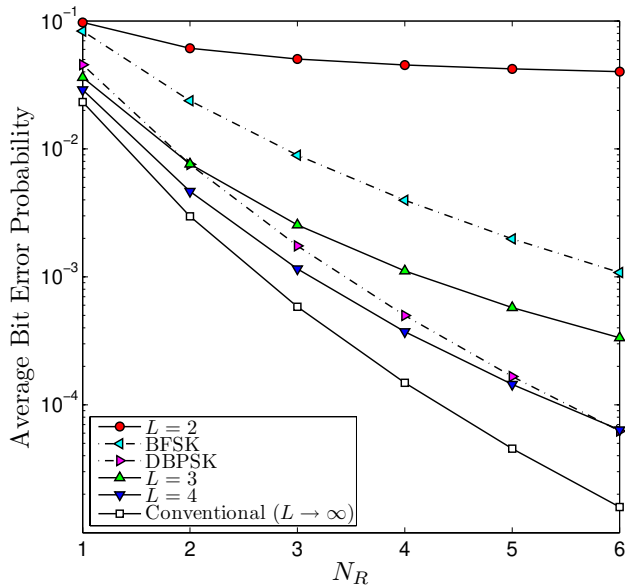


Figure 5.12: BER comparison of BPSK with BFSK and DBPSK at $\bar{\gamma} = 10$ dB.

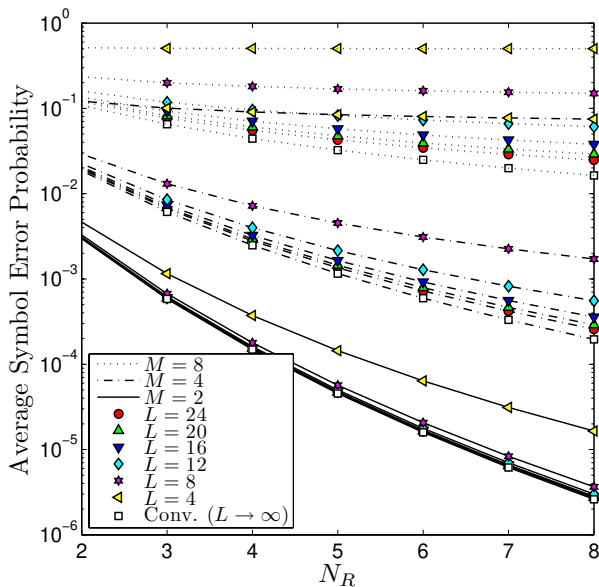


Figure 5.13: SER of QPSK against N_R for various L and M at $\bar{\gamma} = 10$ dB.

this. One can also make a tradeoff between L and the constellation size M . For example, $M = 4$ (QPSK) and $L = 4$ exhibit comparable performance to $M = 8$ (8PSK) and $L = 12$. Similarly, a tradeoff between L and N_R is possible. From Figure 5.12, it can be seen that a BER of 10^{-3} at $\bar{\gamma} = 10$ dB can be achieved with $L = 3$, $N_R = 4$ or with $L = 4$ and $N_R = 3$.

5.5 RF Level Switched Combining

The performance of dual branch SSC and SEC for non-coherent frequency shift keying over Rayleigh fading was reported in [49]. The moment generating function based approach was used in [51, 52], for the performance analysis of dual branch SSC employing various modulation schemes under Nakagami- m and Nakagami- n fading. In [53] the performance analysis of the SEC scheme for Nakagami- m and Nakagami- n fading was carried out. An improved version of SEC, i.e., SECps along with its performance analysis was introduced in [54]. In [55], the performance of pulse amplitude modulated and quadrature amplitude modulated modulated symbols over Rayleigh fading channels with imperfect channel estimates for SSC and SEC was analyzed. The performance of SWC with imperfect combining is still unknown and not reported in the literature. In this section we analyze and investigate the impact of phase shifter quantization noise on the performance of various SWC schemes.

The complex baseband signal after RF level SWC using (5.1) is given as

$$r = \tilde{h}e^{-j\theta^\varepsilon} s + \tilde{n}, \quad (5.63)$$

where \tilde{h} denotes the amplitude of the combined signal and \tilde{n} is the AWGN with variance $N_0/2$.

5.5.1 Error Probability Analysis for Binary Signals

For the case of binary signalling, the real part of (5.63) can be written as

$$r_I = \tilde{h} \cos(\theta^\varepsilon) s + \Re[\tilde{n}], \quad (5.64)$$

For Rayleigh fading, the CDFs for three types of SWC techniques, i.e., SSC, SEC and SECps, using [53,54] are given by

$$\text{SSC : } P_{\tilde{h}}(\tilde{h}) = \begin{cases} 1 - e^{-\frac{r_T^2}{\bar{\gamma}}} + e^{-\left(\frac{\tilde{h}^2 + r_T^2}{\bar{\gamma}}\right)} - e^{-\frac{\tilde{h}^2}{\bar{\gamma}}}, & \tilde{h} < r_T \\ 1 - e^{-\frac{r_T^2}{\bar{\gamma}}} + e^{-\left(\frac{\tilde{h}^2 + h_T^2}{\bar{\gamma}}\right)} - 2e^{-\frac{\tilde{h}^2}{\bar{\gamma}}}, & \tilde{h} \geq r_T, \end{cases} \quad (5.65)$$

$$\text{SEC : } P_{\tilde{h}}(\tilde{h}) = \begin{cases} \left(1 - e^{-\frac{r_T^2}{\bar{\gamma}}}\right)^{N_R-1} \left(1 - e^{-\frac{\tilde{h}^2}{\bar{\gamma}}}\right), & \tilde{h} < r_T \\ \left(e^{-\frac{r_T^2}{\bar{\gamma}}} - e^{-\frac{\tilde{h}^2}{\bar{\gamma}}}\right) \sum_{k=0}^{N_R-1} \left(1 - e^{-\frac{r_T^2}{\bar{\gamma}}}\right)^k + \\ \left(1 - e^{-\frac{r_T^2}{\bar{\gamma}}}\right)^{N_R}, & \tilde{h} \geq r_T, \end{cases} \quad (5.66)$$

and

$$\text{SECps : } P_{\tilde{h}}(\tilde{h}) = \begin{cases} \left(1 - e^{-\frac{\tilde{h}^2}{\bar{\gamma}}}\right)^{N_R}, & \tilde{h} < r_T \\ 1 - e^{-\frac{\tilde{h}^2}{\bar{\gamma}}} \sum_{k=0}^{N_R-1} \left(1 - e^{-\frac{r_T^2}{\bar{\gamma}}}\right)^k, & \tilde{h} \geq r_T, \end{cases} \quad (5.67)$$

respectively. The average SNR per branch for SWC is denoted by

$$\bar{\gamma}_i = \frac{E_s}{N_0} E[h_i^2] = \bar{\gamma}, \quad (5.68)$$

where the last equality follows from the fact that each branch is assumed to have the same average SNR. The error probability is given by

$$P_s = \int_0^\infty P(\epsilon|y) p_y(y) dy, \quad (5.69)$$

where $y = \tilde{h}z$. The CEP for BPSK signalling is given by

$$P(\epsilon|y) = \frac{1}{2} \text{erfc}(y), \quad (5.70)$$

where $\text{erfc}(\cdot)$ denotes the complementary error function [14]. Using the transformation $y = \tan(\eta)$, the error probability given in (5.69) can be written as

$$P_s = \frac{1}{2} \int_0^{\pi/2} \frac{\text{erfc}(\tan(\eta)) p_Y(\tan(\eta))}{\cos(\eta)^2} d\eta. \quad (5.71)$$

The integral given in (5.71) can be efficiently computed using GCQ and therefore the error probability can be approximated in closed form as

$$P_s \approx \frac{\pi^2}{8N_g} \sum_{l=1}^{N_g} \left(\frac{\operatorname{erfc} \left(\tan \left(\frac{\pi}{4} (\nu_l + 1) \right) \right)}{\cos \left(\frac{\pi}{4} (\nu_l + 1) \right)^2} p_y \left(\tan \left(\frac{\pi}{4} (\nu_l + 1) \right) \right) \sqrt{1 - \nu_l^2} \right), \quad (5.72)$$

where ν_l represents the roots of the N_g -th order GC polynomial as given in (4.34). Thus in order to determine the error probability we must first determine the PDF of $y = \tilde{h}z$. We can write the PDF of y as

$$p_y(y) = \int_0^\infty \frac{d}{dy} P_{\tilde{h}} \left(\frac{y}{z} \right) p_z(z) dz. \quad (5.73)$$

In what follows, we determine the PDF of y for SSC, SEC and SECps. Once the PDF is known the error probability can easily be evaluated using (5.72).

PDF of SSC

The PDF of SSC obtained by substituting (5.65) in (5.73) and transforming the limits is given as

$$p_y(y) = \frac{2Ly}{\tilde{\gamma}\pi} \int_{L_1(y)}^1 \frac{e^{-\frac{y^2}{\tilde{\gamma}z^2}} - e^{-\frac{y^2}{\tilde{\gamma}z^2} - \frac{r_T^2}{\tilde{\gamma}}}}{z^2 \sqrt{1 - z^2}} dz + \frac{2Ly}{\tilde{\gamma}\pi} \int_{L_c}^{L_2(y)} \frac{2e^{-\frac{y^2}{\tilde{\gamma}z^2}} - e^{-\frac{y^2}{\tilde{\gamma}z^2} - \frac{r_T^2}{\tilde{\gamma}}}}{z^2 \sqrt{1 - z^2}} dz, \quad (5.74)$$

where

$$L_1(x) = \min \left\{ \max \left\{ \frac{x}{r_T}, \cos \left(\frac{\pi}{L} \right) \right\}, 1 \right\}, \quad (5.75)$$

$$L_2(x) = \max \left\{ \min \left\{ 1, \frac{x}{r_T} \right\}, \cos \left(\frac{\pi}{L} \right) \right\} \quad (5.76)$$

and

$$L_c = \cos \left(\frac{\pi}{L} \right). \quad (5.77)$$

The operators $\max \{a, b\}$ and $\min \{a, b\}$ are used to represent the maximum and minimum of two real numbers a and b . By solving the integral in (5.74), we can

write the PDF as

$$p_y(y) = \frac{Le^{-\left(\frac{y^2+r_T^2}{\gamma}\right)} \left(e^{\frac{r_T^2}{\gamma}} - 1\right)}{\sqrt{\pi\gamma}} \operatorname{erf}\left(\frac{y\sqrt{1-L_1(y)^2}}{\sqrt{\gamma}L_1(y)}\right) + \frac{Le^{-\left(\frac{y^2+r_T^2}{\gamma}\right)} \left(2e^{\frac{r_T^2}{\gamma}} - 1\right)}{\sqrt{\pi\gamma}} \left(\operatorname{erf}\left(\frac{y \tan\left(\frac{\pi}{L}\right)}{\sqrt{\gamma}}\right) - \operatorname{erf}\left(\frac{y\sqrt{1-L_2(y)^2}}{\sqrt{\gamma}L_2(y)}\right)\right). \quad (5.78)$$

PDF of SEC

Substituting (5.66) in (5.73) and transforming the limits yields the PDF of SEC as

$$p_y(y) = \frac{2Ly}{\gamma\pi} \left(1 - e^{-\frac{r_T^2}{\gamma}}\right)^{N_R-1} \int_{L_1(y)}^1 \frac{e^{-\frac{y^2}{z^2\gamma}}}{z^2\sqrt{1-z^2}} dz + \frac{2Ly}{\gamma\pi} \left(1 - \left(1 - e^{-\frac{r_T^2}{\gamma}}\right)^{N_R}\right) \int_{L_c}^{L_2(y)} \frac{e^{-\left(\frac{y^2}{z^2\gamma} - \frac{r_T^2}{\gamma}\right)}}{z^2\sqrt{1-z^2}} dz. \quad (5.79)$$

We can solve the integral in (5.79) and write the PDF as

$$p_y(y) = \frac{Le^{-\frac{y^2}{\gamma}}}{\sqrt{\pi\gamma}} \left(1 - e^{\frac{h_T^2}{\gamma}}\right)^{N_R-1} \operatorname{erf}\left(\frac{y\sqrt{1-L_1(y)^2}}{\sqrt{\gamma}L_1(y)}\right) + \frac{Le^{-\frac{y^2}{\gamma}} e^{\frac{h_T^2}{\gamma}}}{\sqrt{\pi\gamma}} \left(1 - \left(1 - e^{-\frac{h_T^2}{\gamma}}\right)^{N_R}\right) \left(\operatorname{erf}\left(\frac{y \tan\left(\frac{\pi}{L}\right)}{\sqrt{\gamma}}\right) - \operatorname{erf}\left(\frac{y\sqrt{1-L_2(y)^2}}{\sqrt{\gamma}L_2(y)}\right)\right). \quad (5.80)$$

PDF of SECps

For the case of SECps, the PDF is calculated by substituting (5.67) in (5.73) as

$$p_y(y) = \frac{2LyN_R}{\bar{\gamma}\pi} \sum_{k=0}^{N_R-1} \binom{N_R-1}{k} (-1)^k \int_{L_1(y)}^1 \frac{e^{-\frac{y^2(k+1)}{z^2\bar{\gamma}}}}{z^2\sqrt{1-z^2}} dz + \frac{2Ly \left(1 - \left(1 - e^{-\frac{r_T^2}{\bar{\gamma}}}\right)^{N_R}\right)}{\bar{\gamma}\pi} \int_{L_c}^{L_2(y)} \frac{e^{-\left(\frac{y^2}{z^2\bar{\gamma}} - \frac{r_T^2}{\bar{\gamma}}\right)}}{z^2\sqrt{1-z^2}} dz. \quad (5.81)$$

We can solve the integral in (5.81) and write the PDF as

$$p_y(y) = \frac{N_R L}{\sqrt{\pi\bar{\gamma}}} \sum_{k=0}^{N_R-1} \binom{N_R-1}{k} \frac{(-1)^k}{\sqrt{1+k}} e^{-\frac{(1+k)y^2}{\bar{\gamma}}} \operatorname{erf}\left(\frac{y\sqrt{(1+k)(1-L_1(y)^2)}}{\sqrt{\bar{\gamma}}L_1(y)}\right) + \frac{L e^{-\left(\frac{y^2-h_T^2}{\bar{\gamma}}\right)} \left(1 - \left(1 - e^{-\frac{h_T^2}{\bar{\gamma}}}\right)^{N_R}\right)}{\sqrt{\pi\bar{\gamma}}} \left(\operatorname{erf}\left(\frac{y \tan\left(\frac{\pi}{L}\right)}{\sqrt{\bar{\gamma}}}\right) - \operatorname{erf}\left(\frac{y\sqrt{1-L_2(y)^2}}{\sqrt{\bar{\gamma}}L_2(y)}\right)\right). \quad (5.82)$$

We can compute the BER by substituting any of the equations (5.78), (5.80) or (5.82) in (5.72).

5.5.2 Error Probability Analysis for MPSK

The same general approach as was applied for the error probability evaluation of MPSK signals in SC can also be utilized to determine the error probability of various switched combining schemes employing multi-level PSK signalling.

Switch and Stay Combining

The PDF of the combined signal at the output of a dual branch SSC for i.i.d. Rayleigh fading channels is given as [14, p. 421, Eq. (9.275)]

$$p_\gamma(\gamma) = \begin{cases} \frac{1}{\bar{\gamma}} \left(1 - e^{-\frac{\gamma T}{\bar{\gamma}}}\right) e^{-\frac{\gamma}{\bar{\gamma}}}, & \gamma < \gamma_T, \\ \frac{1}{\bar{\gamma}} \left(2 - e^{-\frac{\gamma T}{\bar{\gamma}}}\right) e^{-\frac{\gamma}{\bar{\gamma}}}, & \gamma \geq \gamma_T \end{cases}. \quad (5.83)$$

The switching threshold γ_T is related with r_T as

$$\gamma_T = \frac{E_s}{N_0} r_T^2. \quad (5.84)$$

Substituting (5.83) in (5.57) and simplifying using GCQ we can approximate the error probability as

$$P_s \approx \begin{cases} 1 - \frac{L}{M} + \frac{L}{2\pi^2} (I_8 + I_9 + I_{10} + I_{11} - I_{12} + I_{13} - I_{14} + I_{15}) & , L < M \\ \frac{L}{2\pi^2} (I_{16} + I_{17} + I_{18} + I_{19}) & , L \geq M \end{cases} \quad (5.85)$$

where the terms I_8 to I_{19} are outlined in Appendix C.4.

Switch and Examine Combining

A similar approach as outlined in the previous section can be used for evaluating the error probability for SEC. Using [14, p. 440, Eq. (9.341)] and binomial expansion the PDF of SEC is given as

$$p_\gamma(\gamma) = \begin{cases} \frac{1}{\gamma} \left(1 - e^{-\frac{\gamma T}{\gamma}}\right)^{N_R-1} e^{-\frac{\gamma}{\gamma}}, & \gamma < \gamma_T, \\ \frac{e^{-\frac{\gamma}{\gamma}}}{\gamma} \sum_{k=0}^{N_R-1} \left(1 - e^{-\frac{\gamma T}{\gamma}}\right)^k, & \gamma \geq \gamma_T \end{cases}, \quad (5.86)$$

By, substituting (5.86) in (5.57) and simplifying using GCQ we can approximate the error probability as

$$P_s \approx \begin{cases} L \left(\frac{1}{L} - \frac{1}{M}\right) \left(1 - e^{-\frac{\gamma T}{\gamma}}\right)^{N_R-1} \left(1 - e^{-\frac{\gamma T}{\gamma}}\right) + \\ L e^{-\frac{\gamma T}{\gamma}} \left(\frac{1}{L} - \frac{1}{M}\right) \sum_{k=0}^{N_R-1} \left(1 - e^{-\frac{\gamma T}{\gamma}}\right)^k - \frac{L}{M} \left(1 - e^{-\frac{\gamma T}{\gamma}}\right)^{N_R-1} \left(\frac{1}{L} - \frac{1}{M}\right) + \\ I_{20} + I_{21} - I_{22} - I_{23} + I_{24} + I_{25} - I_{26} - I_{27} + I_{28} + I_{29}, & L < M \\ \frac{(M-1)}{M} \left(1 - e^{-\frac{\gamma T}{\gamma}}\right)^{N_R-1} - I_{30} - I_{31} - I_{32} - I_{33}, & L \geq M \end{cases} \quad (5.87)$$

where the terms I_{20} to I_{33} are given in Appendix C.5. Here again, it is good to point out that the SER expression is in the form of a single finite integral of elementary functions and therefore can be efficiently evaluated numerically.

Switch and Examine Combining with Post Selection

The general approach outlined for error probability calculation of SEC and SSC also holds for SECps. Here again by using the binomial expansion on [14, p. 444, Eq. (9.347)] we can write the PDF of SECps as

$$p_\gamma(\gamma) = \begin{cases} \frac{N_R}{\gamma} \sum_{k=0}^{N_R-1} \binom{N_R-1}{k} (-1)^k e^{-(k+1)\frac{\gamma}{\gamma_T}}, & \gamma < \gamma_T, \\ \frac{1}{\gamma} \left(1 - \left(1 - e^{-\frac{\gamma_T}{\gamma}}\right)^{N_R}\right) e^{\frac{\gamma_T}{\gamma}} e^{-\frac{\gamma}{\gamma_T}}, & \gamma \geq \gamma_T \end{cases} \quad (5.88)$$

Substituting (5.88) in (5.57) and simplifying using GCQ we can approximate the error probability as

$$P_s \approx \begin{cases} LN_R \left(\frac{1}{L} - \frac{1}{M}\right) \sum_{k=0}^{N_R-1} \frac{\binom{N_R-1}{k} (-1)^k}{1+k} \left(1 - e^{-\frac{\gamma_T(1+k)}{\gamma}}\right) + \\ L \left(\frac{1}{L} - \frac{1}{M}\right) \left(1 - \left(1 - e^{-\frac{\gamma_T}{\gamma}}\right)^{N_R}\right) + I_{34} - I_{35} + I_{36} - \\ I_{37} + I_{38} + I_{39} - I_{40} + I_{41} - I_{42} - I_{43} + I_{44} - I_{45}, & L < M \\ I_{46} - I_{47} + I_{48} - I_{49} + I_{50} + I_{51}, & L \geq M \end{cases} \quad (5.89)$$

where the terms I_{34} to I_{51} are outlined in Appendix C.6.

5.5.3 Numerical Results

In this section we validate the analysis with Monte Carlo simulations. We also use the analysis to outline various system level trade-offs and compare the performance with DBPSK and BFSK under diversity reception.

PDF

Figures 5.14, 5.15 and 5.16 give a comparison of the analytic and Monte Carlo simulated PDF of SSC, SEC and SECps for $N_R = 2$ and different phase quantization levels L , respectively. The simulation results are seen to be in good agreement with the analysis. As the value of L increases the PDF is seen to approach the conventional case. It can be seen in all the three cases for SWC that for $L = 2$ there is a higher probability of deep fade, which is evident by the large area under the probability curve for $y < 0.5$. It is worthwhile to note here that the channel phase quantization affects the channel fading behavior (characteristics) and can

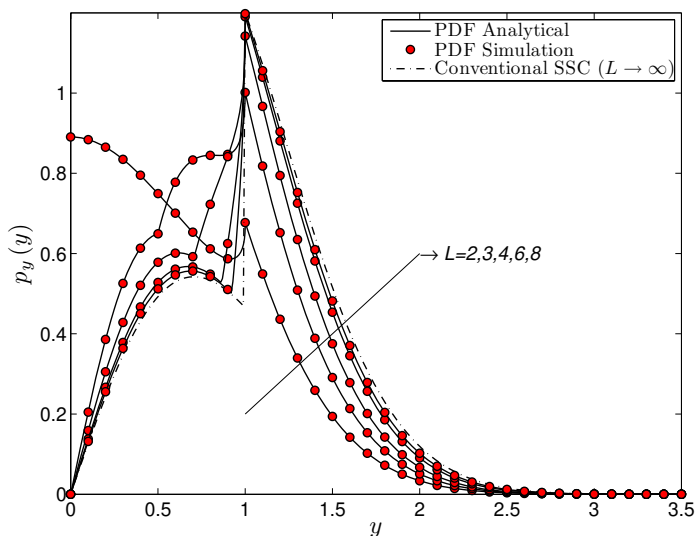


Figure 5.14: Comparison of simulated and analytic PDF of SSC for $N_R = 2$.

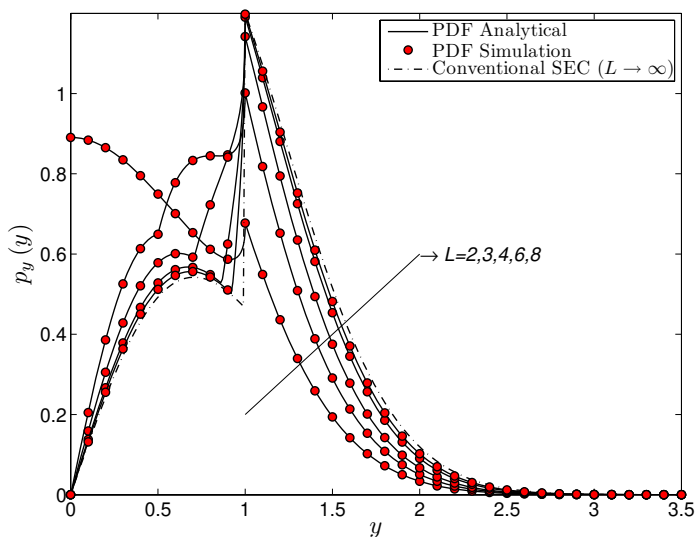


Figure 5.15: Comparison of simulated and analytic PDF of SEC for $N_R = 2$.

lead to severe fading for very low values of L . As the value of L increases this area becomes less and the PDF approaches the conventional case. Since the SWC combining is a non-linear combining scheme the PDF is also not a linear function.

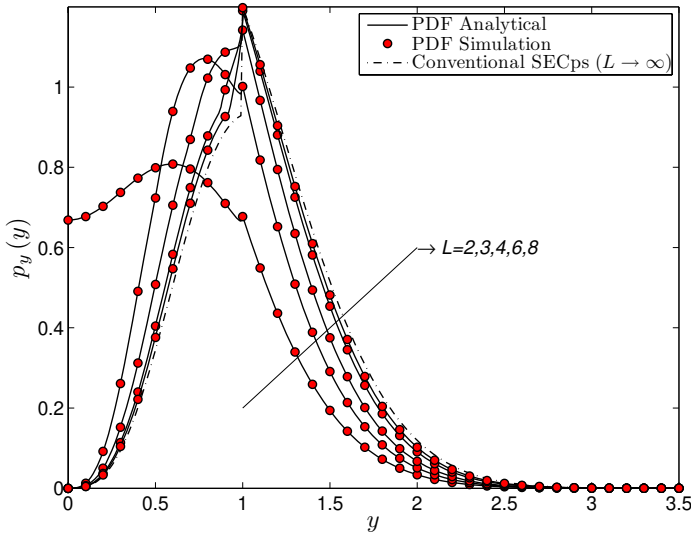


Figure 5.16: Comparison of simulated and analytic PDF of SECps for $N_R = 2$.

It shows a discontinuity around the switching threshold which in these figures is set to unity.

Error Probability

Figures 5.17 and 5.18 give the BER and SER of BPSK and QPSK modulated symbols for SSC against average SNR $\bar{\gamma}$ over Rayleigh fading channels, respectively. Similar results for SEC and SECps are shown in Figures 5.19, 5.20, 5.21 and 5.22. The simulation and analysis is seen to be in good agreement in all the figures.

As explained in the previous section, the signal fading is quite severe for $L = 2$. Therefore, the system performance is expected to be much worse when compared to the conventional case. For example, when SSC is used with $L = 2$, BPSK, $N_R = 2$ and $\gamma_T = 10$ dB (Figure 5.17) an SNR of around 18 dB is required to achieve a BER of 3×10^{-2} as compared to 5 dB for the conventional case. This gives us a gap of 13 dB in the system performance. Whereas, for the same combining and modulation scheme, an SNR of 7 dB is required when $L = 3$ is utilized. Furthermore, the system performance does not improve evenly across the quantization steps L . For instance, with SSC and an SER of 2.5×10^{-2} , the system performance improves by about 7 dB when L is increased from 4 to 5,

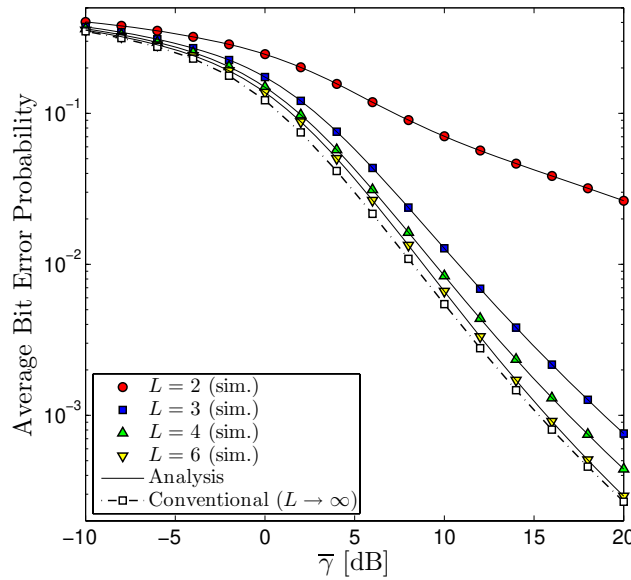


Figure 5.17: A comparison of simulation and analysis for BPSK signal constellation with SSC, $\gamma_T = 10$ dB and $N_R = 2$.

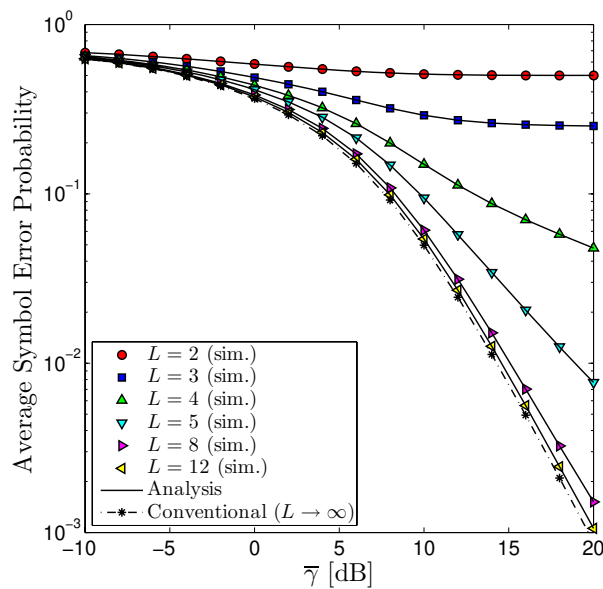


Figure 5.18: A comparison of simulation and analysis for QPSK signal constellation with SSC, $\gamma_T = 10$ dB and $N_R = 2$.

whereas this gain is about 3 dB when the L is increased from 5 to 6. In general the required number of quantization steps will be dependant on the constellation size M and number of diversity branches N_R as can be seen from Figures 5.27 and 5.28.

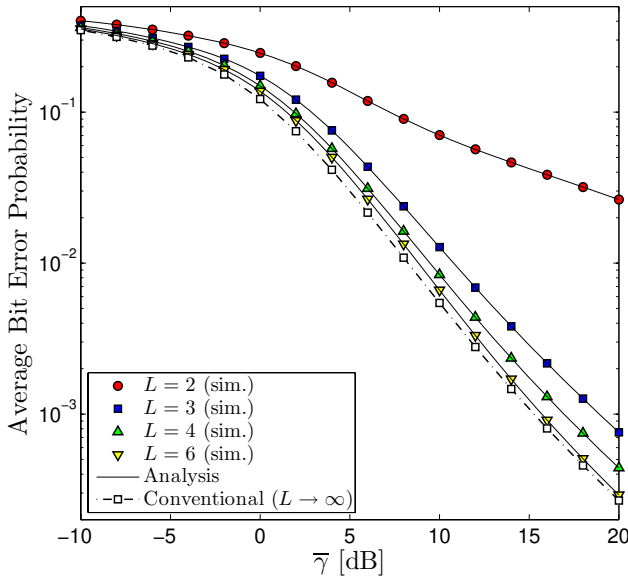


Figure 5.19: A comparison of simulation and analysis for BPSK signal constellation with SEC, $\gamma_T = 10$ dB and $N_R = 2$.

Switching Threshold

The switching threshold γ_T (or r_T) is a critical parameter for switched diversity combining transceivers. Choosing a very low value for γ_T results in unnecessary switching. On the other hand choosing it too high will result in no switching for SSC and SEC and no diversity advantage will be gained in that case. For SECps choosing a very high threshold will turn the system into a selection combiner. Figures 5.23 and 5.24 show the BER and SER against switching threshold γ_T for dual branch SSC and SECps. Since the performance of SSC and SEC for $N_R = 2$ is the same, the curves for SEC are not shown. It can be seen from Figures 5.23 and 5.24 that the optimum switching threshold is not severely affected by channel phase quantization and the optimum value for the RF level selection case is quite close to that of the conventional case. All optimum switching thresholds

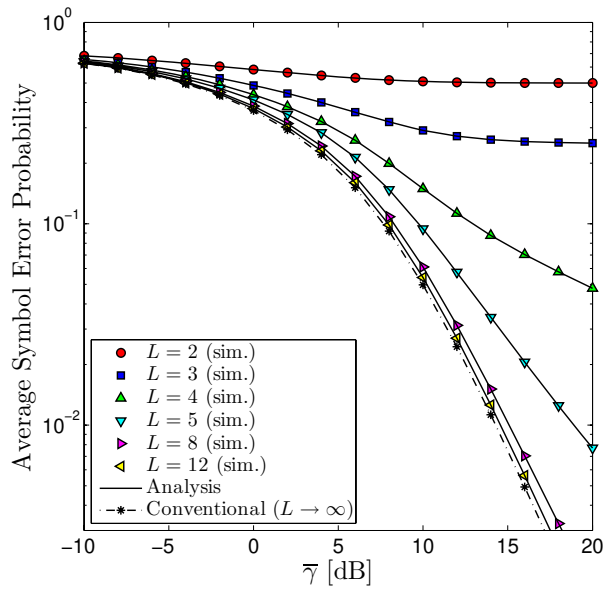


Figure 5.20: A comparison of simulation and analysis for QPSK signal constellation with SEC, $\gamma_T = 10$ dB and $N_R = 2$.

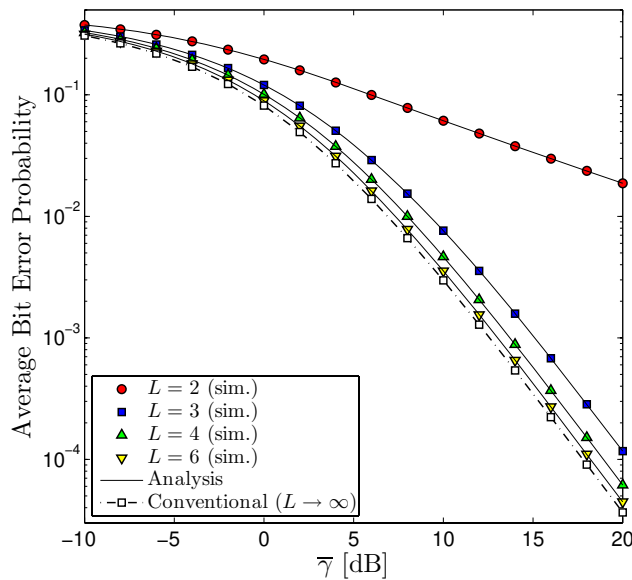


Figure 5.21: A comparison of simulation and analysis for BPSK signal constellation with SECps, $\gamma_T = 10$ dB and $N_R = 2$.

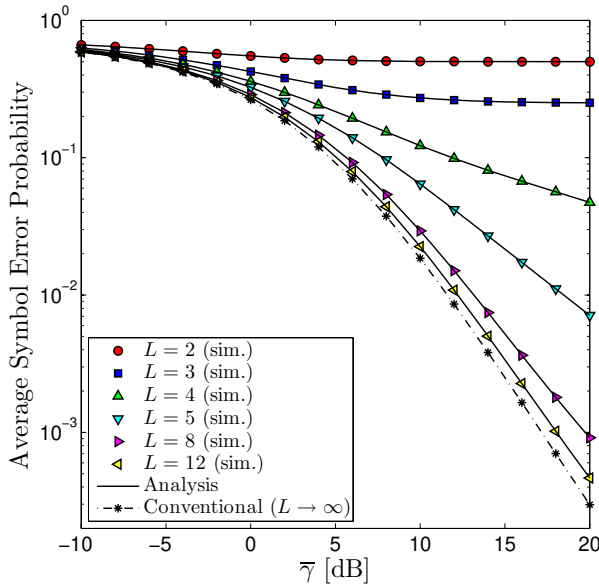


Figure 5.22: A comparison of simulation and analysis for QPSK signal constellation with SECps, $\gamma_T = 10$ dB and $N_R = 2$.

lie between 1 dB and 3 dB for BPSK. The derivative of the SER expressions (5.85), (5.87) and (5.89) with respect to γ_T is cumbersome to compute, therefore classical gradient descent based algorithms cannot be applied for BER optimization. However, (5.85), (5.87) and (5.89) can be used as a cost functions with any standard unconstrained numerical optimization technique [98] to obtain the optimized switching threshold γ_T .

Comparison to BFSK and DBPSK

A comparison with BFSK and DBPSK can also be drawn using the presented analysis as shown in Figures 5.25 and 5.26. It can be seen that the number of quantization levels L required to outperform DBPSK and BFSK does not dependent on the number of receive diversity branches N_R . $L = 3$ is sufficient to outperform BFSK and DBPSK for both SEC and SECps.

System Level Tradeoffs

The presented analysis also allows us to make trade-off in terms of M , L and N_R . Two such tradeoffs are outlined in Figures 5.25 and 5.27, when SEC is employed, and in Figures 5.26 and 5.28, when SECps is used. Figure 5.27 shows the SER

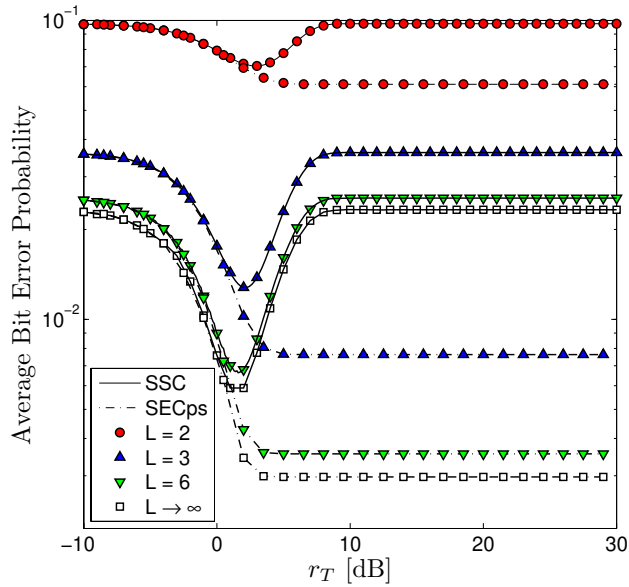


Figure 5.23: Impact of switching threshold on the BER of BPSK for dual branch SSC and SECps at $\bar{\gamma} = 10$ dB.

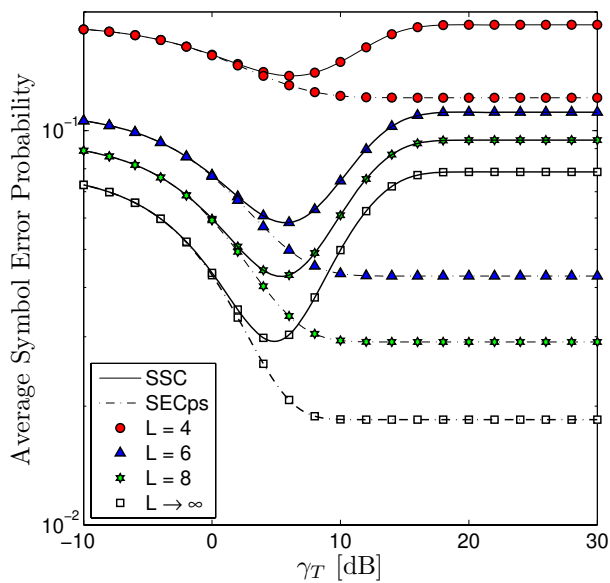


Figure 5.24: Impact of switching threshold on the SER of QPSK for dual branch SEC and SECps at $\bar{\gamma} = 10$ dB.

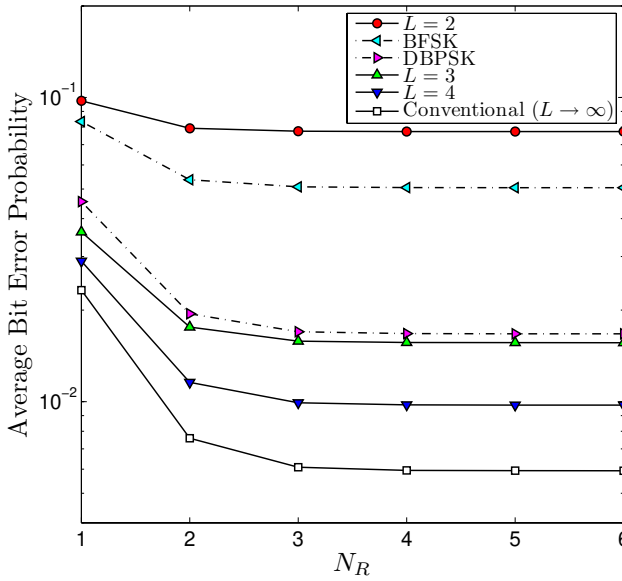


Figure 5.25: BER comparison of BPSK for SEC with BFSK and DBPSK at $\bar{\gamma} = 10$ dB and $\gamma_T = 10$ dB.

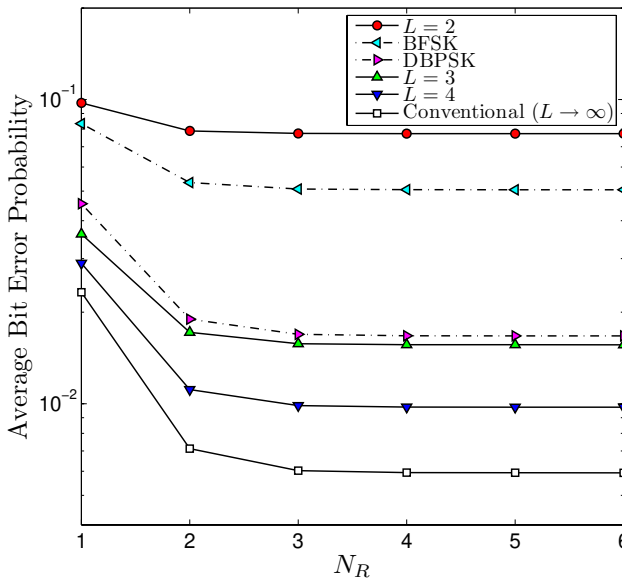


Figure 5.26: BER comparison of BPSK for SECps with BFSK and DBPSK at $\bar{\gamma} = 10$ dB and $\gamma_T = 10$ dB.

against the number of diversity branches N_R for various phase quantization levels L and signal sets M for SEC. It can be seen from the Figure that the number of quantization levels required to achieve performance close to the conventional case are dependent on the number the modulation levels M . For example, for BPSK $L = 8$ is sufficient to attain a SER within 2 times to that of the conventional case, whereas for QPSK $L = 12$ is required to the achieve this. One can also tradeoff L for spectral efficiency M . For example, $M = 4$ (QPSK) and $L = 4$ exhibit comparable performance to $M = 8$ (8PSK) and $L = 12$ for SEC and SECps. Similarly, a tradeoff between L and N_R is also possible. From Figure 5.25, it can be seen that a BER of 3×10^{-2} at $\bar{\gamma} = 10$ dB can be achieved with $L = 3$, $N_R = 2$ or with $L = 4$ and $N_R = 1$ when SEC is used.

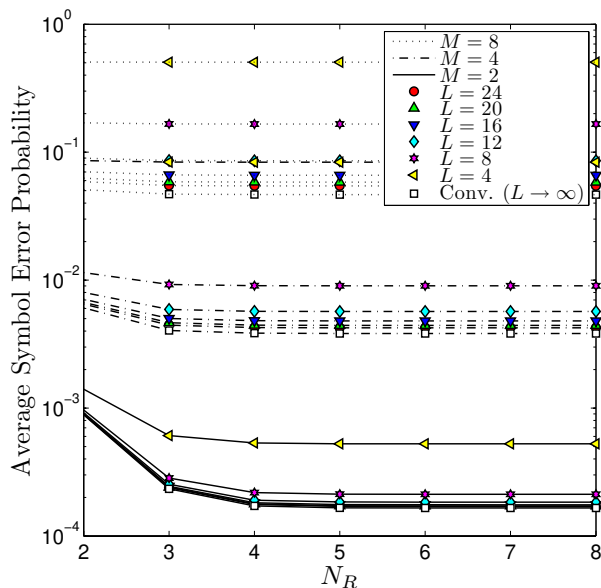


Figure 5.27: SER of QPSK for SEC against N_R for various L and M at $\bar{\gamma} = 5$ dB and $\gamma_T = 10$ dB.

5.6 Comparison

The presented analysis also enables us to make a performance comparison between EGC, SC and SWC. One such comparison using EGC, SC and SEC is depicted in Figure 5.29, in which the average BER is shown against the average SNR for

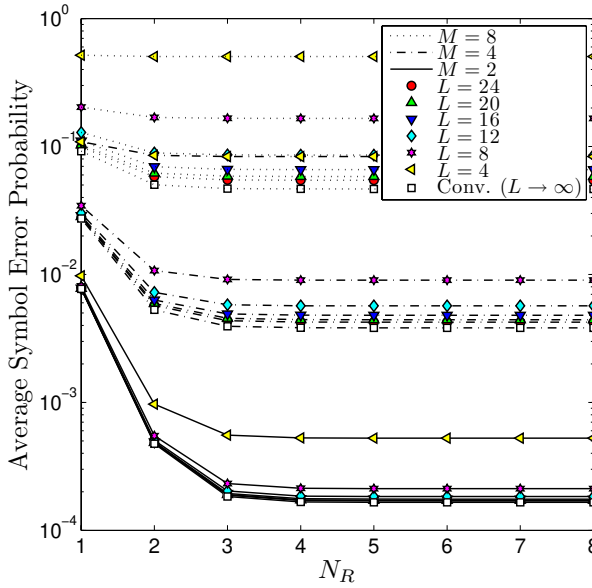


Figure 5.28: SER of QPSK for SECps against N_R for various L and M at $\bar{\gamma} = 5$ dB and $\gamma_T = 10$ dB.

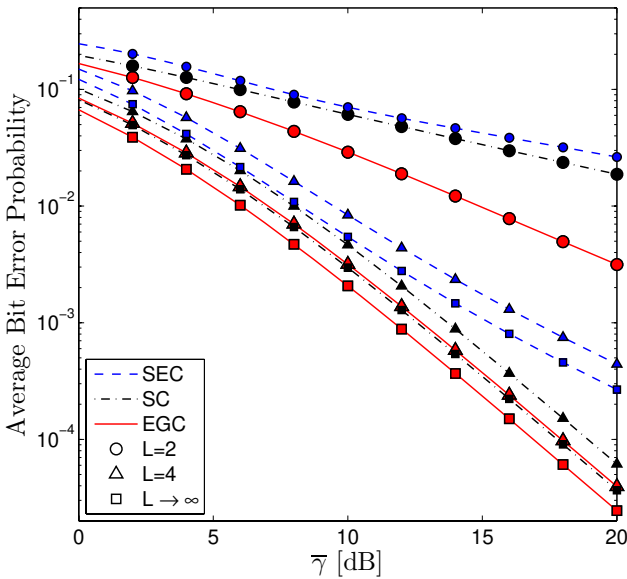


Figure 5.29: SER of QPSK for SEC against N_R for various L and M at $\bar{\gamma} = 5$ dB and $\gamma_T = 10$ dB.

various phase quantization levels L over Rayleigh fading channels. The SEC with the lowest implementation complexity exhibits the least performance. For $L = 2$, the SEC and SC are about 1 dB apart at a BER of 3×10^{-2} while EGC at the same BER performs about 7 dB better than SC and about 8 dB better than SEC. At the same BER the performance of SC and SEC is more drastically improved for SC and SEC schemes as compared to the EGC. For example a performance improvement of about 12 dB and 13 dB is seen for SC and SEC schemes when L is increased from 2 to 4, whereas this improvement is about 5 dB for EGC.

This also enables one to tradeoff and interchange the diversity combining scheme according to the system complexity and power consumption requirements. For example, a BER of 10^{-2} with the system link margin of around 15 dB can be achieved using $L = 2$ with EGC or by using $L = 4$ with SC and SEC.

5.7 Conclusions

The impact of channel phase quantization on the performance of RF level EGC was investigated. BER expressions for EGC and BPSK signalling over Rayleigh fading channels were derived and used to compare the performance with non coherent BFSK and DBPSK under diversity reception. It was shown that for only 3 level phase compensation BPSK exhibits superior performance to both BFSK and DBPSK. A closed form asymptotic error rate expression was used to determine the diversity order, coding gain and the degradation in system performance. It was shown the the diversity order is independent of the phase quantization levels L and the degradation in system performance is dependant only on L . The ability to make a system level trade-off between L and N_R has been demonstrated.

Performance analysis of SC, SSC, SEC and SECps with quantized channel estimates was presented. Analytical expressions for for the SER of MPSK modulated symbols over Rayleigh fading channels were derived. The derived expressions were then utilized to compare the performance with DBPSK and BFSK schemes under diversity reception. It was shown that the number of quantization levels L required to achieve near ideal performance are dependent on the number of the receive antennas N_R and the modulation level M . The analysis was utilized to investigate the impact of phase quantization on the switching threshold. It was shown that the switching threshold is not severely affected by phase quantization. The ability to perform various system level trade-offs was also demonstrated.

Chapter 6

Acoustic Demonstrator

In this chapter, the design of a low cost acoustic demonstrator is described. Path loss and CIR measurements are performed at 10 kHz and 68 kHz and compared with 60 GHz transmission scenarios. The BER of un-coded single-carrier and multi-carrier techniques on both acoustic and radio channels is also compared.

6.1 Introduction

The development of a simple demonstrator for the design and verification for baseband processing algorithms at a carrier frequency of 60 GHz presents two major challenges. Firstly, due to high sampling rate requirements the required hardware is expensive, if available at all. Secondly, the digital signal processor has to be directly programmed which shifts the focus from algorithm design and verification to cumbersome DSP based implementation. In order to alleviate these concerns a low cost acoustic based demonstrator is proposed in this chapter. The major advantage of such an approach is that, it is low-cost and the programming can be done with relative ease in a MATLAB environment which allows us to focus more on algorithm design rather than implementation. Two approaches are investigated for the development of a simplified test-bed based on audio at ultrasonic frequencies. From now onwards, the term audio frequency (AF) is used for the 10 kHz band while ultrasonic frequency (UF) denotes the 68 kHz band. Both the AF and UF are collectively referred to as acoustic frequency in this thesis. The basic idea behind both approaches is to achieve a multi-path rich environment similar to 60 GHz transmission scenarios. In the first approach an appropriate scaling of the acoustic transmission frequency yields the same wavelength as 60 GHz radio waves, i.e., 5 mm. The receiver array design for 68 kHz directly follows from that of the 60 GHz band, due to wavelength similarity. In the second scenario we perform channel measurements at 10 kHz AF. AF yields a much richer multi-path environment, however, it has a wavelength which is not comparable to 60 GHz radio waves, thus the receiver array design does not directly translate from the radio to the acoustic band. Path loss and channel impulse response measurements are performed and compared with 60 GHz transmission scenarios. The BER of un-coded single-carrier and multi-carrier techniques for both acoustic and radio channels is compared.

The rest of this chapter is organized as follows. In Section 6.2, the demonstrator setup is explained along with its various building blocks such as the transmitter, the receiver and the sound card. Section 6.3 presents some large scale and small scale fading parameters obtained by channel measurements at 10 kHz and 68 kHz. BER comparisons of the single-carrier and multi-carrier schemes for various audio and radio channels are given in Section 6.4.

6.2 Setup

The demonstrator setup and its simplified block diagram are shown in Figures 6.1 and 6.2, respectively. An ultrasonic/audio transducer is used as the transmission element with 8 microphones comprising the receiver array. The receive array is crucial for the design and implementation of beam forming algorithms, which is one of the main requirements for the SIGI Spot system. The transmitter and each element of the receiver array are connected to a personal computer (PC) via an ECHO Audiofire12 sound card [99]. A detailed explanation of each demonstrator element follows.

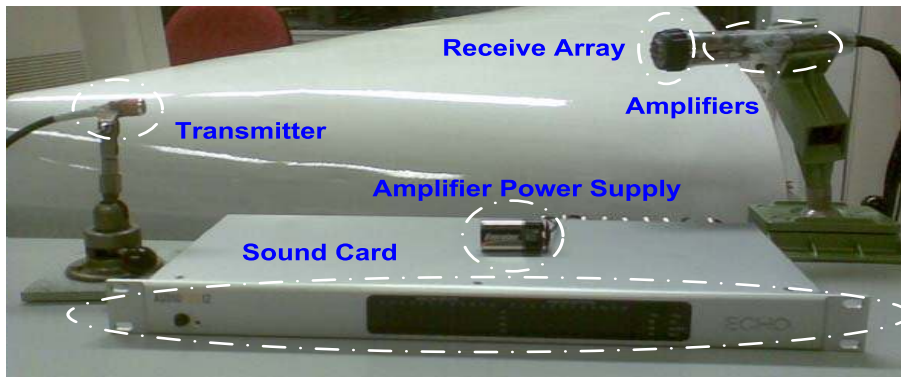


Figure 6.1: *Acoustic demonstrator setup.*

6.2.1 Sound card

The ECHO Audiofire12 is used as the interface between the transceivers and the PC. The properties of the ECHO AudioFire12 are summarized in Table 6.1. As shown in Figure 6.3, the frequency response of the sound card is not flat when used above frequencies of 20 kHz. In order to compensate for the sound card, we use a loop back cable, which is coupled with the transmit channel. This enables easy equalization of the sound card frequency response using the inverse filtering technique [100].

6.2.2 Transmitter

As mentioned above, two acoustic frequency bands have been investigated, i.e. 10 kHz and 68 kHz. For 10 kHz any standard speaker can be directly connected to

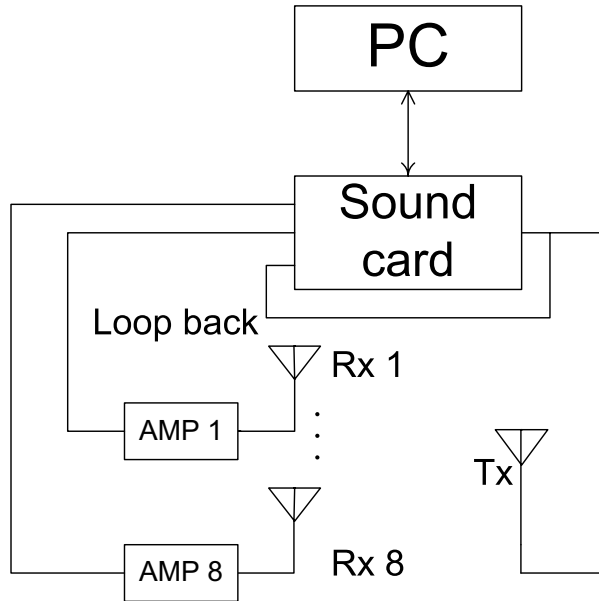


Figure 6.2: *Simplified system block diagram of the acoustic demonstrator.*

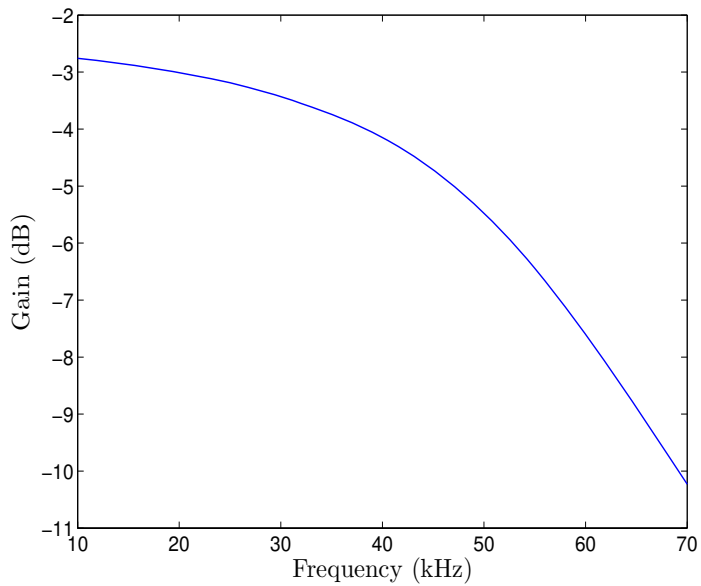


Figure 6.3: *Sound card frequency response.*

Maximum sampling frequency	192 kHz
I/O channels	12
Dynamic Range	113 dB

Table 6.1: *Soundcard properties.*

the output of the soundcard. The speaker at 10 kHz is expected to have a more or less omnidirectional transfer characteristic. For the UF, ready made off the shelf transmitters are not available. Therefore, a custom made 68 kHz ultrasonic air transducer (UAT) as shown in Figure 6.4 was ordered from American Piezo Corporation. The radiation pattern of the 68 kHz UAT is shown in Figure 6.5. UATs are primarily used for range finding applications and therefore exhibit a fairly narrow radiation pattern as can be seen from Figure 6.5.



Figure 6.4: *68 kHz UAT.*

6.2.3 Receiver Array

The receiver array as shown in Figure 6.6, comprises of 8 Panasonic WM-61A electret microphones each connected to a 40 dB amplifying stage. Each element is equally spaced within the circular array. The array radius R and consequently the inter-element spacing of the array is a crucial design parameter and should therefore be carefully chosen. The impact on the beam pattern by changing R of an 8 element circular array consisting of omnidirectional elements is shown in Figure 6.7. Symbols λ_a , λ_u and λ_r denote the wavelengths of the audio, ultrasonic and the radio bands, respectively. Element spacing is a trade-off between the width of the main lobe and the magnitude of the side-lobes as is evident from

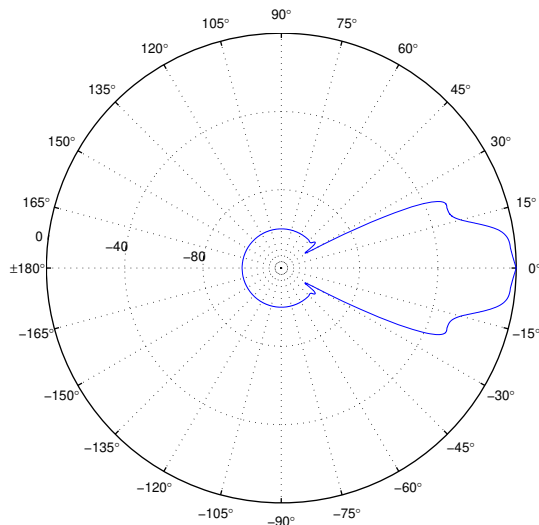


Figure 6.5: Radiation pattern of the 68 kHz UAT.

Figure 6.7. Increasing R^1 results in a narrower main lobe with higher side lobes; on the other hand decreasing R increases the main lobe spread. Considering all these factors a receiver array for 60 GHz is proposed in [101] with $R = 0.65\lambda_r$. Since $\lambda_u = \lambda_r = 5\text{mm}$, the receiver array for the UF band should be similar. In our design, the array radius is chosen to be $1.56\lambda_u$. This is the minimum achievable size with these microphones. The microphones no longer exhibit an omnidirectional behavior at UFs as can be seen from Figure 6.8, which gives the radiation pattern of the microphones at 40 kHz. At 68 kHz the microphones are expected to be even more directional. The directional nature of the microphones limit the scanning range of the array [102]. On the other hand if we consider the 10 kHz audio band, we get $R = 0.23\lambda_a$, which results in a very wide beam pattern and therefore beam forming will yield limited multi-path suppression. The array radius for the 10 kHz audio band thus needs to be increased to $0.65\lambda_a$.

6.3 Channel Measurements

Channel impulse response measurements were carried out under LOS scenarios at the EWI building of the Delft University of Technology. The walls and floor

¹ R can be changed by altering the array dimensions which in turns changes the coefficient of λ



Figure 6.6: Receiver array of 8 microphones.

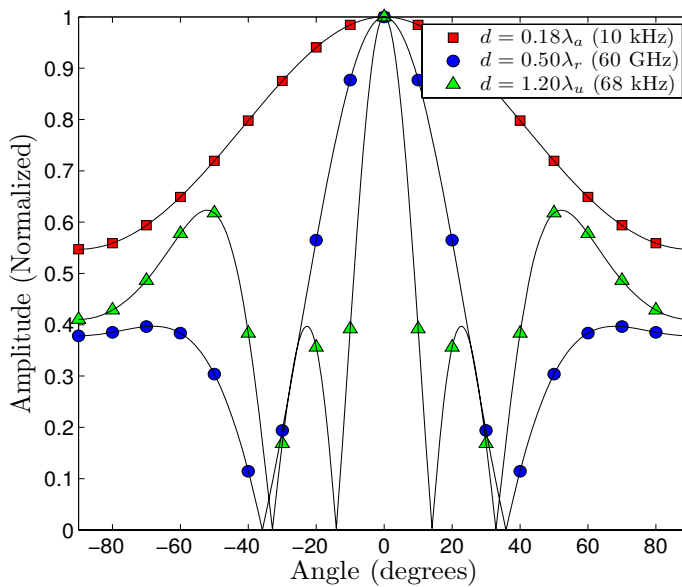


Figure 6.7: Impact of array radius on the beam pattern of the receiver array.

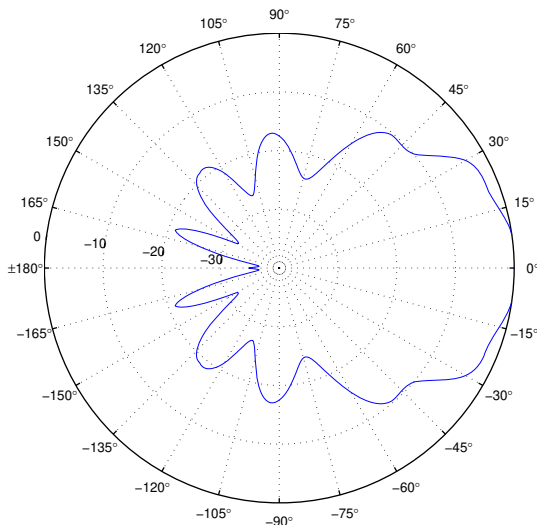


Figure 6.8: *Microphone beam pattern at 40 kHz.*

of the building are made of concrete. A typical office room with furniture and a corridor were used for the measurements. Channel measurements were performed for various distances between 50 cm and 5 m. The channel was sounded with a frequency modulated continuous wave (FMCW) signal commonly referred to as a chirp [103]. A total bandwidth of 10 kHz was used with the center frequencies kept at 10 kHz and 68 kHz. The inverse filtering technique was used for deconvolution to obtain the CIR. Prior to CIR extraction, the received signal was passed through a digital band pass filter (BPF) and windowed. The Hamming window was used which provides leakage suppression up to 40 dB.

Two measured CIRs and the corresponding PDPs for the 10 Hz and 68 kHz frequencies are shown in Figures 6.9 and 6.10, respectively. It is evident from Figures 6.9 and 6.10 that the 10 kHz band exhibits a larger number of multi-path components as compared to the 68 kHz band. The primary reason for this difference is the more omnidirectional nature of the loud speaker and microphone. Due to a high propagation loss at 68 kHz [104] and the directionality of the transceivers, no multi-path components within 35 dB of LOS path are received.

Channel measurements performed at the various frequencies show that the received power P_r is $P_r \propto d^{-n}$, where d denotes the distance between the transmitter and the receiver and n is an environment dependant factor commonly referred to

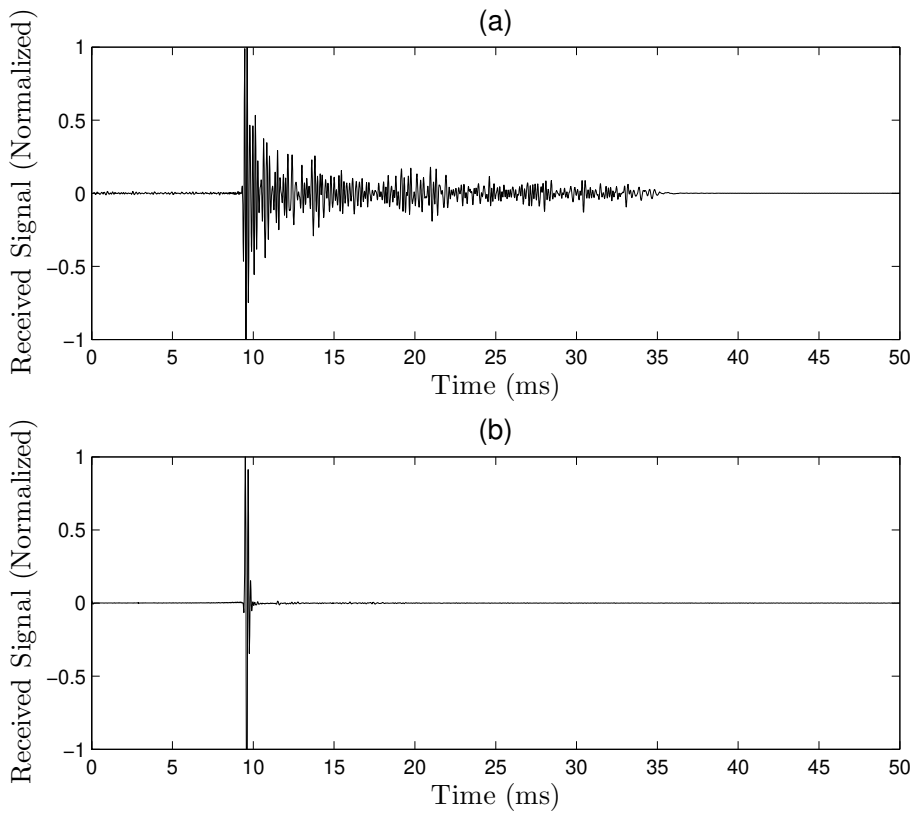


Figure 6.9: A comparison of measured CIR for (a) 10 kHz and (b) 68 kHz channels.

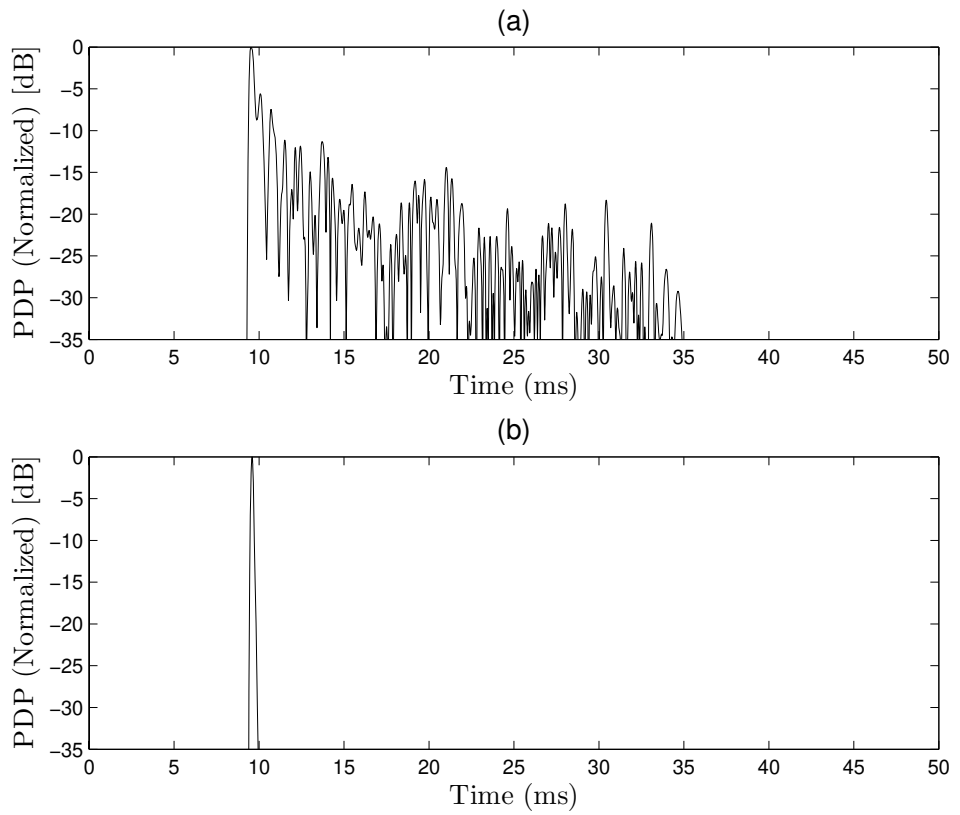


Figure 6.10: A comparison of measured PDP for (a) 10 kHz and (b) 68 kHz channels.

as the path-loss exponent [65]. Assuming that shadowing is log-normal, we can write the path loss at a distance d from the transmitter as

$$PL(d) = PL_0 - n10 \log_{10}(d/d_0) + X \text{ dB}, \quad (6.1)$$

where PL_0 denotes the path-loss at some reference distance d_0 and X is a Gaussian distributed random variable in the log domain with variance σ_X^2 . The path-loss exponent is obtained by linear curve fitting in the scatter plot of the measured path-loss versus distance in the logarithmic domain. Figures 6.11 shows the path-loss model with the measured data for 10 kHz and 68 kHz acoustic frequencies. It can be seen that the model fits well with the data. The path loss exponents found for the 10 kHz and 68 kHz bands are given in Table 6.2.

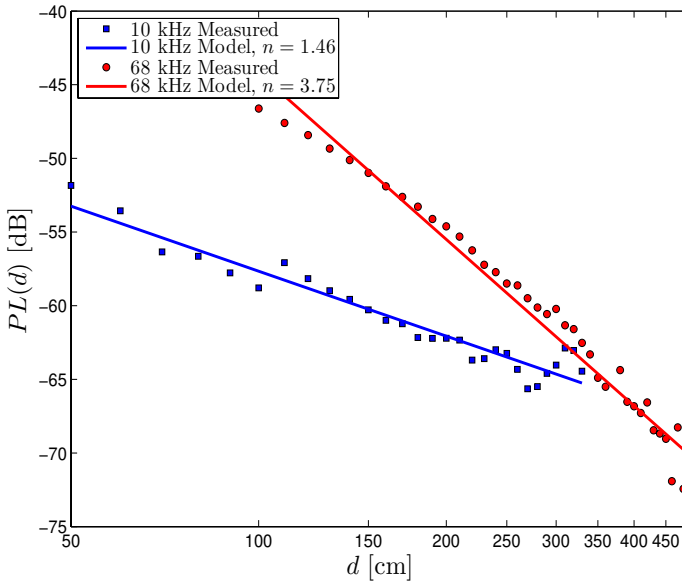


Figure 6.11: Path loss model for 10 kHz and 68 kHz acoustic frequencies.

The 10 kHz band exhibits a path-loss exponent which is much closer to the omnidirectional RF channels at 60 GHz. The values of various channel characteristics at 60 GHz, given in Table 6.2, are taken from [58] in which an exhaustive set of channel measurements for various scenarios and employing different antenna configurations have been reported. The acoustic propagation, unlike the RF propagation, is severely affected by atmospheric conditions within a room such as

Frequency	n	σ_X	τ_{rms}
10 kHz	1.46	1.25 dB	5.2 ms
68 kHz	3.75	1.33 dB	0.0 ms
60 GHz (omni.)	1.20	2.70 dB	7.3 ns
60 GHz (dir.)	2.00	0.60 dB	1.1 ns

Table 6.2: Various measured parameters of the radio and audio channels.

humidity, temperature and pressure [104]. It has been shown in [104] that the attenuation increases as the frequency is increased from 10 kHz to 68 kHz. Thus the large path-loss exponent at 68 kHz can be attributed to a higher atmospheric attenuation and due to the absence of multi-path components. The path-loss for various channels is shown in Figure 6.12. In this figure, the reference distance d_0 is taken to be 100 cm and PL_0 is assumed 0 dB. It can be seen that 10 kHz omnidirectional links are decaying much more rapidly than the 60 GHz omnidirectional links, while they decay more slowly as compared to the directional 60 GHz links. This can be attributed to the large number of multi-path components. The 68 kHz link on the other hand perform worse than all mentioned RF scenarios.

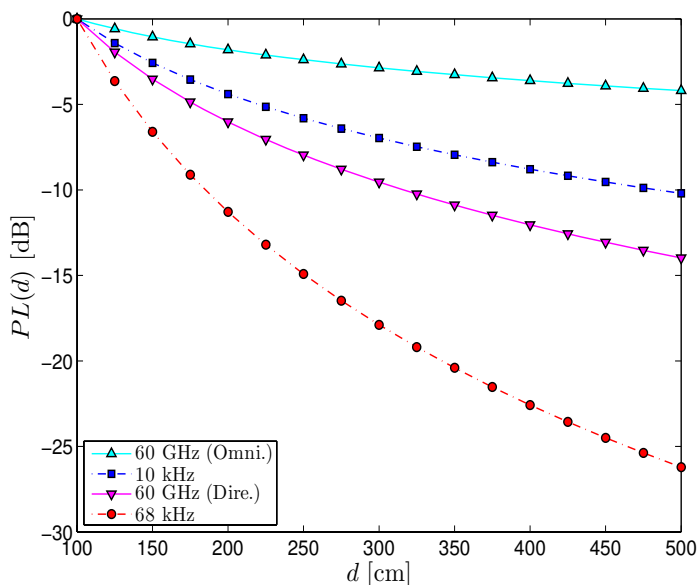


Figure 6.12: Path loss comparison for acoustic and radio frequencies.

6.4 BER Comparison

A performance comparison in terms of BER for various measured 10 kHz and 68 kHz channels along with that of the reference 60 GHz channel, is carried out in this section. We use a simplified 60 GHz LOS channel model, as presented in Section 2.2.2, for the performance comparison of various transmission techniques. A detailed description of these schemes can be found in Section 3.2. The system parameters for the single-carrier and multi-carrier schemes are summarized in Table 6.3. The BER for acoustic channels is evaluated by performing Monte Carlo simulations on the measured realizations that are stored on a computer. The multi-carrier and single-carrier schemes are implemented as shown in Figures 3.1 and 3.3, respectively. A total of 700 stored channel realizations were used for both 10 kHz and 68 kHz frequencies. The Monte Carlo simulation was run 1000 times per channel realization. During simulations it was assumed that the receiver has access to perfect channel state information.

Carrier frequency	60 GHz	10 kHz	68 kHz
Modulation scheme	QPSK	QPSK	QPSK
Channel bandwidth	1 GHz	10 kHz	10 kHz
Block length	1024	1024	1024
Cyclic prefix length	250	250	250

Table 6.3: *Multi-carrier and single-carrier system parameters.*

The BER results for multi-carrier and single-carrier schemes are given in Figures 6.13 and 6.14, respectively. In case of the 68 kHz channel, since there is only one direct LOS component, the only degradation in the system performance is due to the cyclic prefix insertion. The 10 kHz channel on the other hand experiences severe multi-path fading as is evident from Figure 6.10, therefore the BER is much worse in comparison with the RF and the 68 kHz band for both single-carrier and multi-carrier schemes. The 10 kHz band offers a richer multi-path environment which is more representative of the 60 GHz radio channels and is, therefore, a better option in comparison to the 68 kHz band for baseband algorithm design.

6.5 Conclusions

In this chapter, a low cost acoustic demonstrator for baseband algorithm design and verification was proposed. Various building blocks of the demonstrator

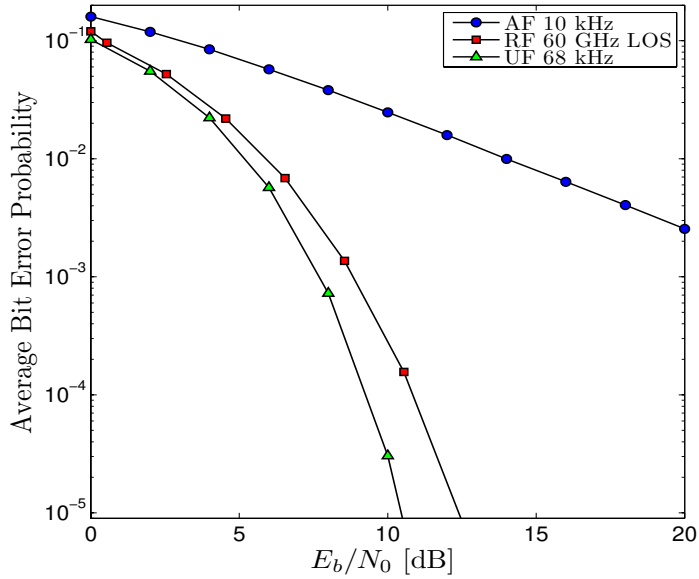


Figure 6.13: BER comparison of MC-BPSK for various acoustic and radio channels.

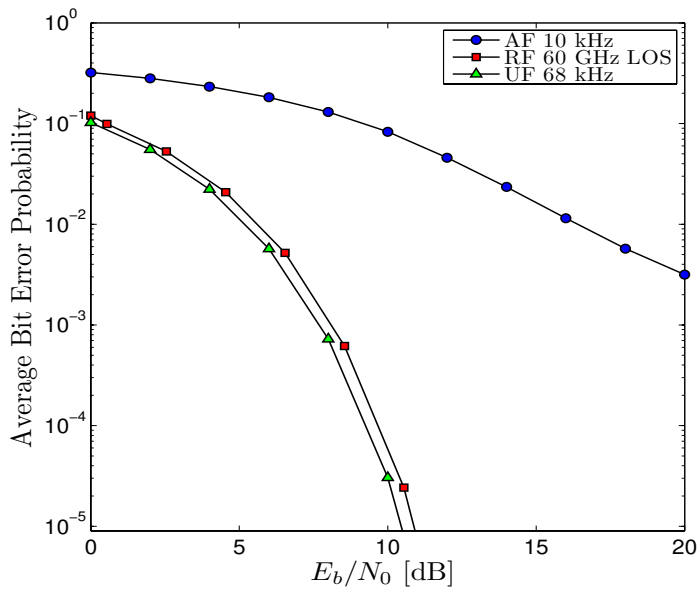


Figure 6.14: BER comparison of SC-BPSK for various acoustic and radio channels.

were explained. The demonstrator was used to perform channel measurements at two frequencies, i.e., 10 kHz and 68 kHz in LOS scenarios. A higher path-loss exponent in the 68 kHz band was observed as compared to the 10 kHz and the 60 GHz band. This can be attributed to the directional nature of the 68 kHz transducers and the high atmospheric absorption of 68 kHz waves. The BER using single-carrier and multi-carrier schemes was evaluated for measured acoustic channels and simulated radio channels. It was seen that 10 kHz channels due to severe multi-path conditions perform worse than both the 60 GHz and the 68 kHz links. The 10 kHz channels are more representative of millimeter-wave radio links due to a rich scattering environment, and therefore, the 10 kHz band is a good candidate for baseband algorithm design for 60 GHz channels. The design parameters of course will be different for acoustic and radio links and therefore should be appropriately adapted during the translation from the audio to the radio band.

Chapter 7

Conclusions and Recommendations

The main highlights of the thesis are summarized in this chapter. Major contributions are given and a number of unresolved issues as well as future research directions are presented.

The main challenges relating to the baseband implementation and design of a wireless communication system operating at a carrier frequency of 60 GHz were addressed in this dissertation. Firstly, various 60 GHz specific RF level circuit imperfections were identified. Based on a low implementation complexity requirement two candidate transmission schemes, namely single-carrier modulation with frequency domain equalization and orthogonal frequency division multiplexing based multi-carrier modulation, were considered. The performance of these schemes in the presence of RF level circuit imperfections was investigated. Low cost and complexity RF level diversity combining architectures with various sub-optimal diversity combining schemes were also considered. Diversity combining can be used effectively to combat fading, which is quite severe in the 60 GHz band. In the last part of the thesis a low cost acoustic demonstrator that can be used for the design and implementation of base band algorithms, was proposed. The demonstrator shifts the focus from tedious high data rate 60 GHz implementation issues to algorithm design, while providing a transmission environment comparable to 60 GHz. The algorithm design after testing can easily be translated to 60 GHz after appropriate scaling. A chapter wise summary of the main results and conclusions along with some unsolved problems and interesting future research prospects is presented below.

7.1 Single-Carrier vs. Multi-Carrier Transmission

Single carrier schemes, due to their lower peak to average power ratio, are much more robust to the effect of RF circuit imperfections as compared to their multi-carrier counter part. Since a modulated base band symbol is transmitted over the entire channel bandwidth with a single-carrier scheme, it efficiently utilizes the multi-path diversity, and therefore, exhibits superior performance to multi-carrier schemes. After a detailed comparison of single-carrier and multi-carrier based transceivers operating in the 60 GHz band, the following major conclusions can be drawn.

<p>The single-carrier and multi-carrier based transceivers require the same computational complexity, however, in case of the single-carrier scheme this complexity is concentrated at the receiver, whereas for a multi-carrier scheme both the transmitter and the receiver have comparable computational complexities.</p>

The choice of single-carrier or multi-carrier modulation is based on implementation complexity. It is therefore dependent on the application. In case of broadcast systems in which there is one transmitter and multiple receivers, single-carrier is not an attractive alternative. For symmetric networks, in which each node must act as a transceiver, it does not matter from a complexity perspective, whether single-carrier or multi-carrier is chosen.

The single-carrier scheme requires a lower resolution for both DAC and ADC.

A major source of power consumption in any communication system is the ADC, which is related to its number of bits and the sampling frequency. This means that the larger the number of the bits and higher the sampling frequency, the greater is the power consumption. The single-carrier scheme requires a lower number of bits for the DAC/ADC as compared to the multi-carrier scheme, therefore, single-carrier based transceivers are more efficient in terms of power consumption, i.e., less DAC/ADC power is required for the same BER performance.

The multi-carrier scheme is more robust to phase noise impairments as compared to the single-carrier scheme.

Due to its superior resilience to phase noise effects, multi-carrier modulation allows the use of low cost oscillators.

A single-carrier scheme outperforms the multi-carrier scheme in the presence of I/Q imbalance.

I/Q imbalance of 60 GHz devices was found to be the worst impairment especially for 8PSK constellations for both single-carrier and multi-carrier schemes. I/Q imbalance is the most critical impairment as it results in a high degradation in system performance especially for 8PSK constellations.

It is shown that the SNR degradation in the single-carrier scheme is marginal even when the the HPA is operated at a low IBO. A multi-carrier scheme requires the HPA to be operated at a high IBO, thus making it inefficient in terms of power consumption.

The power amplifier at the transmitter when operated at a high IBO makes the transceiver design inefficient in terms of power consumption. These investigations were performed only for PSK schemes and the difference between the single-carrier and multi-carrier schemes is expected to be lower for QAM constellations.

It is seen that both the single-carrier and multi-carrier scheme, while having the same implementation complexity, react differently to RF impairments. The single-carrier scheme with PSK modulation is found to be more tolerant to RF impairments, such as amplifier nonlinearities, limited ADC/DAC resolution and I/Q imbalance, while multi-carrier modulation is more robust against phase noise. A qualitative comparison of the single-carrier and multi-carrier systems using QPSK and 8PSK constellations is summarized in Table 7.2. The circuit parameters used are summarized in Table 7.1¹. In Table 7.2, + denotes a low SNR degradation, 0 a moderate SNR degradation and $-N_{\text{ADC}}$ a high degradation in SNR. The

Mod.	N_{DAC}	K	ϵ	ϕ	IBO_{HPA}	N_{ADC}
QPSK	3	-20 dBC	1 dB	4°	6 dB	6
8PSK	4	-24 dBC	1 dB	4°	10 dB	8

Table 7.1: Multi-carrier and single-carrier circuit parameters for qualitative comparison

impact of RF imperfections for coded scenarios along with improved detection schemes should be investigated in future work. An interesting observation that can be made is that constellation rotation can be effectively used to counter the impact of some RF imperfections, such as I/Q imbalance and amplifier nonlinearity. This would, therefore, result in an improved system performance without

¹ N_{DAC} – Numbe of bits of DAC, K – Total integrated double sided PSD of phase noise, ϵ – Amplitude mismatch due to I/Q imbalance, ϕ – Phase mismatch due to I/Q imbalance, IBO_{HPA} – Input back-off for high power amplifier, N_{ADC} –Number of bits of ADC

Mod.	Transc.	N_{DAC}	K	I/Q	IBO _{HPA}	N_{ADC}
QPSK (BER= 1×10^{-4})	Multi-carrier	–	+	0	–	–
	Single-carrier	+	0	0	+	+
8PSK (BER= 1×10^{-4})	Multi-carrier	–	+	–	–	0
	Multiple-carrier	+	0	–	+	+

Table 7.2: *Multiple-carrier and single-carrier qualitative comparison*

any increase in system complexity. Detailed analysis in this direction along with coding can be a useful future investigation.

7.2 ADC Resolution

A major chunk of the power consumption of a communication system is consumed by the ADC. The power consumption of an ADC is directly proportional to the product of its sampling frequency and $2^{N_{ADC}}$, where N_{ADC} denotes the number of bits of the ADC. Therefore, the number of bits of an ADC should be kept as small as possible if power consumption is to be kept small. Novel closed form analytic expressions for the bit error probability of single-carrier schemes, under generalized fading and non-fading scenarios, as a function of the number of ADC bits, the received SNR and the modulation level have been derived. Based on this analysis we can draw the following conclusions.

The required number of bits depend on the channel fading conditions and modulation level M . Therefore, the number of ADC bits should be chosen considering the transmission scenario in which the system is required to operate and the spectral efficiency of the system.

In this work, only the impact of quantization noise was considered. Certain other aspects of the ADC such as offset and gain error and noise due to the sample-and-hold circuit, were ignored. Considering these impairments along with quantization can be a natural extension to this work.

7.3 RF Level Diversity Combining

Conventional antenna diversity combining architectures, which utilize two ADCs and two mixers per antenna element, are cost and power inefficient. In this thesis, we explored the possibility of using RF level diversity combining. In RF level diversity combining the channel phase and amplitude compensation is shifted from the digital domain to the RF domain. This significantly reduces hardware cost and complexity, however, at the cost of sub-optimum system performance. The main highlights and conclusions of this investigation can be stated as follows.

7.3.1 Equal Gain Combining

The performance and viability of using EGC with RF level diversity combining was investigated. Two sets of novel analytical expressions for the system performance evaluation in terms of bit error probability of BPSK signalling were derived. The first expression can be used to accurately predict the system performance over the entire SNR range. An approximation can be used to evaluate the system performance at high (more practical) SNRs. These expressions were used to compare the performance with non coherent and partially coherent schemes, i.e., BFSK and DBPSK. Based on this analysis the following conclusions can be drawn.

The required number of quantization levels L to achieve near ideal performance for an EGC system employing RF level diversity combining is dependent on the number of receiver antennas.

A comparison with non coherent and partially coherent schemes, i.e., BFSK and DBPSK shows that for only 3 level phase compensation BPSK exhibits superior performance to both BFSK and DBPSK, irrespective of the number of antennas used at the receiver.

A diversity order analysis was carried out and surprisingly, the diversity order was found to be independent of the phase quantization level L .

7.3.2 Selection and Switched Combining

Novel analytical expressions for the SER evaluation of MPSK modulation with SC and SWC over Rayleigh fading channels as a function of the received SNR, the phase quantization level L and the modulation level M , were derived. These expressions can be used to evaluate the system performance in terms of average probability of error over the whole SNR range. The following conclusions can be drawn for this analysis.

The number of quantization levels L required to achieve near ideal performance are dependent on: the number of the receive antennas N_R and the modulation level M . One can make a tradeoff between the phase quantization levels L , N_R and M .

Combining Scheme	EGC	SC	SWC
L	4	6	6

Table 7.3: Number of quantization levels L , required to achieve performance close to the conventional case.

The number of quantization levels L required to achieve performance within 0.5 dB of the optimum conventional diversity combiner for BPSK signals in Rayleigh fading with 2 receiver antennas and a SNR of 10 dB are given in Table 7.3.

The system performance when compared with non-coherent BFSK and DBPSK was found outperform non-coherent schemes certain levels of L for all the three considered schemes, i.e., EGC, SC and SWC .

Table 7.4 summarizes the number of levels L required to outperform non-coherent schemes for BPSK signals under Rayleigh fading channels.

Combining Scheme	EGC	SC	SWC
L	3	4	3

Table 7.4: Required number of quantization levels L , to outperform non-coherent diversity combining.

In this work, we limited our analysis to Rayleigh fading channels. Extension to more generalized Nakagami- m fading could be a useful future investigation. Furthermore, it is good to mention here that for Rayleigh fading channels the channel phases are uniformly distributed which implies that the uniform quantization is the best possible solution. On the other hand, as explained in Chapter 2, the channel phases for Nakagami- m fading channels are not uniformly distributed, which means that we can optimize the quantized design using the error probability expression as a cost function.

7.4 Acoustic Demonstrator

The development of a complete demonstrator at 60 GHz is cumbersome due to high hardware costs involved. Furthermore, the algorithm implementation at 60 GHz is challenging due to high sampling rate requirements. To shift the focus from implementation to algorithm design we proposed a low cost demonstrator based on acoustic signal. This system is based on a synchronous 12 input 12 output audio sound card with a maximum sampling frequency of 192 kHz. Channel measurements were carried out at two frequencies, i.e., 10 kHz and 68 kHz in LOS scenarios using the newly developed setup. Based on this system we carried out various system level measurements and the conclusions are as follows.

The 68 kHz band has a high path-loss exponent as compared to the 10 kHz and the RF band. It was shown that 10 kHz channels, due to severe multi-path conditions, perform worse than both the RF and the 68 kHz links.

The 10 kHz channels are more representative of millimeter-wave radio channels due to a richer scattering. Although 10 kHz channels, even in LOS scenarios suffer more severe ISI as compared to LOS 60 GHz channels, they are a good candidate for baseband algorithm design as opposed to the 68 kHz links which do not suffer any ISI.

The design parameters will be different for 10 kHz and RF bands, and there-

fore, should be appropriately adapted during the translation from the audio to the radio band. A qualitative comparison of different channel parameters and BER performance measures for acoustic and radio transmission bands is summarized in Table 7.5. In Table 7.5, + denotes low, 0 denotes moderate and – denotes high, for the mentioned quantities.

Carrier Frequency	n	τ_{rms}	BER
10 kHz	+	–	–
68 kHz	+	+	+
60 GHz	+	+	+

Table 7.5: *A qualitative comparison of different channel parameters and BER for acoustic and radio frequencies.*

Appendix A

Integral Derivation

In this appendix, we present the solution of the integral

$$I(\theta) = \int \frac{1}{\sin^2(\theta)} e^{-\frac{K}{\sin^2(\theta)}} d\theta, \quad (\text{A.1})$$

where K represents an arbitrary constant. Using the substitution $w = \csc^2(\theta) - 1$, (A.1) can be written as

$$I(\theta) = -\frac{1}{2} \int \frac{1}{\sqrt{w}} e^{-K-Kw} dw. \quad (\text{A.2})$$

Using [105], we can write the integral given in (A.2) as

$$I(\theta) = -\frac{e^{-K} \sqrt{\pi} \operatorname{erfi}\left(j\sqrt{K}\sqrt{w}\right)}{2j\sqrt{K}}, \quad (\text{A.3})$$

where $\operatorname{erfi}(\cdot)$ denotes the imaginary error function [106] and $j = \sqrt{-1}$. Using the relation $\operatorname{erfi}(jx) = j\operatorname{erf}(x)$ and substituting $w = \csc^2(\theta) - 1$ we get

$$I(\theta) = -\frac{\sqrt{\pi} e^{-K}}{2\sqrt{K}} \operatorname{erf}\left(\sqrt{K} \cot(\theta)\right). \quad (\text{A.4})$$

Appendix B

An Alternative CHF for EGC

In an alternative approach to the one outlined in the previous section, the PDF of y_i is computed as

$$p_{y_i}(y_i) = \mathcal{M}^{-1}(\mathcal{M}_{h_i}(\omega) \mathcal{M}_{z_i}(\omega)), \quad (\text{B.19})$$

where

$$\mathcal{M}_Z(\omega) = \int_0^\infty z^{\omega-1} p_Z(z) dz \quad (\text{B.20})$$

and

$$\begin{aligned} \mathcal{M}_z^{-1}(\mathcal{M}_z(\omega)) &= p_z(z) \\ &= \frac{1}{2\pi j} \int_{c-j\infty}^{c+j\infty} x^{-\omega} \mathcal{M}_z(\omega) d\omega \end{aligned} \quad (\text{B.21})$$

represent the Mellin and the inverse Mellin transforms (MT and IMT) of the PDF, respectively. It can be shown that the MT of h_i and z_i are

$$\mathcal{M}_{h_i}(\omega) = \left(\frac{1}{\Omega_i}\right)^{\frac{1-\omega}{2}} \Gamma\left(\frac{1+\omega}{2}\right), \quad (\text{B.22})$$

and

$$\mathcal{M}_{z_i}(\omega) = \frac{L}{2\sqrt{\pi}} \frac{\Gamma\left(\frac{\omega}{2}\right)}{\Gamma\left(\frac{1+\omega}{2}\right)} - \frac{L}{2\pi} \sum_{k=0}^{N_a} \frac{\left(\frac{1}{2}\right)_k \Gamma\left(k + \frac{\omega}{2}\right) L_c^{\omega+2k}}{\Gamma(k+1) \Gamma\left(k+1 + \frac{\omega}{2}\right)}, \quad (\text{B.23})$$

respectively, where $\Gamma(\cdot)$ denotes the Gamma function [107, p. 1] and $N_a = 20$ is seen to be a suitable value for series convergence. Substituting (B.22) and (B.23) in (B.19), we get

$$p_{y_i}(y_i) = \sqrt{\frac{L^2}{\pi\Omega_i}} e^{-\frac{y_i^2}{\Omega_i}} + \sqrt{\frac{L^2}{\pi^2\Omega_i}} \sum_{k=0}^{N_a} G_{1,2}^{2,0} \left[\begin{matrix} \frac{y_i^2}{L_c\Omega_i} \\ \frac{y_i^2}{L_c\Omega_i} \end{matrix} \middle| \begin{matrix} k+1 \\ k, \frac{1}{2} \end{matrix} \right] \frac{L_c^{2k} \Gamma(k + \frac{1}{2})}{\Gamma(k+1)} \quad (\text{B.24})$$

where $G_{p,q}^{m,n} \left[\begin{matrix} \cdot \\ \cdot, \dots, \cdot \end{matrix} \middle| \begin{matrix} \cdot, \dots, \cdot \\ \cdot, \dots, \cdot \end{matrix} \right]$ denotes the MeijerG function [107, p. 207]. Representing y_i in terms of v_i , we get

$$p_{v_i}(v_i) = \sqrt{\frac{L^2}{\pi\bar{\gamma}_i}} e^{-\frac{v_i^2}{\bar{\gamma}_i}} + \sqrt{\frac{L^2}{\pi^2\bar{\gamma}_i}} \sum_{k=0}^{N_a} G_{1,2}^{2,0} \left[\begin{matrix} \frac{v_i^2}{L_c\bar{\gamma}_i} \\ \frac{v_i^2}{L_c\bar{\gamma}_i} \end{matrix} \middle| \begin{matrix} k+1 \\ k, \frac{1}{2} \end{matrix} \right] \frac{L_c^{2k} \Gamma(k + \frac{1}{2})}{\Gamma(k+1)} \quad (\text{B.25})$$

Using the relation

$$L_{v_i}(\omega) = \int_0^\infty p_{v_i}(v_i) e^{-\omega v_i} dv_i, \quad (\text{B.26})$$

we can write the Laplace transform of (B.25) as

$$L_{v_i}(\omega) = \frac{L}{2} e^{\frac{\omega^2 \bar{\gamma}_i}{4}} - L \sqrt{\frac{\omega \bar{\gamma}_i}{4\pi}} {}_2F_2 \left(1, \frac{3}{2}; \frac{3}{2}, \frac{3}{2}; \frac{\omega^2 \bar{\gamma}_i}{4} \right) - \frac{L}{2\pi} \sum_{k=0}^{N_a} {}_2F_2 \left(\frac{1}{2} + k, 1; \frac{1}{2}, \frac{3}{2} + k; \frac{\omega^2 L_c^2}{4} \right) \frac{\Gamma(\frac{1}{2} + k) (\frac{1}{2})_k}{\Gamma(\frac{3}{2} + k) (1)_k} L_c^{2k+1} + \frac{L\omega}{4} \sqrt{\frac{\bar{\gamma}_i}{\pi}} \sum_{k=0}^{N_a} {}_2F_2 \left(1 + k, \frac{3}{2}; \frac{3}{2}, 2 + k; \frac{\omega^2 \bar{\gamma}_i L_c^2}{4} \right) \frac{(\frac{1}{2})_k}{(2)_k} L_c^{2k+2} \quad (\text{B.27})$$

where ${}_pF_q(\cdot; \cdot; \cdot)$ denotes the generalized hypergeometric function [107, p. 182]. We can obtain the CHF from (B.27) as

$$\phi_{v_i}(\omega) = \lim_{\sigma \rightarrow 0} L_{v_i}(\sigma - j\omega) \quad (\text{B.28})$$

Thus (B.28) together with (5.15) can be used to compute the BER. It is good to note here that (5.22) and (B.24), (5.27) and (B.28) are alternative but numerically equivalent representations.

Error Probability Derivations for Diversity Combining

Various derivations used to obtain results in Chapter 5 are outline in this appendix.

C.1 BER of EGC at High SNR

The BER ay high SNR is given as (5.30)

$$p_{v_i}(v) = \frac{2Lv}{\pi\bar{\gamma}} \tan\left(\frac{\pi}{L}\right). \quad (\text{C.1})$$

The Laplace Transform (LT) of $p_{v_i}(v)$ is given as

$$L_{v_i}(\omega) = \frac{2L}{\pi\bar{\gamma}\omega^2} \tan\left(\frac{\pi}{L}\right). \quad (\text{C.2})$$

The LT of $p_w(w)$ is then given as

$$L_w(\omega) = \left(\frac{2L}{\pi\bar{\gamma}\omega^2} \tan\left(\frac{\pi}{L}\right)\right)^{N_R}. \quad (\text{C.3})$$

Taking the inverse LT we can write the PDF of w as

$$p_w(w) = \left(\frac{2L}{\pi\bar{\gamma}} \tan\left(\frac{\pi}{L}\right) \right)^{N_R} \frac{w^{2N_R-1}}{\Gamma(2N_R)}, \quad (\text{C.4})$$

where $\Gamma(\cdot)$ denotes the Gamma function [107, p. 1]. Using (5.11) we can formulate the BER at high SNR as

$$P_s = \frac{1}{2\Gamma(2N_R)} \left(\frac{2L}{\pi\bar{\gamma}} \tan\left(\frac{\pi}{L}\right) \right)^{N_R} \int_0^\infty \text{erfc}\left(\frac{w}{\sqrt{N_R}}\right) w^{2N_R-1} dw, \quad (\text{C.5})$$

where we have used

$$P(\varepsilon|w) = \frac{1}{2} \text{erfc}\left(\frac{w}{\sqrt{N_R}}\right). \quad (\text{C.6})$$

Solving the above integral yields

$$P_s = \frac{1}{2\Gamma(1+N_R)} \left(\frac{N_R L}{2\pi\bar{\gamma}} \tan\left(\frac{\pi}{L}\right) \right)^{N_R}. \quad (\text{C.7})$$

C.2 Error Probability Derivation for MPSK Signals

In this appendix we derive the error probability for the case when phase noise $\phi > \pi/M$, i.e., the phase noise takes the symbol out of its decision region. A simplified geometry for this case is depicted in Figure C.1. This case can be further divide into two error events whose error probability can be separately computed. The first case is for $\phi < \pi/M$, i.e., phase noise does not take the symbol out of its decision region. The second case is for $\phi > \pi/M$. In this case it is easier to first compute the probability of correct decision and then subtract it from 1 to find the error probability. The total conditional error probability is thus given as

$$P(E; \alpha, \phi) = P(E_1; \alpha, \phi) + P(E_2; \alpha, \phi). \quad (\text{C.8})$$

where $P(E_1; \alpha, \phi)$ and $P(E_2; \alpha, \phi)$ correspond to the error probabilities of the first and the second error events, respectively. The error probability of the first

event follows directly from [96] and can be written as

$$\begin{aligned}
 P(E_1; \alpha, \phi) &= \frac{1}{2\pi} \int_0^{\frac{\pi}{M}(M-1)} e^{-\frac{\alpha^2 E_s \sin^2(\frac{\pi}{M} + \phi)}{N_0 \sin^2(\Phi)}} d\Phi + \\
 &\quad \frac{1}{2\pi} \int_0^{\frac{\pi}{M}(M-1) + \phi} e^{-\frac{\alpha^2 E_s \sin^2(\frac{\pi}{M} - \phi)}{N_0 \sin^2(\Phi)^2}} d\Phi. \quad (C.9)
 \end{aligned}$$

By inspecting the geometry of Figure C.1 and after some simple trigonometric manipulation we can write the distances R_1 and R_2 as

$$R_1 = \frac{\alpha \sqrt{E_s} \sin\left(\phi - \frac{\pi}{M}\right)}{\sin\left(\phi - \frac{\pi}{M} + \theta\right)}, \quad (C.10)$$

and

$$R_2 = \frac{\alpha \sqrt{E_s} \sin\left(\phi + \frac{\pi}{M}\right)}{\sin\left(\phi + \frac{\pi}{M} + \theta\right)}, \quad (C.11)$$

where α denotes the amplitude error. Using the polar form of the Gaussian PDF, i.e.,

$$p_{r,\theta}(r, \theta) = \frac{r}{\pi N_0} e^{-\frac{r^2}{N_0}} \quad (C.12)$$

we can write the probability of a correct symbol detection denoted by $P(C; \alpha, \phi)$ as

$$P(C; \alpha, \phi) = \frac{1}{2\pi} \int_0^{\pi - \phi - \frac{\pi}{M}} e^{-\frac{R_1^2}{N_0}} - e^{-\frac{R_2^2}{N_0}} d\theta + \frac{1}{2\pi} \int_{\pi - \phi - \frac{\pi}{M}}^{\pi - \phi + \frac{\pi}{M}} e^{-\frac{R_1^2}{N_0}} d\theta \quad (C.13)$$

The probability of an erroneous decision for the second error event can thus be computed as

$$P(E_2; \alpha, \phi) = 1 - P(C; \alpha, \phi). \quad (C.14)$$

Substituting (C.10), (C.11) and (C.13) in (C.14) we can write the error probability as

$$\begin{aligned}
 P(E_2; \alpha, \phi) &= 1 - \frac{1}{2\pi} \int_0^{\pi - \phi - \frac{\pi}{M}} e^{-\frac{\alpha^2 E_s}{N_0} \frac{\sin^2\left(\phi - \frac{\pi}{M}\right)}{\sin^2\left(\phi - \frac{\pi}{M} + \theta\right)}} - e^{-\frac{\alpha^2 E_s}{N_0} \frac{\sin^2\left(\phi + \frac{\pi}{M}\right)}{\sin^2\left(\phi + \frac{\pi}{M} + \theta\right)}} d\theta - \\
 &\quad \frac{1}{2\pi} \int_{\pi - \phi - \frac{\pi}{M}}^{\pi - \phi + \frac{\pi}{M}} e^{-\frac{\alpha^2 E_s}{N_0} \frac{\sin^2\left(\phi + \frac{\pi}{M}\right)}{\sin^2\left(\phi + \frac{\pi}{M} + \theta\right)}} d\theta. \quad (C.15)
 \end{aligned}$$

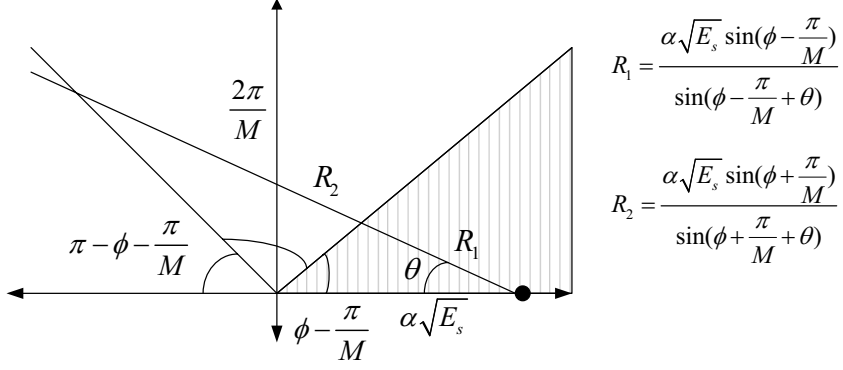


Figure C.1: Geometry for SER calculation.

The total error probability can thus be written as

$$\begin{aligned}
 P(E; \alpha, \phi) = & 1 - \frac{1}{2\pi} \int_0^{\pi - \phi - \frac{\pi}{M}} e^{-\frac{\alpha^2 E_s}{N_0} \frac{\sin^2(\phi - \frac{\pi}{M})}{\sin^2(\phi - \frac{\pi}{M} + \theta)}} - e^{-\frac{\alpha^2 E_s}{N_0} \frac{\sin^2(\phi + \frac{\pi}{M})}{\sin^2(\phi + \frac{\pi}{M} + \theta)}} d\theta - \\
 & \frac{1}{2\pi} \int_{\pi - \phi - \frac{\pi}{M}}^{\pi - \phi + \frac{\pi}{M}} e^{-\frac{\alpha^2 E_s}{N_0} \frac{\sin^2(\phi + \frac{\pi}{M})}{\sin^2(\phi + \frac{\pi}{M} + \theta)}} d\theta + \\
 & \frac{1}{2\pi} \int_0^{\frac{\pi}{M}(M-1)} e^{-\frac{\alpha^2 E_s \sin^2(\frac{\pi}{M} + \phi)}{N_0 \sin^2(\Phi)}} d\Phi + \\
 & \frac{1}{2\pi} \int_0^{\frac{\pi}{M}(M-1) + \phi} e^{-\frac{\alpha^2 E_s \sin^2(\frac{\pi}{M} - \phi)}{N_0 \sin^2(\Phi)^2}} d\Phi, \quad \phi > \frac{\pi}{M}. \quad (C.16)
 \end{aligned}$$

The error probability derivation for selection combining and switched combining was outlined in Chapter 5. For ease of presentation, the error probabilities were represented as combinations of various functions and terms, which are given in appendices C.3 - C.6.

C.3 Error Probability terms for Selection Combining

The functions and terms used for evaluating the SER given in (5.62) are

$$I_1 = \int_0^{\frac{\pi}{M}} \sum_{k=0}^{N_R-1} \frac{\binom{N_R-1}{k} (-1)^k}{1+k} \mathcal{G}_1 \left(1, \mathcal{H}_2(1, 1, 0, \cdot), 0, 1, \mathcal{H}_2(-1, 1, 0, \cdot), \right. \\ \left. 1, \mathcal{H}_3(-1, -1, 0, 1, 1, 0, k, \bar{\gamma}), 1, 1, \mathcal{H}_2(1, 1, 0, \cdot), 0 \right) d\phi, \quad (\text{C.17})$$

$$I_2 = \int_0^{\frac{\pi}{M}} \sum_{k=0}^{N_R-1} \frac{\binom{N_R-1}{k} (-1)^k}{1+k} \mathcal{G}_1 \left(1, \mathcal{H}_2(1, 1, 1, \cdot), 0, 1, \mathcal{H}_2(0, 1, 0, \cdot), 1, \right. \\ \left. \mathcal{H}_2(0, -1, 0, \cdot), 1, 1, \mathcal{H}_2(1, 1, 1, \cdot), 0 \right) d\phi, \quad (\text{C.18})$$

$$I_3 = \int_{\frac{\pi}{M}}^{\frac{\pi}{L}} \sum_{k=0}^{N_R-1} \binom{N_R-1}{k} (-1)^k \mathcal{G}_1 \left(\mathcal{H}_1(k, \bar{\gamma}), \mathcal{H}_2(1, 1, 1, \cdot), 1, 1, \right. \\ \left. \mathcal{H}_2(0, 1, -1, 1, 1, 0, k, \bar{\gamma}), -1, \mathcal{H}_3(0, -1, 1, 1, 1, 0, k, \bar{\gamma}), 1, \right. \\ \left. \mathcal{H}_2(0, -1, -1, \cdot), \frac{2\pi}{M}, \mathcal{H}_2(0, -1, 0, \cdot) \right) d\phi, \quad (\text{C.19})$$

$$I_4 = \int_{\frac{\pi}{M}}^{\frac{\pi}{L}} \sum_{k=0}^{N_R-1} \binom{N_R-1}{k} (-1)^k \mathcal{G}_1 \left(\mathcal{H}_1(k, \bar{\gamma}), \mathcal{H}_2(1, 1, 1, \cdot), 1, 1, \right. \\ \left. \mathcal{H}_2(0, 1, 0, \cdot), 1, \mathcal{H}_3(0, -1, 1, 1, 1, 0, k, \bar{\gamma}), 1, \right. \\ \left. \mathcal{H}_3(0, -1, 0, 1, 1, 0, k, \bar{\gamma}), \pi, \mathcal{H}_2(0, 0, 0, \cdot) \right) d\phi, \quad (\text{C.20})$$

$$I_5 = \int_0^{\frac{\pi}{M}} \sum_{k=0}^{N_R-1} \binom{N_R-1}{k} (-1)^k \mathcal{G}_1 \left(\mathcal{H}_1(k, \bar{\gamma}), \frac{2\pi}{M}, 1, \pi, \mathcal{H}_3(0, 1, 1, 1, 1, 0, k, \bar{\gamma}), 1, \right. \\ \left. 1, -1, \mathcal{H}_3(0, -1, 1, 1, 1, 0, k, \bar{\gamma}), 1, \frac{2\pi}{M} \right) d\phi, \quad (\text{C.21})$$

$$I_6 = \int_0^{\frac{\pi}{L}} \sum_{k=0}^{N_R-1} \frac{\binom{N_R-1}{k} (-1)^k}{1+k} \mathcal{G}_1 \left(1, \mathcal{H}_2(1, 1, 0), 0, 1, \mathcal{H}_3(-1, 1, 0, 1, 1, 0, k, \bar{\gamma}), 1, \right. \\ \left. \mathcal{H}_3(-1, -1, 0, 1, 1, 0, k, \bar{\gamma}), 1, 1, \mathcal{H}_2(1, 1, 0), 0 \right) d\phi, \quad (\text{C.22})$$

$$I_7 = \int_0^{\frac{\pi}{L}} \sum_{k=0}^{N_R-1} \frac{\binom{N_R-1}{k} (-1)^k}{1+k} \mathcal{G}_1 \left(1, \mathcal{H}_2(1, 1, 1), 0, 1, \mathcal{H}_3(0, 1, 0, 1, 1, 0, k, \bar{\gamma}), 1, \right. \\ \left. \mathcal{H}_3(0, -1, 0, 1, 1, 0, k, \bar{\gamma}), 1, 1, \mathcal{H}_2(1, 1, 1), 0 \right) d\phi, \quad (\text{C.23})$$

$$\mathcal{H}_1(\bar{\gamma}, k) = \frac{\bar{\gamma}}{k+1}, \quad (\text{C.24})$$

$$\mathcal{H}_2(n, p, q) = n\pi + (-1)^p \frac{\pi}{M} + (-1)^q \phi, \quad (\text{C.25})$$

$$\mathcal{H}_3(n, o, p, q, r, t, k, \bar{\gamma}) = (-1)^t \left(\sqrt{\frac{\bar{\gamma}^q \sin \left((-1)^p \frac{\pi}{M} + (-1)^n \phi \right)^2}{(1+k)^r + \bar{\gamma}^q \sin \left((-1)^p \frac{\pi}{M} + (-1)^n \phi \right)^2}} \right)^o, \quad (\text{C.26})$$

and

$$\mathcal{G}_1(F, K, G_1, G_2, G, A_1, A_2, B_1, B_2, A, B) = FK - FGG_2 \tan^{-1} \left(\frac{A_2}{A_1} \tan(A) \right) + \\ FGG_1 \tan^{-1} \left(\frac{B_2}{B_1} \tan(B) \right). \quad (\text{C.27})$$

C.4 Error Probability terms for Switch and Stay Combining

The error probability terms for evaluating the SER of (5.85) are given as

$$I_8 = \left(1 - e^{-\frac{\gamma_T}{\bar{\gamma}}}\right) \int_0^{\frac{\pi}{M}} \mathcal{G}_1 \left(1, \mathcal{H}_2(1, 1, -1), 0, 1, \mathcal{H}_3(0, 1, 0, 1, 0, 0, 0, \bar{\gamma}), \right. \\ \left. \mathcal{H}_3(0, 1, 0, 1, 0, 0, 0, \bar{\gamma}), 1, 1, 1, \mathcal{H}_2(1, 1, -1), 1\right) d\phi, \quad (\text{C.28})$$

$$I_9 = e^{-\frac{\gamma_T}{\bar{\gamma}}} \int_0^{\frac{\pi}{M}} \mathcal{G}_2 \left(0, \mathcal{H}_2(1, 1, -1), \gamma_T, 0, \bar{\gamma}, N_g, 0, 0, 0, 0, 0, 0, -1\right) d\phi, \quad (\text{C.29})$$

$$I_{10} = \left(1 - e^{-\frac{\gamma_T}{\bar{\gamma}}}\right) \int_0^{\frac{\pi}{M}} \mathcal{G}_1 \left(1, \mathcal{H}_2(1, 1, 0), 0, 1, \mathcal{H}_3(1, 1, 0, 1, 0, 0, 0, \bar{\gamma}), \right. \\ \left. \mathcal{H}_3(1, 1, 0, 1, 0, 0, 0, \bar{\gamma}), 1, 1, 1, \mathcal{H}_2(1, 1, 0), 1\right) d\phi, \quad (\text{C.30})$$

$$I_{11} = e^{-\frac{\gamma_T}{\bar{\gamma}}} \int_0^{\frac{\pi}{M}} \mathcal{G}_2 \left(0, \mathcal{H}_2(1, 1, 0), \gamma_T, 1, \bar{\gamma}, N_g, 0, 0, 0, 0, 0, 0, -1\right) d\phi, \quad (\text{C.31})$$

$$I_{12} = \left(1 - e^{-\frac{\gamma_T}{\bar{\gamma}}}\right) \int_0^{\frac{\pi}{L}} \mathcal{G}_1 \left(1, \mathcal{H}_2(1, 0, 1), 1, \pi, \mathcal{H}_3(0, 1, -1, 1, 0, 0, 0, \bar{\gamma}), 1, 1, \right. \\ \left. \mathcal{H}_3(0, 1, -1, 1, 0, 0, 0, \bar{\gamma}), 1, 1, \mathcal{H}_2(0, -1, 0)\right) d\phi, \quad (\text{C.32})$$

$$I_{13} = \left(1 - e^{-\frac{\gamma_T}{\bar{\gamma}}}\right) \int_0^{\frac{\pi}{L}} \mathcal{G}_1 \left(1, \mathcal{H}_2(1, 1, 1), 1, \pi, \mathcal{H}_3(0, 1, 0, 1, 0, 0, 0, \bar{\gamma}), 1, 1, \right. \\ \left. \mathcal{H}_3(0, 1, 0, 1, 0, 0, 0, \bar{\gamma}), 1, 1, \mathcal{H}_2(0, 0, 0)\right) d\phi, \quad (\text{C.33})$$

$$I_{14} = \int_{\frac{\pi}{M}}^{\frac{\pi}{L}} \mathcal{G}_2(\mathcal{H}_2(0, -1, 0), \pi, \gamma_T, -1, \bar{\gamma}, N_g, 0, 0, 0, 0, 1, 0, -1) d\phi, \quad (\text{C.34})$$

$$I_{15} = \int_{\frac{\pi}{M}}^{\frac{\pi}{L}} \mathcal{G}_2(\mathcal{H}_2(0, 0, 0), \pi, \gamma_T, 0, \bar{\gamma}, N_g, 0, 0, 0, 0, 1, 0, -1) d\phi, \quad (\text{C.35})$$

$$I_{16} = \left(1 - e^{-\frac{\gamma_T}{\bar{\gamma}}}\right) \int_0^{\frac{\pi}{L}} \mathcal{G}_1\left(1, \mathcal{H}_2(1, 1, -1), 0, 1, \mathcal{H}_3(0, 1, 0, 1, 0, 0, 0, \bar{\gamma}), \right. \\ \left. \mathcal{H}_3(0, 1, 0, 1, 0, 0, 0, \bar{\gamma}), 1, 1, 1, \mathcal{H}_2(1, 1, -1), 1\right) d\phi, \quad (\text{C.36})$$

$$I_{17} = \left(1 - e^{-\frac{\gamma_T}{\bar{\gamma}}}\right) \int_0^{\frac{\pi}{L}} \mathcal{G}_1\left(1, \mathcal{H}_2(1, 1, 0), 0, 1, \mathcal{H}_3(1, 1, 0, 1, 0, 0, 0, \bar{\gamma}), \right. \\ \left. \mathcal{H}_3(1, 1, 0, 1, 0, 0, 0, \bar{\gamma}), 1, 1, 1, \mathcal{H}_2(1, 1, 0), 1\right) d\phi, \quad (\text{C.37})$$

$$I_{18} = e^{-\frac{\gamma_T}{\bar{\gamma}}} \int_0^{\frac{\pi}{L}} \mathcal{G}_2\left(0, \mathcal{H}_2(1, 1, -1), \gamma_T, 0, \phi, \bar{\gamma}, N_g, 0, 0, 0, 0, 0, -1\right) d\phi, \quad (\text{C.38})$$

$$I_{19} = e^{-\frac{\gamma_T}{g}} \int_0^{\frac{\pi}{L}} \mathcal{G}_2\left(0, \mathcal{H}_2(1, 1, 0), \gamma_T, 1, \bar{\gamma}, N_g, 0, 0, 0, 0, 0, -1\right) d\phi, \quad (\text{C.39})$$

$$\mathcal{G}_2(A, B, \gamma_T, n, g, N_g, k, o, p, q, r, t, u) = \frac{\pi}{2N_g}(B - A) \\ \sum_{l=1}^{N_g} \mathcal{F}\left(\frac{1}{2}(\nu_l + 1)(B - A) + A, \gamma_T, M, n, \phi, g, k, o, p, q, r, t, u\right) \sqrt{1 - \nu_l^2}, \quad (\text{C.40})$$

and

$$\mathcal{F}(x, \gamma_T, M, n, \phi, \bar{\gamma}, k, o, p, q, r, t, u) = \frac{g^q e^{-r \frac{\gamma_T}{\bar{\gamma}} (k+1)^p}}{(k+1)^p + \frac{\bar{\gamma} \sin\left(\frac{(-1)^n \phi + (-1)^o \frac{\pi}{M}\right)^2}{\sin(x)^2}} \left(t - \frac{u e^{-t \frac{\gamma_T}{\bar{\gamma}} (k+1)} e^{-\gamma_T \frac{\sin\left(\frac{(-1)^n \phi + (-1)^o \frac{\pi}{M}\right)^2}{\sin(x)^2}}}{\sin(x)^2} \right). \tag{C.41}$$

The roots of N_g -th order Gauss Chebyshev polynomial are denoted by ν_l and are the same as given in 4.34.

C.5 Error Probability terms for Switch and Examine Combining

The error probability terms for evaluating the SER of (5.87) are given as

$$I_{20} = \frac{L}{2\pi^2} \left(1 - e^{-\frac{\gamma_T}{g}}\right)^{N_R-1} \int_0^{\frac{\pi}{M}} \mathcal{G}_1\left(1, \mathcal{H}_2(1, 1, -1), 0, 1, \mathcal{H}_3(0, 1, 0, 1, 0, 0, k, \bar{\gamma}), \mathcal{H}_3(0, 1, 0, 1, 0, 0, k, \bar{\gamma}), 1, 1, 1, \mathcal{H}_2(1, 1, -1), 1\right) d\phi, \tag{C.42}$$

$$I_{21} = \frac{L}{2\pi^2} \left(1 - e^{-\frac{\gamma_T}{\bar{\gamma}}}\right)^{N_R-1} \int_0^{\frac{\pi}{M}} \mathcal{G}_1\left(1, \mathcal{H}_2(1, 1, 0), 0, 1, \mathcal{H}_3(1, 1, 0, 1, 0, 0, k, \bar{\gamma}), \mathcal{H}_3(1, 1, 0, 1, 0, 0, k, \bar{\gamma}), 1, 1, 1, \mathcal{H}_2(1, 1, 0), 1\right) d\phi, \tag{C.43}$$

$$I_{22} = \frac{L e^{-\frac{\gamma_T}{\bar{\gamma}}}}{2\pi^2} \left(\left(1 - e^{-\frac{\gamma_T}{\bar{\gamma}}}\right)^{N_R-1} - \sum_{k=0}^{N_R-1} \left(1 - e^{-\frac{\gamma_T}{\bar{\gamma}}}\right)^k \right) \int_0^{\frac{\pi}{M}} \mathcal{G}_2\left(0, \mathcal{H}_2(1, 1, -1), \gamma_T, 0, \bar{\gamma}, N_g, 0, 0, 0, 0, 0, 0, -1\right) d\phi, \tag{C.44}$$

$$I_{23} = \frac{Le^{-\frac{\gamma T}{g}}}{2\pi^2} \left(\left(1 - e^{-\frac{\gamma T}{\bar{\gamma}}}\right)^{N_R-1} - \sum_{k=0}^{N_R-1} \left(1 - e^{-\frac{\gamma T}{\bar{\gamma}}}\right)^k \right) \int_0^{\frac{\pi}{M}} \mathcal{G}_2(0, \mathcal{H}_2(1, 1, 0), \gamma_T, 1, \bar{\gamma}, N_g, 0, 0, 0, 0, 0, 0, -1) d\phi, \quad (\text{C.45})$$

$$I_{24} = \frac{L}{2\pi^2} \left(1 - e^{-\frac{\gamma T}{\bar{\gamma}}}\right)^{N_R-1} \int_{\frac{\pi}{M}}^{\frac{\pi}{L}} \mathcal{G}_1(1, 0, 1, 1, \mathcal{H}_3(0, 1, 1, 1, 0, 1, k, \bar{\gamma}), \mathcal{H}_3(0, 1, 1, 1, 0, 1, k, \bar{\gamma}), 1, \mathcal{H}_3(0, 1, 1, 1, 0, 0, k, \bar{\gamma}), 1, \frac{2\pi}{M}, \phi - \frac{\pi}{M}) d\phi, \quad (\text{C.46})$$

$$I_{25} = \frac{Le^{-\frac{\gamma T}{\bar{\gamma}}}}{2\pi^2} \left(\left(1 - e^{-\frac{\gamma T}{\bar{\gamma}}}\right)^{N_R-1} - \sum_{k=0}^{N_R-1} \left(1 - e^{-\frac{\gamma T}{\bar{\gamma}}}\right)^k \right) \int_{\frac{\pi}{M}}^{\frac{\pi}{L}} \mathcal{G}_2(\mathcal{H}_2(0, -1, 0), \pi - \frac{2\pi}{M}, \gamma_T, 0, \phi, \bar{\gamma}, N_g, 0, -1, 0, 0, 0, 0, -1) d\phi, \quad (\text{C.47})$$

$$I_{26} = \frac{Le^{-\frac{\gamma T}{g}}}{2\pi^2} \left(\left(1 - e^{-\frac{\gamma T}{\bar{\gamma}}}\right)^{N_R-1} - \left(\sum_{k=0}^{N_R-1} \left(1 - e^{-\frac{\gamma T}{\bar{\gamma}}}\right)^k \right) \right) \int_{\frac{\pi}{M}}^{\frac{\pi}{L}} \mathcal{G}_2(\mathcal{H}_2(0, 0, 0), \pi - \frac{2\pi}{M}, \gamma_T, 0, \bar{\gamma}, N_g, 0, 0, 0, 0, 0, 0, -1) d\phi, \quad (\text{C.48})$$

$$I_{27} = \frac{L}{2\pi^2} \left(1 - e^{-\frac{\gamma T}{\bar{\gamma}}}\right)^{N_R-1} \int_{\frac{\pi}{M}}^{\frac{\pi}{L}} \mathcal{G}_1(1, 0, 1, \pi, \mathcal{H}_3(0, 1, 0, 1, 0, 1, k, \bar{\gamma}), 1, 1, \mathcal{H}_3(0, 1, 0, 1, 0, 0, k, \bar{\gamma}), 1, 1, \phi + \frac{\pi}{M}) d\phi, \quad (\text{C.49})$$

$$I_{28} = \frac{L}{2\pi^2} \left(1 - e^{-\frac{\gamma T}{\bar{\gamma}}}\right)^{N_R-1} \int_{\frac{\pi}{M}}^{\frac{\pi}{L}} \mathcal{G}_1 \left(1, 0, 1, \pi, \mathcal{H}_3(0, 1, 1, 1, 0, 1, k, \bar{\gamma}), 1, 1, \mathcal{H}_3(0, 1, 1, 1, 0, 1, k, \bar{\gamma}), 1, 1, \frac{2\pi}{M}\right) d\phi, \quad (\text{C.50})$$

$$I_{29} = \frac{L e^{-\frac{\gamma T}{\bar{\gamma}}}}{2\pi^2} \left(\left(1 - e^{-\frac{\gamma T}{\bar{\gamma}}}\right)^{N_R-1} - \sum_{k=0}^{N_R-1} \left(1 - e^{-\frac{\gamma T}{\bar{\gamma}}}\right)^k \right) \int_{\frac{\pi}{M}}^{\frac{\pi}{L}} \mathcal{G}_2 \left(\pi - \frac{2\pi}{M}, \pi, \gamma_T, 0, \phi, g, N_g, 0, -1, 0, 0, 0, 0, -1\right) d\phi, \quad (\text{C.51})$$

$$I_{30} = \frac{L}{2\pi^2} \left(1 - e^{-\frac{\gamma T}{\bar{\gamma}}}\right)^{N_R-1} \int_0^{\frac{\pi}{L}} \mathcal{G}_1 \left(1, 0, 0, 1, \mathcal{H}_3(0, 1, 0, 1, 0, 1, k, \bar{\gamma}), \mathcal{H}_3(0, 1, 0, 1, 0, 0, k, \bar{\gamma}), 1, 1, 1, \mathcal{H}_2(1, 1, -1), 1\right) d\phi, \quad (\text{C.52})$$

$$I_{31} = \frac{L}{2\pi^2} \left(1 - e^{-\frac{\gamma T}{\bar{\gamma}}}\right)^{N_R-1} \int_0^{\frac{\pi}{L}} \mathcal{G}_1 \left(1, 0, 0, 1, \mathcal{H}_3(1, 1, 0, 1, 0, 1, k, \bar{\gamma}), \mathcal{H}_3(1, 1, 0, 1, 0, 0, k, \bar{\gamma}), 1, 1, 1, \mathcal{H}_2(1, 1, 0), 1\right) d\phi, \quad (\text{C.53})$$

$$I_{32} = \frac{L e^{-\frac{\gamma T}{\bar{\gamma}}}}{2\pi^2} \left(\left(1 - e^{-\frac{\gamma T}{\bar{\gamma}}}\right)^{N_R-1} - \sum_{k=0}^{N_R-1} \left(1 - e^{-\frac{\gamma T}{\bar{\gamma}}}\right)^k \right) \int_0^{\frac{\pi}{L}} \mathcal{G}_2 \left(0, \mathcal{H}_2(1, 1, -1), \gamma_T, 0, \bar{\gamma}, N_g, 0, 0, 0, 0, 0, 0, -1\right) d\phi, \quad (\text{C.54})$$

and

$$I_{33} = \frac{L e^{-\frac{\gamma T}{\bar{\gamma}}}}{2\pi^2} \left(\left(1 - e^{-\frac{\gamma T}{\bar{\gamma}}}\right)^{N_R-1} - \sum_{k=0}^{N_R-1} \left(1 - e^{-\frac{\gamma T}{\bar{\gamma}}}\right)^k \right) \int_0^{\frac{\pi}{L}} \mathcal{G}_2 \left(0, \mathcal{H}_2(1, 1, 0), \gamma_T, 1, \bar{\gamma}, N_g, 0, 0, 0, 0, 0, 0, -1\right) d\phi. \quad (\text{C.55})$$

C.6 Error Probability terms for Switch and Examine Combining with Post Selection

The error probability terms for evaluating the SER of (5.89) are given as

$$I_{34} = \frac{LN_R}{2\pi^2} \sum_{k=0}^{N_R-1} \frac{\binom{N_R-1}{k} (-1)^k}{1+k} \int_0^{\frac{\pi}{M}} \mathcal{G}_1 \left(1, \mathcal{H}_2(1, 1, -1), 0, \right. \\ \left. \mathcal{H}_3(0, 1, 0, 1, 1, 0, k, \bar{\gamma}), 1, 1, \mathcal{H}_3(0, -1, 0, 1, 1, 0, k, \bar{\gamma}), 1, 1, \mathcal{H}_2(1, 1, -1), 1 \right) d\phi, \quad (\text{C.56})$$

$$I_{35} = \binom{N_R-1}{k} (-1)^k \int_0^{\frac{\pi}{M}} \mathcal{G}_2 \left(0, \mathcal{H}_2(1, 1, -1), \gamma_T, M, 0, \bar{\gamma}, N_g, k, 0, 1, 0, 1, \right. \\ \left. 0, -1 \right) d\phi, \quad (\text{C.57})$$

$$I_{36} = \frac{LN_R}{2\pi^2} \sum_{k=0}^{N_R-1} \frac{\binom{N_R-1}{k} (-1)^k}{1+k} \int_0^{\frac{\pi}{M}} \mathcal{G}_1 \left(1, \mathcal{H}_2(1, 1, 0), 0, \mathcal{H}_3(1, 1, 0, 1, 1, 0, k, \bar{\gamma}), \right. \\ \left. 1, 1, \mathcal{H}_3(1, -1, 0, 1, 1, 0, k, \bar{\gamma}), 1, 1, \mathcal{H}_2(1, 1, 0), 1 \right) d\phi, \quad (\text{C.58})$$

$$I_{37} = \binom{N_R-1}{k} (-1)^k \int_0^{\frac{\pi}{M}} \mathcal{G}_2 \left(0, \mathcal{H}_2(1, 1, 0), \gamma_T, 1, \phi, \bar{\gamma}, N_g, k, 0, 1, 0, 1, 0, -1 \right) d\phi, \quad (\text{C.59})$$

$$I_{38} = \frac{L}{2\pi^2 \bar{\gamma}} \left(1 - \left(1 - e^{-\frac{\gamma_T}{\bar{\gamma}}} \right)^{N_R} \right) \int_0^{\frac{\pi}{M}} \mathcal{G}_2 \left(0, \mathcal{H}_2(1, 1, -1), \gamma_T, 0, \bar{\gamma}, N_g, \right. \\ \left. 0, 0, 0, 1, 0, 0, -1 \right) d\phi, \quad (\text{C.60})$$

$$I_{39} = \frac{L}{2\pi^2\bar{\gamma}} \left(1 - \left(1 - e^{-\frac{\gamma_T}{\bar{\gamma}}} \right)^{N_R} \right) \int_0^{\frac{\pi}{M}} \mathcal{G}_2 \left(0, \mathcal{H}_2(1, 1, 0), \gamma_T, 1, \bar{\gamma}, N_g, \right. \\ \left. 0, 0, 0, 1, 0, 0, -1 \right) d\phi, \quad (\text{C.61})$$

$$I_{40} = \frac{LN_R}{\pi\bar{\gamma}} \sum_{k=0}^{N_R-1} \frac{\binom{N_R-1}{k} (-1)^k}{2\pi} \int_{\frac{\pi}{M}}^{\frac{\pi}{L}} \mathcal{G}_2 \left(\mathcal{H}_2(0, -1, 0), \pi - \frac{2\pi}{M}, \gamma_T, M, 0, \bar{\gamma}, N_g, \right. \\ \left. k, -1, 1, 1, 0, 1, 1 \right) d\phi, \quad (\text{C.62})$$

$$I_{41} = \frac{LN_R}{\pi g} \sum_{k=0}^{N_R-1} \frac{\binom{N_R-1}{k} (-1)^k}{2\pi} \int_{\frac{\pi}{M}}^{\frac{\pi}{L}} \mathcal{G}_2 \left(\mathcal{H}_2(0, 0, 0), \pi, \gamma_T, 0, \phi, \bar{\gamma}, N_g, k, \right. \\ \left. 0, 1, 1, 0, 1, 1 \right) d\phi, \quad (\text{C.63})$$

$$I_{42} = \frac{LN_R}{\pi g} \sum_{k=0}^{N_R-1} \frac{\binom{N_R-1}{k} (-1)^k}{2\pi} \int_{\frac{\pi}{M}}^{\frac{\pi}{L}} \mathcal{G}_2 \left(\pi - \frac{2\pi}{M}, \pi, \gamma_T, 0, \phi, \bar{\gamma}, N_g, k, -1, \right. \\ \left. 1, 1, 0, 1, 1 \right) d\phi, \quad (\text{C.64})$$

$$I_{43} = \frac{L}{2\pi^2\bar{\gamma}} \left(1 - \left(1 - e^{-\frac{\gamma_T}{\bar{\gamma}}} \right)^{N_R} \right) \int_{\frac{\pi}{M}}^{\frac{\pi}{L}} \mathcal{G}_2 \left(\mathcal{H}_2(0, -1, 0), \pi - \frac{2\pi}{M}, \gamma_T, 0, \phi, \bar{\gamma}, N_g, \right. \\ \left. 0, -1, 0, 1, 0, 0, -1 \right) d\phi, \quad (\text{C.65})$$

$$I_{44} = \frac{L}{2\pi^2\bar{\gamma}} \left(1 - \left(1 - e^{-\frac{\gamma_T}{\bar{\gamma}}} \right)^{N_R} \right) \int_{\frac{\pi}{M}}^{\frac{\pi}{L}} \mathcal{G}_2 \left(\mathcal{H}_2(0, 0, 0), \pi, \gamma_T, 0, \phi, \bar{\gamma}, N_g, \right. \\ \left. 0, 0, 0, 1, 0, 0, -1 \right) d\phi, \quad (\text{C.66})$$

$$I_{45} = \frac{L}{2\pi^2 g} \left(1 - \left(1 - e^{-\frac{\gamma_T}{g}} \right)^{N_R} \right) \int_{\frac{\pi}{M}}^{\frac{\pi}{L}} \mathcal{G}_2 \left(\pi - \frac{2\pi}{M}, \pi, \gamma_T, 0, \bar{\gamma}, N_g, 0, -1, \right. \\ \left. 0, 1, 0, 0, -1 \right) d\phi, \quad (\text{C.67})$$

$$\begin{aligned}
I_{46} = & \frac{LN_R}{2\pi^2} \sum_{k=0}^{N_R-1} \frac{\binom{N_R-1}{k} (-1)^k}{1+k} \int_0^{\frac{\pi}{M}} \mathcal{G}_1 \left(1, \mathcal{H}_2(1, 1, -1), 0, \right. \\
& \mathcal{H}_3(0, 1, 0, 1, 1, 0, k, \bar{\gamma}, M, \phi), 1, 1, \mathcal{H}_3(0, -1, 0, 1, 1, 0, k, \bar{\gamma}), 1, 1, \\
& \left. \mathcal{H}_2(1, 1, -1), 1 \right) d\phi, \tag{C.68}
\end{aligned}$$

$$I_{47} = \binom{N_R-1}{k} (-1)^k \int_0^{\frac{\pi}{L}} \mathcal{G}_2 \left(0, \mathcal{H}_2(1, 1, -1), \gamma_T, 0, \bar{\gamma}, N_g, k, 0, 1, 0, 1, 0, -1 \right) d\phi, \tag{C.69}$$

$$\begin{aligned}
I_{48} = & \frac{LN_R}{2\pi^2} \sum_{k=0}^{N_R-1} \frac{\binom{N_R-1}{k} (-1)^k}{1+k} \int_0^{\frac{\pi}{L}} \mathcal{G}_1 \left(1, \mathcal{H}_2(1, 1, 0), 0, \right. \\
& \left. \mathcal{H}_3(1, 1, 0, 1, 1, 0, k, \bar{\gamma}), 1, 1, \mathcal{H}_3(1, -1, 0, 1, 1, 0, k, \bar{\gamma}), 1, 1, \mathcal{H}_2(1, 1, 0), 1 \right) d\phi, \tag{C.70}
\end{aligned}$$

$$I_{49} = \binom{N_R-1}{k} (-1)^k \int_0^{\frac{\pi}{L}} \mathcal{G}_2 \left(0, \mathcal{H}_2(1, 1, 0), \gamma_T, M, 1, \bar{\gamma}, N_g, k, 0, 1, 0, 1, 0, -1 \right) d\phi, \tag{C.71}$$

$$\begin{aligned}
I_{50} = & \frac{L}{2\pi^2 g} \left(1 - \left(1 - e^{-\frac{\gamma_T}{g}} \right)^{N_R} \right) \int_0^{\frac{\pi}{L}} \mathcal{G}_2 \left(0, \mathcal{H}_2(1, 1, -1), \gamma_T, 0, \bar{\gamma}, N_g, \right. \\
& \left. 0, 0, 0, 1, 0, 0, -1 \right) d\phi, \tag{C.72}
\end{aligned}$$

and

$$\begin{aligned}
I_{51} = & \frac{L}{2\pi^2 g} \left(1 - \left(1 - e^{-\frac{\gamma_T}{g}} \right)^{N_R} \right) \int_0^{\frac{\pi}{L}} \mathcal{G}_2 \left(0, \mathcal{H}_2(1, 1, 0), \gamma_T, 1, \bar{\gamma}, N_g, \right. \\
& \left. 0, 0, 0, 1, 0, 0, -1 \right) d\phi. \tag{C.73}
\end{aligned}$$



List of Figures

1.1	Worldwide spectrum allocation for 60 GHz.	6
2.1	A simplified wireless signal transmission model.	22
2.2	Path loss as a function of d for various 60 GHz channels	23
2.3	Nakagami- m and Nakagami- n amplitude PDFs for various value of m and n	28
2.4	Nakagami- m phase PDF for various value of m	29
2.5	Simplified block diagram of a direct conversion transceiver.	30
2.6	Simplified block diagram of a superheterodyne receiver.	31
2.7	A simplified thermometric coded DAC schematic.	32
2.8	Transfer characteristics of a thermometric coded DAC.	33
2.9	A simplified flash ADC schematic.	34
2.10	Transfer characteristics of a flash ADC.	35
2.11	Transfer characteristics of phase noise.	36
2.12	Phase and amplitude transfer characteristics of a nonlinear amplifier.	38
3.1	A simplified system model for a multi-carrier based transceiver.	47
3.2	Performance of multi-carrier and single-carrier based transceivers at 60 GHz employing QPSK/8PSK constellations for an ideal front end.	48
3.3	A simplified system model for a single-carrier based transceiver.	49
3.4	SNR degradation as a function of BER for various N_{DAC} values.	54

3.5	SNR degradation as a function of BER for various N_{ADC} values. . .	55
3.6	Impact of PN and AWGN on 8PSK signal constellation.	58
3.7	SNR degradation as a function of BER for various PN models. . .	58
3.8	SNR degradation as a function of BER for various I/Q imbalance parameters.	60
3.9	SNR degradation as a function of BER for various IBO values of the HPA.	62
4.1	BER of 2PAM over an AWGN channel for various N_{ADC} values. . .	73
4.2	BER of 4PAM over an AWGN channel for various N_{ADC} values. . .	74
4.3	BER of 2PAM over a Rayleigh fading channel for various N_{ADC} values.	74
4.4	BER of 4PAM over a Rayleigh fading channel for various N_{ADC} values.	75
4.5	BER of 2PAM over various Nakagami- m fading channels with different N_{ADC} values at $\bar{\gamma}_b = 10$ dB.	76
4.6	Degradation in BER as a function of M for various values of N_{ADC} over an AWGN channel at a BER of 10^{-5}	77
4.7	Degradation in BER as a function of M for various values of N_{ADC} over a Rayleigh fading channel at a BER of 10^{-3}	77
5.1	System architecture for an RF level diversity combiner.	84
5.2	System architecture for a conventional diversity combiner.	84
5.3	Comparison of simulated and analytic PDF of EGC for $N_R = 1$. . .	94
5.4	Comparison of simulated and analytic $ \phi_x(\omega) $ for $L = 2$	95
5.5	Comparison of simulated and analytic $\angle\phi_x(\omega)$ for $L = 2$	95
5.6	A comparison of simulated and analytic BER for $N_R = 2$	96
5.7	A comparison of tight (5.15) and high SNR (5.31) BER for various values of N_R and L	96
5.8	BER comparison of BPSK with BFSK and DBPSK at $\bar{\gamma} = 10$ dB. . .	97
5.9	Comparison of simulated and analytic PDF of SC for $N_R = 1$	104
5.10	A comparison of simulation and analysis for BPSK signal constellation with SC and $N_R = 2$	104
5.11	A comparison of simulation and analysis for QPSK signal constellation with SC and $N_R = 2$	105
5.12	BER comparison of BPSK with BFSK and DBPSK at $\bar{\gamma} = 10$ dB. . .	106

5.13	SER of QPSK against N_R for various L and M at $\bar{\gamma} = 10$ dB. . . .	106
5.14	Comparison of simulated and analytic PDF of SSC for $N_R = 2$. . .	114
5.15	Comparison of simulated and analytic PDF of SEC for $N_R = 2$. . .	114
5.16	Comparison of simulated and analytic PDF of SECps for $N_R = 2$. . .	115
5.17	A comparison of simulation and analysis for BPSK signal constellation with SSC, $\gamma_T = 10$ dB and $N_R = 2$	116
5.18	A comparison of simulation and analysis for QPSK signal constellation with SSC, $\gamma_T = 10$ dB and $N_R = 2$	116
5.19	A comparison of simulation and analysis for BPSK signal constellation with SEC, $\gamma_T = 10$ dB and $N_R = 2$	117
5.20	A comparison of simulation and analysis for QPSK signal constellation with SEC, $\gamma_T = 10$ dB and $N_R = 2$	118
5.21	A comparison of simulation and analysis for BPSK signal constellation with SECps, $\gamma_T = 10$ dB and $N_R = 2$	118
5.22	A comparison of simulation and analysis for QPSK signal constellation with SECps, $\gamma_T = 10$ dB and $N_R = 2$	119
5.23	Impact of switching threshold on the BER of BPSK for dual branch SSC and SECps at $\bar{\gamma} = 10$ dB.	120
5.24	Impact of switching threshold on the SER of QPSK for dual branch SEC and SECps at $\bar{\gamma} = 10$ dB.	120
5.25	BER comparison of BPSK for SEC with BFSK and DBPSK at $\bar{\gamma} = 10$ dB and $\gamma_T = 10$ dB.	121
5.26	BER comparison of BPSK for SECps with BFSK and DBPSK at $\bar{\gamma} = 10$ dB and $\gamma_T = 10$ dB.	121
5.27	SER of QPSK for SEC against N_R for various L and M at $\bar{\gamma} = 5$ dB and $\gamma_T = 10$ dB.	122
5.28	SER of QPSK for SECps against N_R for various L and M at $\bar{\gamma} = 5$ dB and $\gamma_T = 10$ dB.	123
5.29	SER of QPSK for SEC against N_R for various L and M at $\bar{\gamma} = 5$ dB and $\gamma_T = 10$ dB.	123
6.1	Acoustic demonstrator setup.	127
6.2	Simplified system block diagram of the acoustic demonstrator. . .	128
6.3	Sound card frequency response.	128
6.4	68 kHz UAT.	129

6.5 Radiation pattern of the 68 kHz UAT. 130

6.6 Receiver array of 8 microphones. 131

6.7 Impact of array radius on the beam pattern of the receiver array. . 131

6.8 Microphone beam pattern at 40 kHz. 132

6.9 A comparison of measured CIR for (a) 10 kHz and (b) 68 kHz
channels. 133

6.10 A comparison of measured PDP for (a) 10 kHz and (b) 68 kHz
channels. 134

6.11 Path loss model for 10 kHz and 68 kHz acoustic frequencies. 135

6.12 Path loss comparison for acoustic and radio frequencies. 136

6.13 BER comparison of MC-BPSK for various acoustic and radio chan-
nels. 138

6.14 BER comparison of SC-BPSK for various acoustic and radio chan-
nels. 138

C.1 Geometry for SER calculation. 160



List of Tables

1.1	Channel bandwidths and power allocations for UWB, WLAN and 60 GHz bands.	5
1.2	IEEE 802.15.3c	8
1.3	ECMA387	8
2.1	Various path loss channel parameters at 60 GHz	23
2.2	Power delay profile for LOS and NLOS 60 GHz tapped delay line model.	25
2.3	I/Q imbalance parameters for 60 GHz transceivers.	37
3.1	Single-carrier and multi-carrier system parameters.	46
3.2	Complexity of multi-carrier and single-carrier based systems.	51
3.3	Multi-carrier and single-carrier circuit parameters for quantitative comparison.	63
3.4	Multi-carrier and single-carrier quantitative comparison.	63
4.1	PDF and Fourier Transforms of Gaussian and Uniform distributions.	68
5.1	Amplifier gains for EGC, SC, SSC, SEC and SECps.	87
6.1	Soundcard properties.	129
6.2	Various measured parameters of the radio and audio channels.	136
6.3	Multi-carrier and single-carrier system parameters.	137

- 7.1 Multi-carrier and single-carrier circuit parameters for qualitative comparison 144
- 7.2 Multiple-carrier and single-carrier qualitative comparison 145
- 7.3 Number of quantization levels L , required to achieve performance close to the conventional case. 147
- 7.4 Required number of quantization levels L , to outperform non-coherent diversity combining. 148
- 7.5 A qualitative comparison of different channel parameters and BER for acoustic and radio frequencies. 149



Bibliography

- [1] P. K. Bondyopadhyay, “Sir J. C. Bose diode detector received Marconi’s first transatlantic wireless signal of December 1901 (the “Italian navy coherer” scandal revisited),” *Proceedings of the IEEE*, vol. 86, no. 1, pp. 259–285, January 1998.
- [2] R. G. Gallager, “Claude E. Shannon: A retrospective on his life, work, and impact,” *IEEE Transactions on Information Theory*, vol. 47, no. 7, pp. 2681–2695, November 2001.
- [3] P. K. Bondyopadhyay, “In the beginning,” *Proceedings of the IEEE*, vol. 86, no. 1, pp. 63–77, January 1998.
- [4] S. ten Brink, “Rate one-half code for approaching the Shannon limit by 0.1 dB,” *IEE Electronic Letters*, vol. 36, no. 15, pp. 1293–1294, July 2000.
- [5] D. C. Cox, “Chochannel interference considerations in frequency reuse small-coverage-area radio systems,” *IEEE Transactions on Communications*, vol. 30, no. 1, pp. 135–142, January 1982.
- [6] B. Sklar, *Digital Communications, Fundamentals and Applications*. Upper Saddle River, NJ: Prentice Hall, 2001.
- [7] P. Bellavista, *Telecommunication Systems and Technologies*. Paris, France: Eolss, 2001.

- [8] R. G. Freeman, *Radio System Design for Telecommunications*, 3rd ed. NY, USA: IEEE-Wiley, 2007.
- [9] J. H. Winters, "On the capacity of radio communication systems with diversity in a Rayleigh fading environment," *IEEE Journal on Selected Areas in Communications*, vol. 5, no. 5, pp. 871–878, June 1987.
- [10] G. J. Foschini and M. J. Gans, "On limits of wireless communications in a fading environment when using multiple antennas," *Wireless Personal Communications*, vol. 6, no. 3, pp. 311–335, March 1998.
- [11] G. J. Foschini, "Layered space time architecture for wireless communication in a fading environment when using multi-element antennas," *Bell Labs Technical Journal*, vol. 2, pp. 41–59, Autumn 1996.
- [12] I. E. Teletar, "Capacity of multi-antenna Gaussian channels," *European Transactions on Telecommunications*, vol. 10, no. 6, pp. 585–595, February 1999.
- [13] D. G. Brennan, "Linear diversity combining techniques," *Proceedings of the IRE*, vol. 47, pp. 1075–1102, June 1959.
- [14] M. K. Simon and M.-S. Alouini, *Digital Communication over Fading Channels*. NY, USA: John Wiley & Sons, 2004.
- [15] C. S. Tsang and T. M. Nguyen, "Survey of signal processing techniques for interference suppression in communication," in *IEEE Aerospace Conference*, March 2004, pp. 1347–1354.
- [16] D. T. Emerson, "The work of Jagadis Chandra Bose: 100 years of mm-wave research," in *IEEE MTT-S International Microwave Symposium Digest*, vol. 2, 1997, pp. 553–556.
- [17] M. Chelouche and A. Plattner, "Mobile broadband system (MBS): trends and impact on 60 ghz band mmic development," *Electronics & Communication Engineering Journal*, vol. 5, no. 3, pp. 187–197, June 1993.
- [18] F. Giannetti, M. Luise, and R. Reggiannini, "Mobile and personal communications in the 60 GHz band: A survey," *Wireless Personal Communications*, vol. 10, pp. 207–243, 1999.

- [19] P. Smulders, "Exploiting the 60 GHz band for local wireless multimedia access: prospects and future directions," *IEEE Communications Magazine*, vol. 40, no. 1, pp. 140–147, January 2002.
- [20] —, "60 GHz radio: prospects and future directions," in *IEEE Symposium on Communications and Vehicular Technologies*, 2003, pp. 1–8.
- [21] A. G. Siamarou, "Broadband wireless local-area networks at millimeter waves around 60 GHz," *IEEE Antennas and Propagation Magazine*, vol. 45, no. 1, pp. 177–181, February 2003.
- [22] B. Bosco, R. Emrick, S. Franson, J. Holmes, and S. Rockwell, "Emerging commercial applications using the 60 GHz unlicensed band: opportunities and challenges," in *IEEE wireless and Microwave Technology Conference*, December 2006, pp. 1–6.
- [23] R. C. Daniels and R. W. Heath, "60 GHz wireless communications emerging requirements and design recommendations," *IEEE Vehicular Technology Magazine*, vol. 2, no. 3, pp. 41–50, September 2007.
- [24] N. Guo, R. C. Qiu, S. S. Mo, and K. Takahashi, "60 GHz millimeter wave radio; principle, technology and new results," *EURASIP Journal on Wireless Communications and Networking*, vol. 2007, pp. 48–58, January 2007.
- [25] S. K. Yong and C. Chong, "An overview of multigigabit wireless through millimeter wave technology: potentials and technical challenges," *EURASIP Journal on Wireless Communications and Networking*, vol. 2007, pp. 58–68, January 2007.
- [26] M. Peter, W. Keusgen, and J. Luo, "A survey on 60 GHz broadband communication: Capability, applications and system design," in *IEEE European Microwave Integrated Circuit Conference*, October 2008, pp. 1–4.
- [27] "Part 15.3: Wireless medium access control (MAC) and physical layer (PHY) specifications for high data rate wireless personal area networks (WPANs)," 2009. [Online]. Available: <http://www.ieee802.org/15/pub/TG3c.html>
- [28] "High rate 60 GHz PHY, MAC and HDMI PAL," 2009. [Online]. Available: <http://www.ieee802.org/15/pub/TG3c.html>

- [29] “WirelessHD: The first 60 GHz standard,” 2009. [Online]. Available: <http://www.wirelesshd.org/>
- [30] “Wireless gigabit alliance,” 2009. [Online]. Available: <http://wirelessgigabitalliance.org/>
- [31] D. Falconer, S. L. Ariyavisitakul, A. Benyamin-Seeyar, and B. Eidson, “Frequency domain equalization for single-carrier broadband wireless systems,” *IEEE Communications Magazine*, vol. 40, no. 4, pp. 58–66, April 2002.
- [32] —, “White paper : Frequency domain equalization for single-carrier broadband wireless systems,” `whitepaper2.pdf`, February 2002. [Online]. Available: www.sce.carleton.ca/bbw/papers/
- [33] G. Fettweis, M. Lohning, D. Petrovic, M. Windisch, P. Zillmann, and W. Rave, “Dirty rf: A new paradigm,” *International Journal of Wireless Information Networks*, vol. 14, no. 2, pp. 133–148, June 2007.
- [34] J. H. Reed, *Software Radio: A Modern Approach to Radio Engineering*. NJ, USA: Prentice Hall, 2002.
- [35] B. Shim and N. Shanghag, “Complexity analysis of multicarrier and single-carrier systems for very high-speed digital subscriber line,” *IEEE Transactions on Signal Processing*, vol. 51, no. 1, pp. 282–292, Jan. 2003.
- [36] Z. Wang, X. Ma, and G. B. Giannakis, “OFDM or single-carrier block transmissions?” *IEEE Transactions on Communications*, vol. 52, no. 3, pp. 380–394, Mar. 2004.
- [37] A. Seyedi and D. Birru, “On the design of a multi-gigabit short-range communication system in the 60 GHz band,” in *IEEE CCNC*, Jan. 2007.
- [38] J. Tubbax, B. Come, L. V. Perre, L. Deneire, S. Donnay, and M. Engels, “OFDM versus single carrier with cyclic prefix: a system-based comparison,” in *Proc. IEEE Vehicular Technology Conference*, Oct. 2001, pp. 1115–1119.
- [39] N. C. Beaulieu and A. A. Abu-Dayya, “Analysis of equal diversity on Nakagami fading channels,” *IEEE Transactions on Communications*, vol. 39, no. 4, pp. 225–234, February 1991.

- [40] Q. T. Zhang, "A simple approach to probability of error for equal gain combiners over Rayleigh fading," *IEEE Transactions on Vehicular Technology*, vol. 48, no. 4, pp. 1151–1154, July 1999.
- [41] A. Annamalai, C. Tellambura, and V. K. Bhargava, "Equal-gain diversity receiver performance in wireless channels," *IEEE Transactions on Communications*, vol. 48, no. 10, pp. 1732–1745, October 2000.
- [42] M.-S. Alouini and M. K. Simon, "Performance analysis of coherent equal gain combining over Nakagami- m fading channels," *IEEE Transactions on Vehicular Technology*, vol. 50, no. 6, pp. 1449–1463, November 2001.
- [43] X. Qi, M.-S. Alouini, and Y.-C. Ko, "Closed-form analysis of dual-diversity equal-gain combining over Rayleigh fading channels," *IEEE Transactions on Wireless Communications*, vol. 2, no. 6, pp. 1120–1125, November 2003.
- [44] R. Annavajjala and L. B. Milstein, "Performance analysis of optimum and suboptimum selection diversity schemes on Rayleigh fading channels with imperfect channel estimates," *IEEE Transactions on Vehicular Technology*, vol. 56, no. 3, pp. 1119–1130, May 2007.
- [45] M. A. Blanco, "Diversity receiver performance in Nakagami fading," in *IEEE Southeast. Conf.*, 1983.
- [46] F. Adachi, K. Ohno, and M. Ikura, "Postdetection selection diversity reception with correlated, unequal average power Rayleigh fading signals for $\pi/4$ -shift qdpsk mobile radio," *IEEE Transactions on Vehicular Technology*, vol. 41, pp. 199–210, May 1992.
- [47] O. C. Ugweje and V. A. Aalo, "Performance of selection diversity system in correlated Nakagami fading," May 1997, pp. 1488–1492.
- [48] M. K. Simon and M.-S. Alouini, "A unified performance analysis of digital communications with dual selective combining over correlated Rayleigh and Nakagami- m fading channels," *IEEE Transactions on Communications*, vol. 47, pp. 33–43, January 1999.
- [49] M. A. Blanco and K. J. Zdunek, "Performance and optimization of switched diversity systems for the detection of signals with Rayleigh fading," *IEEE*

- Transactions on Communications*, vol. 27, no. 12, pp. 1887–1895, December 1979.
- [50] A. A. Abu-Dayya and N. C. Beaulieu, “Analysis of switched diversity systems on generalized-fading channels,” *IEEE Transactions on Communications*, vol. 42, no. 11, pp. 2959–2966, November 1994.
- [51] Y.-C. Ko, M.-S. Alouini, and M. K. Simon, “Analysis and optimization of switched diversity systems,” *IEEE Transactions on Vehicular Technology*, vol. 49, no. 5, pp. 1813–1831, September 2000.
- [52] C. Tellambura, A. Annamalai, and V. K. Bhargava, “Unified analysis of switched diversity systems in independent and correlated fading,” *IEEE Transactions on Communications*, vol. 49, no. 11, pp. 1955–1965, November 2001.
- [53] H.-C. Yang and M.-S. Alouini, “Performance analysis of multibranch switched diversity systems,” *IEEE Transactions on Communications*, vol. 51, no. 5, pp. 782–794, May 2003.
- [54] —, “Improving the performance of switched diversity with post-examining selection,” *IEEE Transactions on Wireless Communications*, vol. 5, no. 1, pp. 67–71, January 2006.
- [55] L. Xiao and X. Dong, “Error performance of selection combining and switched combining systems in Rayleigh fading channels with imperfect channel estimation,” *IEEE Transactions on Vehicular Technology*, vol. 54, pp. 2054–2065, November 2005.
- [56] T. S. Rappaport, *Wireless Communications*. Upper Saddle River, NJ: Prentice Hall, 1996.
- [57] P. A. Bello, “Characterization of randomly time-variant linear channels,” *IEEE Transactions on Communications*, vol. 11, no. 4, pp. 360–393, December 1963.
- [58] H. Yang, P. F. M. Smulders, and M. H. A. J. Herben, “Channel characteristics and transmission performance for various channel configurations at 60 GHz,” *EURASIP Journal*, vol. 1, pp. 1–3, 2006.

- [59] H. Xu, V. Kukshya, and T. S. Rappaport, "Spatial and temporal characteristics of 60-GHz indoor channels," *IEEE Journal on Selected Areas in Communications*, vol. 20, no. 3, pp. 620–630, April 2002.
- [60] D. Dardari, L. Minelli, V. Tralli, and O. Andrisano, "Wideband indoor communication channels at 60 GHz," in *Proc. IEEE 7th International Symposium on PIMRC*, October 1996, pp. 791–794.
- [61] J. Purwaha, A. Mank, D. Matic, K. Witrisal, and R. Parsad, "Wide-band channel measurements at 60 GHz in indoor environments," in *Proc. IEEE Benelux 6th Symposium on Vehicular Technology and Communications*, October 1998.
- [62] J.-H. Park, Y. Kim, Y.-S. Hur, K. Lim, and K.-H. Kim, "Analysis of 60 GHz band indoor wireless channels with channel configurations," in *Proc. IEEE 9th International Symposium on PIMRC*, September 1998, pp. 617–620.
- [63] J. Hübner, S. Zeisberg, K. Koora, J. Borowski, and A. Finger, "Simple channel model for 60 GHz indoor wireless LAN design based on complex wideband measurements," in *Proc. IEEE 47th Vehicular Technology Conference*, May 1997, pp. 1004–1008.
- [64] N. Moraitis and P. Constantinou, "Indoor channel measurements and characterization at 60 GHz for wireless local area network applications," *IEEE Transactions on Antennas and Propagation*, vol. 52, no. 12, pp. 3180–3189, December 2004.
- [65] A. Goldsmith, *Wireless Communications*. New York, NY: Cambridge University Press, 2005.
- [66] M. Fryziel, C. Loyez, L. Clavier, N. Rolland, and P. A. Rolland, "Path-loss model of the 60-GHz indoor radio channel," *Microwave and Optical Technology Letters*, vol. 34, no. 3, pp. 158–162, August 2002.
- [67] S. Emami, B. Gaucher, A. Mathew, and Z. Lai, "60 GHz channel model parameters for IBM measurement set," 15-05-0644-00-003c-60-ghz-channel-model-parameters-ibm-measurement-set.ppt, November 2005. [Online]. Available: <ftp://ieee:wireless@ftp.802wirelessworld.com/15/05/>

- [68] P. Pagani, N. Malhouroux, I. Siaud, and V. Guillet, "Characterization and modeling of the 60 GHz indoor channel in the office and residential environments," 15-06-0027-02-003c-indoor-channel-models-60ghz-v1-1.doc, October 2006. [Online]. Available: <ftp://ieeewireless@ftp.802wirelessworld.com/15/06/>
- [69] K. Witrisal, *OFDM Air-Interface Design For Multimedia Communications*. PhD Thesis: EWI, Delft University of Technology, Delft, The Netherlands, 2002.
- [70] W. Lee, K. Kim, J. Kim, and Y. Kim, "Multipath channel modeling 60 GHz frequency band," 15-06-0038-01-003c-multipath-channel-modeling-60ghz-frequency-band.ppt, January 2006. [Online]. Available: <ftp://ieeewireless@ftp.802wirelessworld.com/15/06/>
- [71] M. Yacoub, G. Fraidenraich, and J. C. S. S. Filho, "Nakagami-m phase-envelope joint distribution," *IEE Electronics Letters*, vol. 41, pp. 259–261, March 2005.
- [72] P. Jespers, *Integrated Converters D to A and A to D Architectures, Analysis and Simulation*. Oxford University Press, 2001.
- [73] H. Hoshino, R. Tachibana, T. Mitomo, N. Ono, Y. Yoshihara, and R. Fujimoto, "A 60-GHz phase-locked loop with inductor-less prescaler in 90-nm CMOS," in *Proc. IEEE European Solid State Circuits Conference*, September 2007, pp. 472–475.
- [74] A. Bourdoux, J. Nsenga, W. V. Thillo, F. Horlin, and L. V. der Perre, "Air interface and physical layer techniques for 60 GHz WPANs," in *IEEE Symposium on Communications and Vehicular Technology*, November 2006, pp. 1–6.
- [75] C. Cao and K. K. O, "Millimeter-wave voltage-controlled oscillators on 0.13- μ m CMOS technology," *IEEE Journal of Solid State Circuits*, vol. 41, no. 6, pp. 1297–1304, June 2006.
- [76] B. Floyd, S. Reynolds, U. Pfeiffier, T. Beukema, J. . Grzyb, and C. Haymes, "A 60 GHz receiver and transmitter chipset for broadband communications in Silicon," in *Proc. IEEE ISSCC Digest Technical Papers*, February 2006.

- [77] B. Razavi, "A mm-wave CMOS heterodyne receiver with on-chip LO and driver," in *Proc. IEEE ISSCC Digest Technical Papers*, February 2007.
- [78] A. A. M. Saleh, "Frequency-independent and frequency-dependent nonlinear models of TWT amplifiers," *IEEE Transactions on Communications*, vol. COM-29, no. 11, pp. 1715–1720, November 1981.
- [79] E. Costa and S. Pupolin, "M-QAM OFDM system performance in the presence of a nonlinear amplifier and phase noise," *IEEE Transactions on Communications*, vol. 48, no. 1, pp. 37–44, January 2000.
- [80] M. Kärkkäinen, M. Varonen, P. Kangaslahti, and K. Halonen, "Integrated amplifier circuits for 60 GHz broadband telecommunication," *Analog integrated circuits and signal processing*, vol. 42, pp. 37–46, Jun. 2005.
- [81] A. R. S. Bahai and B. R. Saltzberg, *Multi-Carrier Digital Communications, Theory and Applications of OFDM*. New York: Kluwer Academic Publishers, 2002.
- [82] J. G. Proakis and D. G. Manolakis, *Digital Signal Processing; Principles, Algorithms and Applications*. NJ, USA: Prentice Hall, 1996.
- [83] J. Tubbx, B. Come, L. V. Perre, S. Donnay, M. Engels, H. D. Man, and M. Moonen, "Compensation of IQ imbalance and phase noise in OFDM systems," *IEEE Transactions on Wireless Communications*, vol. 4, no. 3, pp. 872–877, May 2005.
- [84] T. Matsumoto, S. Fujita, H. Lei, M. Sim, and Y. Z. Raymond, "Panasonic PHY and MAC proposal to IEEE802.15 TG3c CFP," 15-07-0698-05-003c-panasonic-ook-based-60ghz-phy-mac-proposal.pdf, Jul. 2007. [Online]. Available: <https://mentor.ieee.org/802.15/file/07/>
- [85] A. Moschitta and D. Petri, "Wideband communication system sensitivity to overloading quantization noise," *IEEE Transactions on Instrumentation and Measurement*, vol. 52, no. 4, pp. 1302–1307, August 2003.
- [86] K. Cho and D. Yoon, "On the general BER expression of one- and two-dimensional amplitude modulations," *IEEE Transactions on Communications*, vol. 50, no. 7, pp. 1074–1080, July 2002.

- [87] R. K. Bock and W. Krischer, *The Data Analysis BriefBook*. Berlin, Germany: Springer-Verlag, 1998.
- [88] “The wolfram functions site,” 2009. [Online]. Available: <http://functions.wolfram.com/06.25.21.0001.01>
- [89] M. Abramowitz and I. A. Stegun, *Handbook of Mathematical Functions with Formulas, Graphs and Mathematical Tables*, 9th ed. NY, USA: Dover Publications, 1970.
- [90] P. Baltus, P. Smulders, and Y. Yu, “Systems and Architectures for Very High Frequency Radio Links,” *Analog Circuit Design (Book Chapter)*, vol. 3, pp. 1–3, 2008.
- [91] C. C. Ling and Z. Chunning, “Low-complexity antenna diversity receivers for mobile wireless applications,” vol. 14, pp. 65–81, 2000.
- [92] N. N. Lebedev, *Special Functions and Their Applications*. Prentice Hall, 1965.
- [93] S. Nadarajah and S. Kotz, “On the product and ratio of gamma and weibull random variables,” vol. 22, pp. 338–344, 2006.
- [94] Z. Wang and G. B. Giannakis, “A simple and general parameterization quantifying performance in fading channels,” *IEEE Transactions on Communications*, vol. 51, no. 8, pp. 1389–1398, Aug. 2003.
- [95] J. G. Proakis, *Digital Communications*, 4th ed. NY, USA: McGraw-Hill, 2001.
- [96] M. K. Simon and D. Divsalar, “Some new twists to problems involving the Gaussian probability integral,” *IEEE Transactions on Communications*, vol. 46, no. 2, pp. 200–210, February 1998.
- [97] G. L. Stüber, *Principles of Mobile Communication*, 2nd ed. NY, USA: Kluwer Academic Publishers, 2002.
- [98] J. Nocedal and S. J. Wright, *Numerical Optimization*. NY, USA: Springer-Verlag, 1999.

- [99] E. Digital, *AudioFire Windows Manual v2.0*. CA, USA: Echo Digital Audio Corporation, 2006.
- [100] A. Levy, J. Rossi, J. Barbot, and J. Martin, “An improved channel sounding technique applied to wideband mobile 900 mhz propagation measurements,” May 1990, pp. 513–519.
- [101] J. A. G. Akkermans and M. H. A. J. Herben, “Planar beam-forming array for broadband communications in the 60 GHz band,” in *The Second European Conference on Antennas and Propagation (EuCAP)*, November 2007.
- [102] F. Gross, *Smart Antennas for Wireless Communications*. NY, USA: McGraw-Hill, 2005.
- [103] S. Salous and N. Razavi-Ghods, *Handbook of Mathematical Functions with Formulas, Graphs and Mathematical Tables*. Durham, UK: EURO-COST, 2004.
- [104] H. E. Bass, L. C. Sutherland, A. J. Zuckerwar, D. T. Blackstock, and D. M. Hester, “Atmospheric absorption of sound: futher developments,” vol. 97, no. 1, pp. 680–683, January 1995.
- [105] “The wolfram functions site,” 2008. [Online]. Available: <http://functions.wolfram.com/01.03.21.0096.01>
- [106] “The wolfram functions site,” 2008. [Online]. Available: <http://functions.wolfram.com/GammaBetaErf/Erfi/>
- [107] A. Erdélyi, *Higher Transcendental Functions, Volume I*. FL, USA: Robert E. Krieger Publishing, 1985.



Publications by the Author

- [J1] U. H. Rizvi, G. J. M. Janssen and J. H. Weber, “BER Analysis for MPAM Signal Constellations in the Presence of Fading and ADC Quantization Noise,” *IEEE Communications Letters*, vol. 13, no. 10, pp. 733–735, October 2009.
- [J2] Z. Genc, U. H. Rizvi, E. Onur and I. Niemegeers, “Cooperative Communications in Future Home Networks,” *Wireless Personal Communications*, vol. 53, no. 3, pp. 349–364, May 2010.
- [J3] U. H. Rizvi, F. Yilmaz, M-S. Alouini, G. J. M. Janssen and J. H. Weber, “Performance of Equal Gain Combining with Quantized Phases in Rayleigh Fading Channels,” *IEEE Transactions on Communications*, vol. 59, no. 1, pp. 13–18, January 2011.
- [J4] U. H. Rizvi, F. Yilmaz, M-S. Alouini, G. J. M. Janssen and J. H. Weber, “Performance of Selection and Switched Combining with Quantized Phases in Rayleigh Fading Channels,” *IEEE Transactions on Wireless Communications (under preparation)*, November 2011.

- [C1] O. Al-askary, U. H. Rizvi and M. N. Khormuji, "Rate adaptive generalized concatenated codes for wireless communication," *International Multi-topic Conference on Communication*, December 2005.
- [C2] M. N. Khormuji, U. H. Rizvi, G. J. M. Janssen and S. B. Slimane, "Rotation optimization for MPSK/MQAM signal constellations over Rayleigh fading channels," *IEEE International Conference on Communications Systems*, October 2006.
- [C3] N. F. Kiyani, U. H. Rizvi, J. H. Weber and G. J. M. Janssen, "Optimized rotations for LDPC-coded gray-mapped MPSK constellations with signal space diversity," *IEEE Symposium on Communications and Vehicular Technology*, November 2006.
- [C4] N. F. Kiyani, U. H. Rizvi, J. H. Weber and G. J. M. Janssen, "Optimized rotations for LDPC-coded MPSK constellations with signal space diversity," *IEEE Wireless Communications and Networking Conference*, March 2007.
- [C5] U. H. Rizvi, G. J. M. Janssen and S. B. Slimane, "Combined multiple transmit antennas and multi-level modulation techniques," *Benelux Information Theory Symposium*, May 2007.
- [C6] U. H. Rizvi, G. J. M. Janssen and J. H. Weber, "Impact of RF impairments on the performance of multi-carrier and single-carrier based 60 GHz transceivers," *IEEE Symposium on Communications and Vehicular Technology*, November 2007.

- [C7] U. H. Rizvi, G. J. M. Janssen and J. H. Weber, "Impact of RF circuit imperfections on multi-carrier and single-carrier based transmissions at 60 GHz," *IEEE Radio and Wireless and Symposium*, January 2008.
- [C8] U. H. Rizvi, G. J. M. Janssen and J. H. Weber, "BER analysis of single-carrier MPAM in the presence of ADC quantization noise," *IEEE Personal Indoor Mobile Radio Communications Conference*, September 2008.
- [C9] U. H. Rizvi, G. J. M. Janssen and J. H. Weber, "BER analysis of BPSK and QPSK constellations in the presence of ADC quantization noise," *IEEE Asia Pacific Conference on Communications*, October 2008.
- [C10] U. H. Rizvi, F. Yilmaz, M-S. Alouini, G. J. M. Janssen and J. H. Weber, "Performance of RF Level Diversity Combining with Quantized Channel Estimates over Rayleigh Fading," *IEEE Communication Theory Workshop*, May 2009.
- [C11] U. H. Rizvi, F. Yilmaz, M-S. Alouini, G. J. M. Janssen and J. H. Weber, "Performance of Equal Gain Combining for Quantized Estimates of Rayleigh Fading Channels," *IEEE European Wireless Conference*, May 2009.
- [C12] U. H. Rizvi, F. Yilmaz, M-S. Alouini, G. J. M. Janssen and J. H. Weber, "Switched Combining with Quantized Channel Phase Compensation over Rayleigh Fading," *IEEE Symposium on Communications and Vehicular Technology*, November 2009.
- [C13] U. H. Rizvi, F. Yilmaz, M-S. Alouini, G. J. M. Janssen and J. H. Weber, "Selection Combining with Quantized Channel Phase Compensation over Rayleigh Fading," *IEEE Radio and Wireless Symposium*, January 2010.

The table on the next page depicts the relation between the publications and the chapters of the dissertation; "•" is used to show this relation.

Publications	Ch. 2	Ch. 3	Ch. 4	Ch. 5	Ch. 6
J1			•		
J2*					
J3				•	
J4				•	
C1*					
C2*					
C3*					
C4*					
C5*					
C6		•			
C7		•			
C8			•		
C9			•		
C10				•	
C11				•	
C12				•	
C13				•	

“*” denotes that the paper has no relation with the dissertation.



Samenvatting

Impact of RF Imperfections on 60 GHz Wireless Communication Systems

Draadloze communicatie is in de afgelopen paar decennia een enorm succes gebleken en heeft geleid tot een bloeiende industrie met momenteel meer dan 5 miljard mobiele telefoons in gebruik. Dit heeft aan de ene kant het leven van gebruikers gemakkelijker gemaakt, maar tegelijkertijd heeft deze enorme groei nieuwe uitdagingen gebracht voor draadloze systeemontwerpers. Grote en snelle veranderingen in het draadloze communicatie kanaal resulteren in grote verschillen in de instantane ontvangen signaalsterkte. Aangezien de meeste mobiele systemen worden gevoed door batterijen en opereren in een netwerk is alleen het verhogen van het zendvermogen niet een aantrekkelijke oplossing, omdat het de levensduur van de batterij vermindert en interferentie naar andere gebruikers verhoogt. De grootste uitdaging in draadloze communicatie is dan ook om de communicatiesnelheid en de linkbetrouwbaarheid te verhogen door het gebruik van energie zuinige, goedkope en spectraal efficiënte systemen. Zelfs met de komst van efficiënte signaalverwerkingstechnieken en energie zuinige hardware, blijft het fysieke knelpunt de beschikbare bandbreedte van het systeem. Dit heeft geleid tot de introductie van de 60 GHz-band als een aantrekkelijk alternatief. En van de voordelen van de licentie-vrije 60 GHz-band is de systeem bandbreedte tot maximaal 7 GHz, welke zeer geschikt is voor korte afstand draadloze communicatie zoals bijvoorbeeld wireless local area netwerken.

Er zijn echter bepaalde uitdagingen die moeten worden overwonnen voordat de 60 GHz-band in zijn volledigheid kan worden benut. Deze uitdagingen zijn het ontwerpen van hardware-componenten, zoals antennes, versterker en mixers; identificatie en het gebruik van geschikte basisband verwerkingsalgoritmen en efficiënte communicatie protocollen voor draadloze netwerken die werkzaam zijn in de 60 GHz-band. Dit proefschrift behandelt het ontwerp en de ontwikkeling van de basisband verwerkingsalgoritmen voor communicatietoestellen die werken bij een draaggolffrequentie rond de 60 GHz.

Als eerste worden in dit proefschrift twee praktische kandidaten voor basisband implementatie gedentificeerd: single-carrier en multi-carrier basisband implementatie. De twee technieken

worden geanalyseerd onder verschillende circuit onvolkomenheden, waaronder fase ruis en niet-lineair gedrag. Dit wordt gedaan omdat low-cost radiofrequentie circuits in de 60 GHz-band geen ideale prestaties leveren. Voor beide alternatieven wordt de prestatiesdegradatie in termen van operationele parameters bepaald, zoals het benodigde aantal bits in de digitale-naar-analoog converter en de analoog-naar-digitaal converter en input back-off voor de versterker als een functie van de bit fout kans. In dit proefschrift is aangetoond dat de single-carrier systemen een lagere degradatie in prestaties van het systeem voor een bepaalde set van circuit parameters vertonen. De single-carrier regeling is daarom aangewezen als een geschikte kandidaat voor 60 GHz baseband implementatie.

Als tweede hebben we de mogelijkheid onderzocht om de systeemprestaties te verhogen door gebruik te maken van eenvoudige, goedkope, hoogfrequent diversiteit schema's. Drie diversiteit schema's zijn onderzocht: *equal gain combining*, *selection combining* en *switched combining*. Een analytisch kader voor de evaluatie van de prestaties van deze diversiteit schema's is ontwikkeld. Analytische uitdrukkingen voor de bit error rate en de symbol error rate van hogere orde PSK gemoduleerde symbolen over Rayleigh fading kanalen worden afgeleid. De afgeleide uitdrukkingen worden vervolgens gebruikt om de prestaties te vergelijken met niet coherent ontvangers en diversiteit. Het is aangetoond dat het aantal kwantisatie niveaus dat nodig is om in de buurt van ideale prestaties te komen afhankelijk is van het aantal ontvangstantennes en het modulatie-niveau. De analyse wordt ook gebruikt om de impact van fase kwantisatie te onderzoeken op de thresholds voor geschakelde diversiteit schema's. Er wordt aangetoond dat de threshold niet zwaar beïnvloed wordt door fase kwantisatie. De mogelijkheid om verschillende systeem-niveau trade-offs uit te voeren is ook aangetoond.

Ten slotte is een low cost audio demonstrator voorgesteld. De akoestische kanalen die in dit proefschrift zijn onderzocht kunnen worden gebruikt om een hoge multi-pad omgeving te bieden die ook typisch is voor 60 GHz-kanalen. Dit biedt een praktische manier om de prestaties van verschillende basisband processing algoritmes op een kosteneffectieve manier te testen.

Umar H. Rizvi



Acknowledgements

It has been a long and tiring journey with many hurdles and bumps. At certain points it seemed a never ending road, however this chapter in my life is finally coming to an end. It was in the end a wonderful experience and I had the good fortune of coming in contact with many people from different cultures and backgrounds which has helped me to develop various skills and friendships which I will cherish for the rest of my life. While this thesis carries my name as an author on the title page, this is in fact a collaborative effort and would not have been possible without the help and guidance of many individuals whom I wish to acknowledge.

First and foremost I would like to thank my supervisors Prof. Gerard Janssen and Prof. Jos Weber from the Wireless and Mobile Communications group of TU Delft for providing me with a wonderful opportunity to carry out this research. Their constructive criticism, insightful comments and valuable suggestions has helped to improve the overall presentation and technical content of this work. I would also like to thank Prof. Ignas Niemegeers for acting as a promoter for this thesis and to all the members of the examination committee.

I would like to thank my former colleagues and office mates in Delft. First of all Dr. Nauman Kiyani and Dr. Santpal Dhillon for a being a wonderful company and enlightening discussions that we had while cooking food or hanging out in Rotterdam. Thanks also to Dr. Zoubir Irrahauten for helping out with the acoustic demonstrator and more importantly with my first ever APK. I would also like to mention here Prof. Ertan Onur for being a very nice office mate and friend throughout my stay in Delft. Special thanks also to Marjon Verkaik-Vonk, Wendy Murtinu - Van Schagen and Stefanie van Gentevoort for helping out with administrative matters.

I would also like to express my deepest gratitude to Prof. Mohamed-Slim Alouini of King Abdullah University of Science and Technology (KAUST) for hosting me in his research group in Texas A&M University in Qatar (TAMUQ) for 4 months. Most of the work on diversity combining was done when I was a visiting researcher in TAMUQ. Here also, I would like to express my gratitude to Dr. Ferkan Yilmaz of KAUST for helping me with many technical issues and introducing me to the wonderful world of Mathematica. I would always miss his

company and especially the memorable trip of San Francisco and Aalborg. I would also like to thank my colleagues in TAMUQ, Ki-Hong, Jee Hun and Kyu Song for the wonderful time that we spent together. Especially, Ki-Hong with whom I shared the apartment, played squash and mostly hitched a ride to work.

Here, I would also like to thank Mr. and Mrs. Karijoredjo for hosting me on their house for some home cooked Suriname food and Aisjah for being a wonderful company and making the life in Netherlands a lot more bearable.

I would also like to acknowledge the help and assistance of my current colleagues at ASML. Firstly, I would like to thank Guido Verbeeten for offering me a wonderful opportunity to work in the Imaging and Focus group at ASML. The first days at ASML were quite hectic and I would like to thank my FlexWave team mates Dr. James Downes, Dr. Milenko Jovanovic, Ad van Gestel, Ralph Haanraads, Dr. Konstantin Leavsky and Aditya Deshpande. Especially, I am highly grateful to Dr. Milenko Jovanovic and Dr. James Downes for being patient and taking time to answer my questions on Metrology.

Lastly and most importantly, I would like to express my deepest and sincere gratitude to my parents, brother and sister. Especially, I would like to thank Mama and Papa for enduring my absence, believing in me and encouraging me every step of the way. Without their help and support all of this would have been impossible. This thesis is in part theirs too.

*Eindhoven,
November 2011*

Umar Hassan Rizvi



Curriculum Vitae

Umar Rizvi was born in Lahore, Pakistan, on September 13, 1982. He graduated with a bachelors degree (cum laude) in electronics engineering from Ghulam Ishaq Khan Institute of Engineering Science and Technology (GIKI), Pakistan, in May 2004. He graduated with Masters of Science degree from Royal Institute of Technology, Stockholm, Sweden in wireless systems in January 2006. In April 2006, he started his research work towards a doctorate of philosophy (PhD.) degree in electrical engineering from Wireless and Mobile Communications group, Faculty of Electrical Engineering, Mathematics and Computer Science (EEMCS), Delft University of Technology, Netherlands. The research conducted by him in Delft University of Technology is presented here in this dissertation. Since April 2010, he is working as a Design Engineer in ASML.